

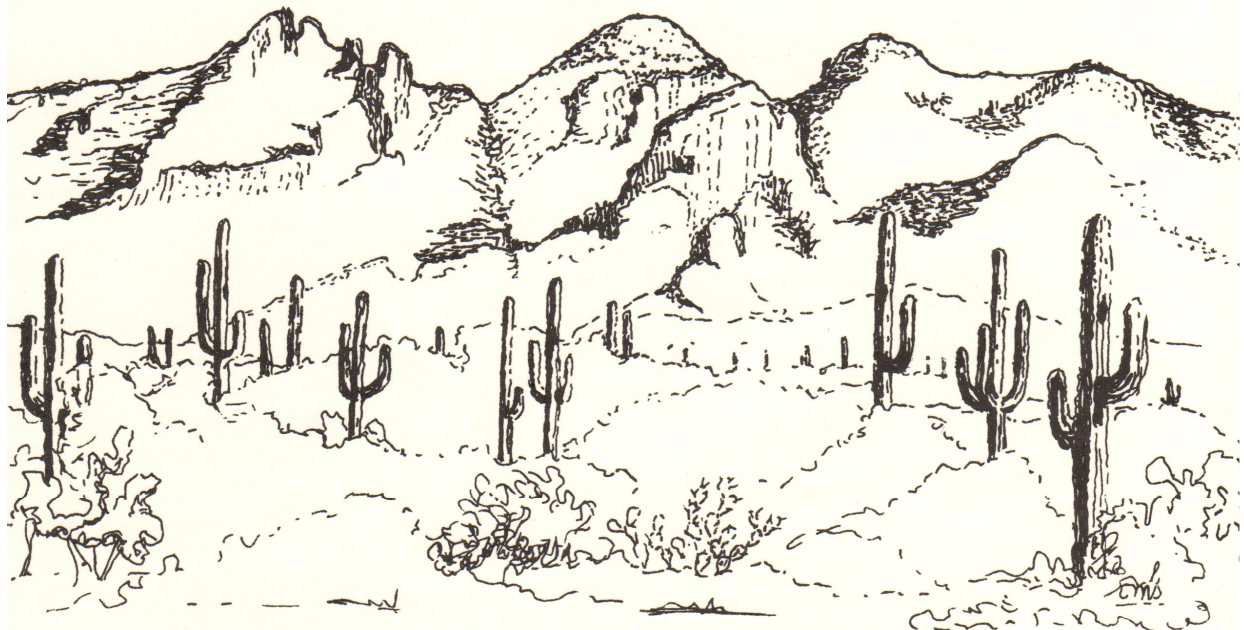


**GEOPHYSICAL INVESTIGATION OF
THE TUCSON MOUNTAINS**

GEOPHYSICS FIELD CAMP 2011

LASI-11-1

May 14, 2011



**GEOPHYSICAL INVESTIGATION OF
THE TUCSON MOUNTAINS**

**GEOPHYSICS FIELD CAMP 2011
LASI-11-1
May 14, 2011**

Patrick Avanesians
Giancarlo A. Daroch
John Fleming
Stephen A. Hundt
Steven C. Leake
Lujendra Ojha
Ben K. Sternberg
David F. Wampler

Abstract

Transient Electromagnetic (TEM), Controlled Source Audio Magnetotellurics (CSAMT), Gravity, and Magnetic data were collected in the Tucson Mountains during the Spring semester, 2011. The goal was to investigate the extent of a low-resistivity porous sedimentary layer and faults that may form potential traps located under the surface volcanic layers, as interpreted by Lipman 1993. The sedimentary layer under the volcanics has the potential to be used for either water resources or compressed air storage to store solar energy. The results from the TEM and CSAMT surveys broadly correlated with the thickness of the volcanic layer and throw of the faults interpreted by Lipman, 1993. The gravity modeling suggested the faults may have a larger throw than what was indicated by the other methods. Because of the fundamental uncertainty in the densities to use in the modeling, it was concluded that the gravity modeling may not give as accurate a prediction of the structure in this region. For further investigation of the deep porous sedimentary layer, we suggest that TEM and CSAMT are the most effective methods.

Acknowledgements

The University of Arizona Geophysics Field Camp class, GEN/GEOS 416/516, would like to thank Science Foundation Arizona (SFAZ) for providing the funding for this project (Contract Number 0405-08) and the Arizona Research Institute for Solar Energy (AzRISE) and Dr. Joseph H. Simmons, Director of AzRISE, for their support of this project. Without this funding and support, we would not have been able to offer the class this year and this extraordinary opportunity to characterize the potential water resources and potential compressed air energy storage under the Tucson Mountains would not have been possible.

We wish to thank Zonge Engineering for loaning the equipment to our class for the TEM and CSAMT surveys. This equipment was essential for this project.

Dr. Charles Stoyer, president of Interpex Limited, provided the modeling software, which we used to run inversions on our TEM, magnetics, and gravity data. This made it possible for us to make quantitative comparisons with the geologic cross sections.

Dr. Mark Gettings, in the USGS Tucson office, made available the regional magnetic and gravity data over the Tucson Mountains, which provided an important comparison for the data we collected in the field. Dr. Gettings also provided extensive review comments for all the chapters in the report, which were invaluable to the students.

Leandra Marshall provided assistance in pre-processing the regional magnetics and gravity data. Her knowledge in dealing with these data was helpful in allowing our class to proceed with the data analysis.

Thanks to the Pima County Parks Department, which provided us with the special use permits needed to carry out our research in the Tucson Mountains.

TABLE OF CONTENTS

	Abstract	3
	Acknowledgements	4
1	Introduction	8
	1.1 Geology of Tucson Mountains	9
	1.2 Geographic location	16
	1.3 Objectives	18
2	Transient Electromagnetic (TEM) Survey.....	20
	2.1 Introduction	20
	2.2 Location	20
	2.3 Instrumentation and Field Procedures.....	22
	2.4 Data Processing	23
	2.5 Layered-Earth Modeling	30
	2.6 Comparison with Geological Sections	40
3	Controlled Source Audio Magnetotelluric (CSAMT) Survey.....	47
	3.1 Introduction and Location.....	47
	3.2 Methodology and Instrumentation.....	47
	3.3 Data Processing.....	48
	3.4 Interpretation	49
4	Magnetic Survey.....	54
	4.1 Introduction and Location.....	54
	4.2 Instrumentation and Field Procedures.....	54
	4.3 Data Processing and Interpretation.....	60

	4.4 Modeling and Inversion.....	72
5	Gravity Survey.....	77
	5.1 Introduction and Location.....	77
	5.2 Instrumentation and Field Procedures.....	79
	5.3 Data Processing and Interpretation.....	81
	5.4 Gravity Meter Test	81
	5.5 Gravity Modeling/Inversion	93
6	Summary and Conclusions	97
	6.1 Data Profile Summaries	97
	6.2 Conclusions	101
7	References.....	103

1. Introduction

The GEN/GEOS 416/516, Field Studies in Geophysics class conducted geophysical surveys in the Tucson Mountains during the Spring Semester of 2011. Geophysics data at this site may have a number of practical applications. For example, there is considerable interest in the potential for future water resources under the Tucson Mountains as well as potential for Compressed Air Energy Storage (CAES) in porous rocks underneath the Tucson Mountains. We note, however, that the Tucson Mountains are a wilderness area. Any potential use of this area for water resources or CAES storage could be done with horizontal drilling from a drill site outside of the Tucson Mountain Park. Figure 1.1 shows the location of the study area (red rectangle) on a map of Arizona.

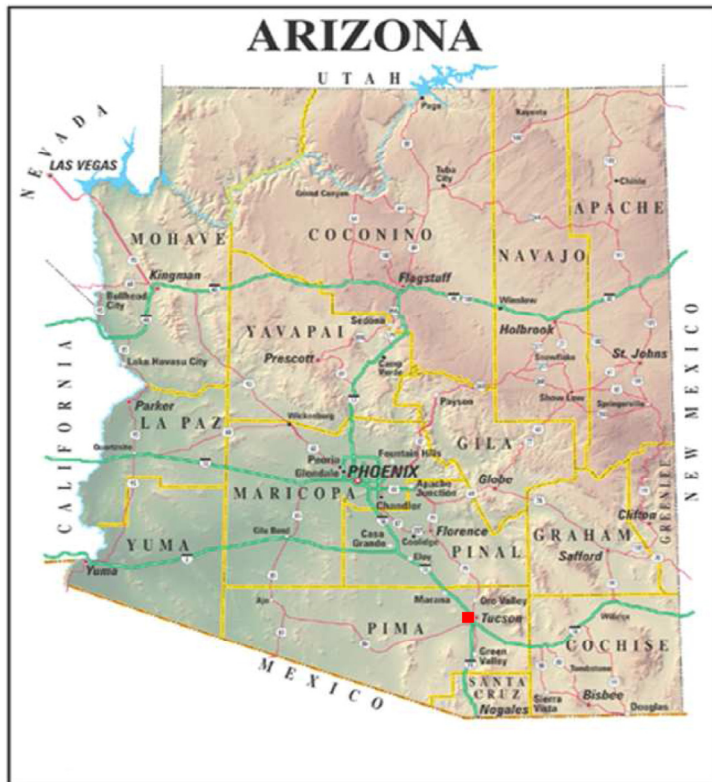


Figure 1.1. Location of Tucson Mountains in Arizona.

1.1 Geology of Tucson Mountains

The Tucson Mountain area is about 32 km long and up to 11 km wide and is one of many relatively small ranges that appear in the southwestern United States belonging to the Basin and Range Province. These ranges are the result of block faulting, which occurred about 10-15 million years ago, and today are separated by basins filled with thousands of feet of alluvial sediments derived from the erosion of these mountains. The Tucson Mountains consist primarily of volcanic rocks, dominantly rhyolite, and the entire mountain range is interpreted as a structurally disrupted interior of a volcanic caldera, in which the margins have been largely concealed by Tertiary basin fill (Lipman, 1993). The overall inferred dimensions of the Tucson Mountains Caldera are about 20 x 25 km; it is partially exposed in the Tucson Mountain area, and it is consistent with the observed size of other late Cenozoic calderas in the Western United States (Lipman, 1984). The age of the formation of this caldera has been inferred to be Jurassic and Laramide-age (Lipman and Sawyer, 1985).

The main geologic units exposed in the area of the Tucson Mountains, summarized from Lipman, 1993, are from younger to older:

Quaternary alluvium (Qal, Qf): Correspond to gravel, sand and silt filling the bottom and the slopes of the valleys. This unit includes alluvial-fan, alluvial and colluvial sedimentary deposits.

Tertiary volcanic and intrusive rocks (Tv, Ti): This sequence includes erosional remnants of a dacitic volcanic field in the northern Tucson Mountains, a stratified sequence of basaltic andesitic lavas and rhyolitic tuff along the east edge of the area, a dacitic-rhyolitic lava dome cluster along the south edge of the map area and small dikes and irregularly shaped small

intrusions.

Caldera-fill volcanic rocks (TKv, Kv): These units correspond to an interleaved caldera-filling mafic to silicic lava flows, tuffs and volcanoclastic sediments, preserved mainly in the southeastern and northern flanks of the Tucson Mountains. The southeastern rocks are considered younger than those in the northern flank on the basis of potassium-argon (K-Ar) dates.

Caldera-related Intrusions (Tki, Kg): Dikes, sills, small regular intrusions that range in composition from andesitic to silicic dikes, and the large granodioritic-granitic Amole pluton in the northern Tucson Mountains, which are considered to be associated with magmatic resurgence of the caldera and post-caldera volcanism.

Cretaceous Cat Mountain Tuff (Kc, Kcm): This is the main volcanic unit and corresponds to a thick intracaldera rhyolitic ash-flow tuff (72-74% of SiO₂) that varies greatly in welding and crystallization character laterally and vertically. This unit interfingers complexly with multiple horizons of lenticular and more irregular masses of chaotic mega-breccia. The tuff contains 10-30% phenocryst of quartz, altered feldspar, and biotite. The total thickness of the Cat Mountain Tuff, including the interleaved breccias, increases from only about 100 m in the southernmost part of the area to at least 4 to 5 km in the northern part of the mountain range.

Other Cretaceous rocks (Ks, Ktc): Corresponds to stratigraphically coherent pre-caldera Cretaceous rocks, that include a crystal-rich gray, welded rhyolitic tuff and a sedimentary package composed of siltstone, conglomerate and volcanic sandstones.

Jurassic and Triassic sedimentary and volcanic rocks (JT): This package includes interleaved red-brown sandstone and siltstone, dark-red-brown conglomerate containing abundant andesitic detritus, a basalt flow, and two rhyolitic ash-flow sheets.

Paleozoic-sedimentary rocks (Pz): Occur as clasts of limestone, dolomite, sandstone and quartzite in the mega-breccia member of the Cat Mountain Tuff.

Precambrian rocks (pC): Occur as clasts in the mega-breccia in the Cat Mountain Tuff, and are mainly composed of muscovite-bearing granites with potassium feldspar, and quartz-sericite schist.

The distribution of the rocks mentioned above is shown in Figures 1.2 and 1.3. Within the northern parts of the Tucson Mountains caldera fill, slide breccias dominate over ash-flow tuff. In contrast, in the southern caldera margin the thickness of the tuff decreases to only about 100 m, and the mega-breccia unit is virtually absent. On the west flank of the range, a small segment of the structural boundary of the caldera may be represented by the irregular Museum fault zone (Figure 1.2), which drops Cretaceous sedimentary rocks, probably part of the caldera floor, against Jurassic rocks. Along the northeast and southeast flanks of the Tucson Mountains, the Cat Mountain Tuff is conformably overlain by andesitic to rhyolitic lavas. These lavas obscure the northern and southern caldera margins. On the other hand, the granodioritic-granitic Amole pluton is exposed along the northwest flank of the Tucson Mountains, and appears to be a resurgent ring intrusion that arches the caldera fill, including postcaldera lavas upward to the east and north.

In several parts of the Tucson Mountains, northwest and northeast trending normal faults disrupt the caldera filling volcanic rocks with relatively small displacements (25-100m). These faults complicate the estimation of the thickness of the caldera fill because reliable stratigraphic markers are generally lacking in the area (Lipman, 1993). Many of these faults are related to the

middle Tertiary extension, but some may have formed in response to disruption of the caldera during the Cretaceous subsidence event.

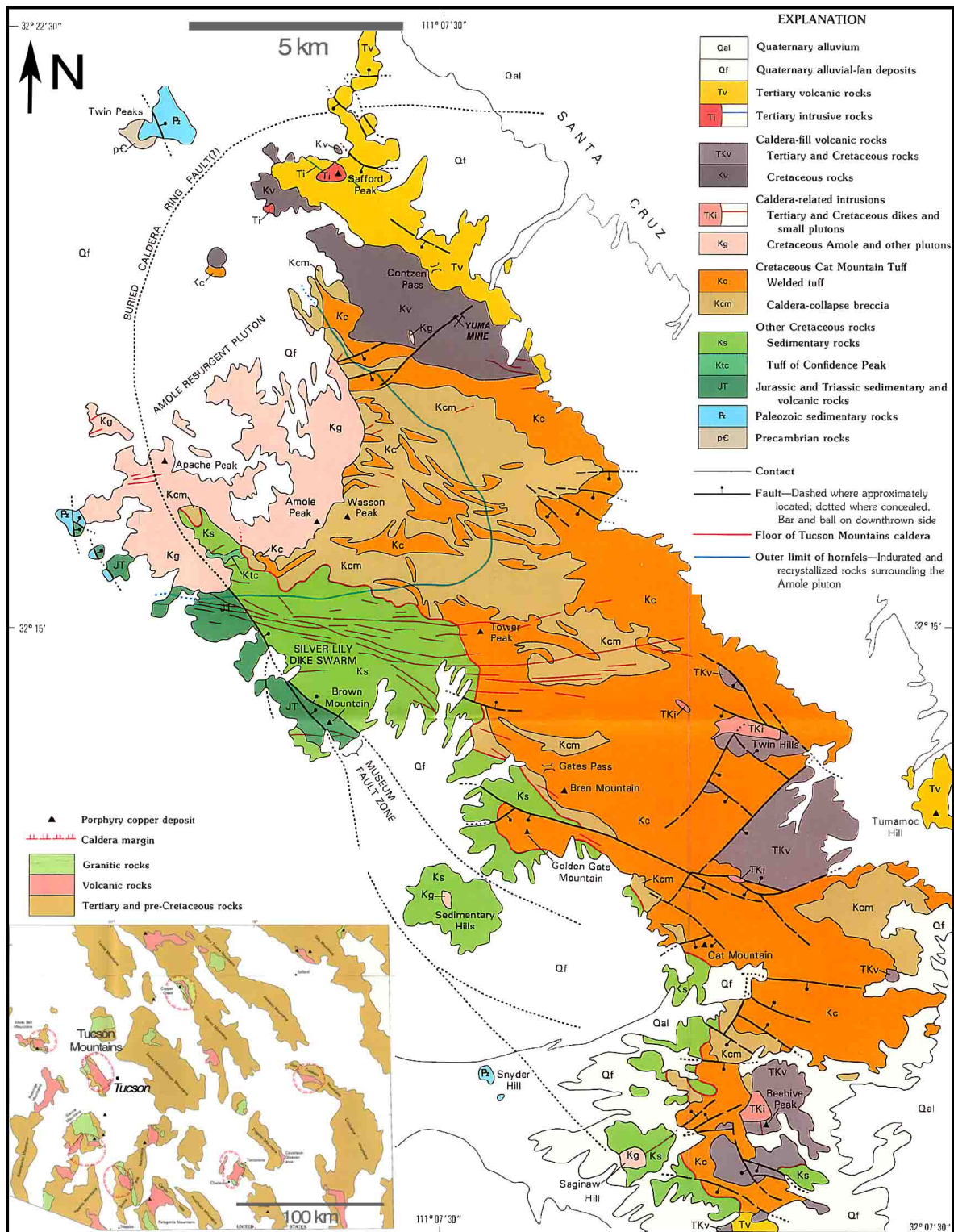


Figure 1.2. Simplified geological map of the Tucson Mountains, modified after Lipman, 1993.

Geology Map of Tucson

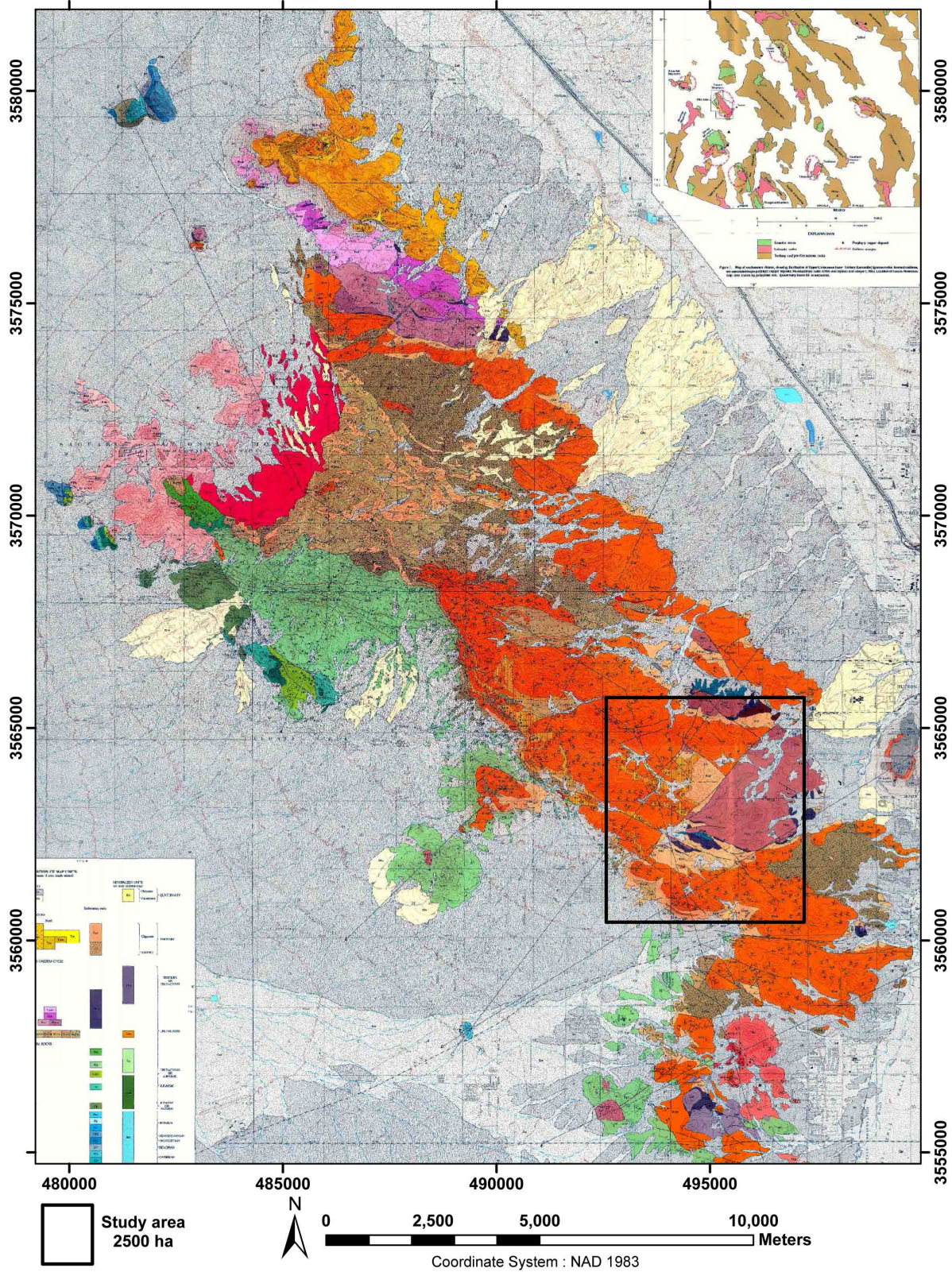


Figure 1.3. Geological map of the Tucson area.

LEGEND

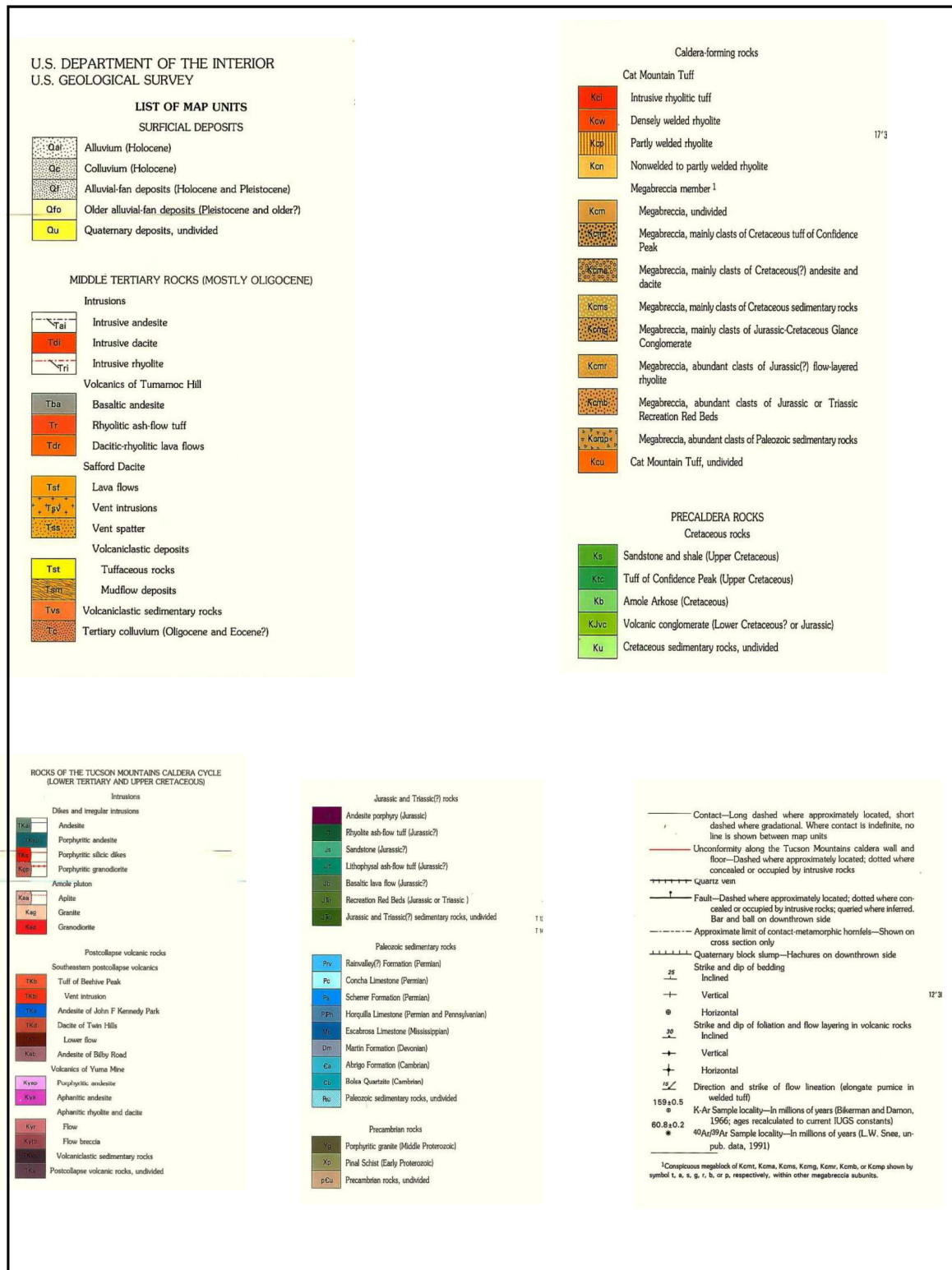


Figure 1.4. Legend for the Tucson area geological map.

1.2 Geographic location

The location of this study is within a rectangular shaped area whose UTM coordinates are:

492566E	497207E	497207E	492566E
3565710N	3565710N	3560433N	3560433N

Figure 1.5 indicates the study area on the topographic map of Tucson Mountains and Figure 1.6 shows the study area on an orthoimage.

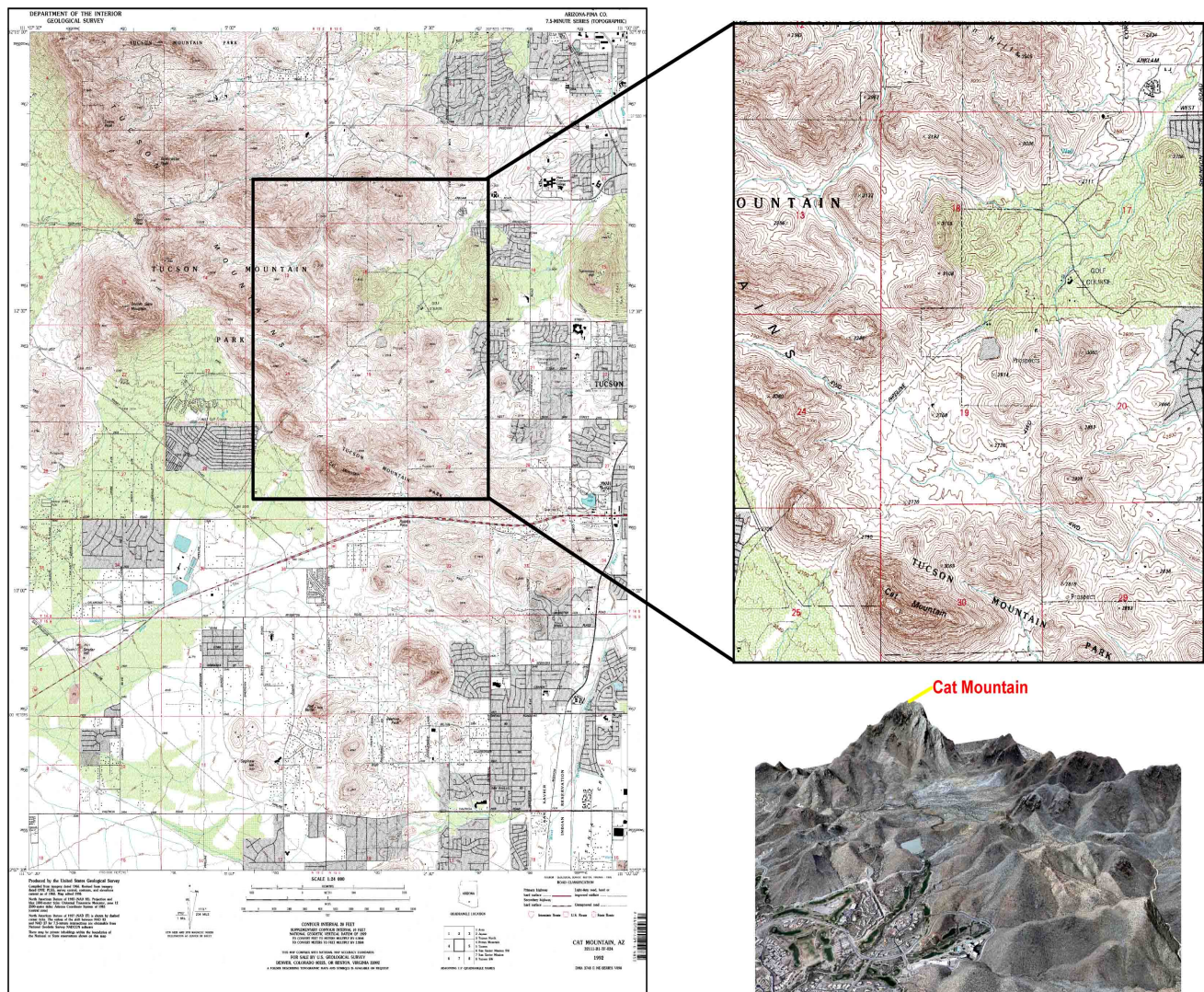


Figure 1.5. Location of study area on the topographic map of Tucson Mountains.

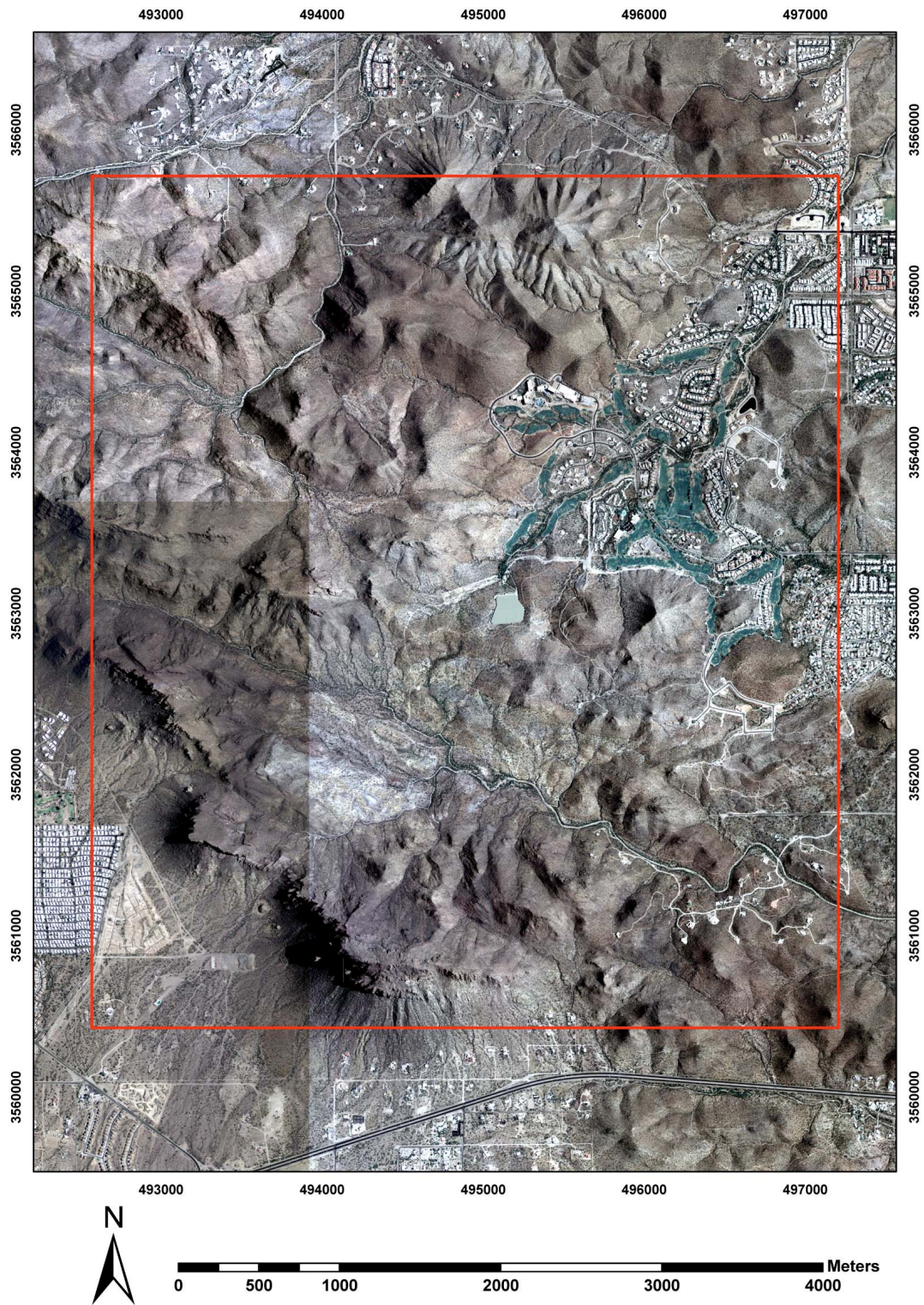


Figure 1.6. Location of study area – orthoimagery.

1.3 Objectives

One of the objectives of this project was to investigate and evaluate possible water resources in the southern part of the Tucson Mountains. Another objective of this project was to investigate the potential for storage of Compressed Air Energy (CAES) in porous rocks beneath the volcanic mountains. For this study, magnetic, gravity, Transient Electromagnetic (TEM) and Controlled Source Audio Magnetotelluric (CSAMT) methods were employed. Each of these geophysical methods can help identify potential locations of underground water in different ways. For example, TEM and CSAMT can determine the presence of conductive layers at depth. These conductive layers are typically related to porous and permeable, water saturated, sedimentary rocks in this type of geologic setting. These porous and permeable rocks could be potential reservoirs for water and for compressed air. The magnetic and gravity surveys may give us insight into fault locations and structure in the subsurface. The faults may provide suitable traps for compressed air energy storage.

This study used TEM data collected by the GEN/GEOS 416/516 Spring semester 2011 Geophysics Field Methods class, as well as some TEM data collected previously (Stokes and Sternberg, 2010). The class also collected magnetic and gravity data. For CSAMT data, the data described in Stokes and Sternberg, 2010 were processed by Zonge Engineering. Figure 1.7 shows the locations of the stations on a topographic map of the Tucson Mountains

Survey Map

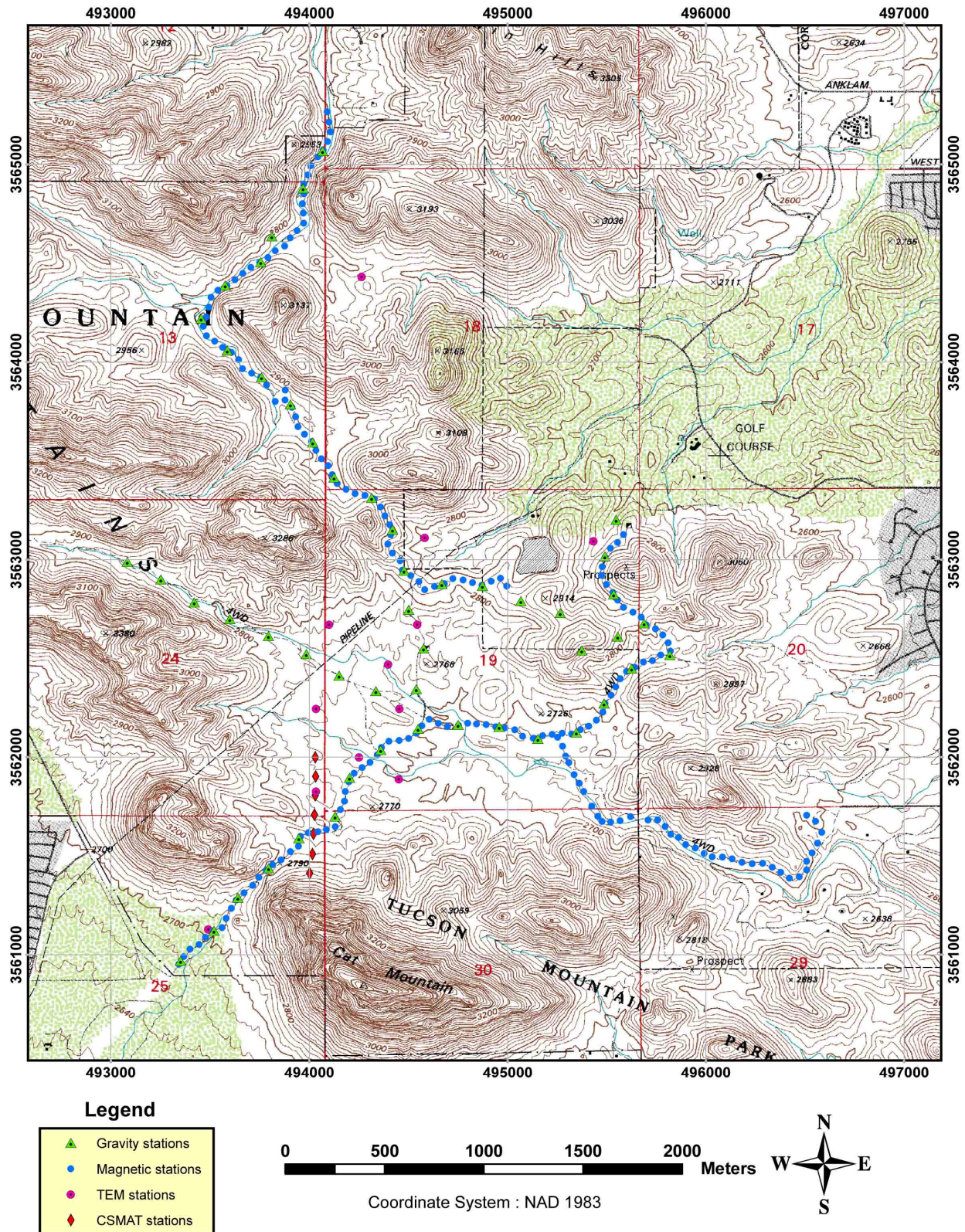


Figure 1.7. Location of the survey stations on a Topographic Map.

2. Transient Electromagnetic (TEM) Survey

2.1 Introduction

Transient Electromagnetic (TEM) soundings are a widely used exploration geophysics method for mapping subsurface layers. In this study, the TEM method was used to test the hypothesis of the presence of a conductive layer at depth, presumably a potential water resource, under the volcanic sequence. A total of 11 TEM sites were strategically recorded during 2010 and 2011 for this study (Figure 2.1), and the data, results and interpretation are described in this chapter.

2.2 Location

TEM data were recorded at eleven sites in the southern part of the Tucson Mountains area (Figures 2.1 and 2.2). The study area was approximately 3 x 4 km and the UTM coordinates for the center point are 3,562,500N and 494,500E. TEM sites 1, 2, 3, 4, 5a, 6 and 7 are located in the valley north of Cat Mountain. TEM site 8 is immediately southwest of Cat Mountain and TEM site 10 was located 1 km north of the valley. Also, sites 9 and 11 were located approximately 500 m northeast of the valley.

TEM sites 1, 2, 3, 4, 5, 6 and 7 were measured in 2010 prior to our class measurements, and were published in Stokes and Sternberg, 2010 and Stokes et al, 2010. Sites 1-6 used 500m X 500m loops and Site 7 used a 1000m X 1000m loop. Sites 1, 2, 5, and 6 were reoccupied in 2011 and new sites 8, 9, 10, and 11 were occupied as part of the work for the GEN/GEOS 416/516 Spring semester 2011 Geophysics Field Methods class, using 250m X 250m loops and a larger current in the transmitter loop. The larger current in 2011 (7.5A - 8.0A) provided a higher signal-to-noise ratio than the smaller current in 2010 (2.2A - 2.3A). This led to an improved depth of

TEM site	Easting	Northing	Elevation (m)	Loop size (m)
1	494041	3561828	843	500 x 500 250 x 250
2	494474	3561885	823	500 x 500 250 x 250
3	494061	3562244	836	500 x 500
4	494485	3562242	829	500 x 500
5a	494398	3562470	830	250 x 250
6	494563	3562660	840	500 x 500 250 x 250
7	494274	3562012	826	1000 x 1000
8	493491	3561129	826	250 x 250
9	495433	3563094	840	250 x 250
10	494264	3564432	866	250 x 250
11	494583	3563111	852	150 x 150

Figure 2.2. Table with the summarized data from the Tucson Mountains TEM sites.

2.3 Instrumentation and Field Procedures

These surveys utilized the Zonge International GDP32-II multi-channel receiver. This receiver was used in conjunction with a ZT-30 transmitter and an XMT-32 transmitter controller. The transmitter is capable of producing time-domain or frequency-domain waveforms into either resistive or inductive loads, and the controller produces timing signals for controlling the transmitter. The GDP32-II and the XMT-32 are synchronized together at the same frequency (8 Hz for this study). These instruments were provided and manufactured by Zonge International (formerly - Zonge Engineering).

The TEM surveys were performed using an in-loop array for a vertical sounding, with 500 x 500 m and 250 x 250 m loop size, with two exceptions, one 1000 m x 1000 m (TEM site 7) and a 150 x 150m loop (TEM site 11). The transmitted current for the 2011 survey loops ranged between 7.5 and 8.0 Amps; with the exception of TEM site 11 in which the current used was 11.2 Amps. The transmitted current for the 2010 survey loops ranged between 2.2 and 2.3 Amps.

We tried to keep the transmitter loops away from fence lines, pipelines, power lines and other cultural features that could affect the measurements. However, Station 11 was affected by conductive interference produced by the proximity of a barbed wire fence with metal posts. Therefore, the Station 11 results were not used in the interpretation. Station 9 was located near a Tucson Water Reservoir. We learned from Tucson Water that this reservoir has a metal rebar reinforced concrete liner. We, therefore, also eliminated station 9 in the final interpretation because of potential interference from this large metal structure.

2.4 Data Processing

The TEM data obtained from the surveys were stored in the GDP32-II receiver and then downloaded and saved, in its raw form, to a desktop computer in the Mining and Geological Engineering Department at the University of Arizona. The raw data were sorted and organized and then processed using Zonge International's proprietary suite of software called DATPRO. Then, the data were trimmed or edited for values that had a large error or were inconsistent with the decay trend. The file was then run through STEMINV, in order to invert the measured data into a smooth model of the resistivity variation with depth. The one-dimensional inversions for each TEM site are shown in Figures 2.3 to 2.13. A comparison of the measured decay curve data

and the best-fit calculated decay curve is shown on the left side of each figure, and in red are the values considered too noisy that were deleted prior to the smooth inversion. On the right side of the figures, a plot of the best-fit smooth model of resistivity versus depth is shown.

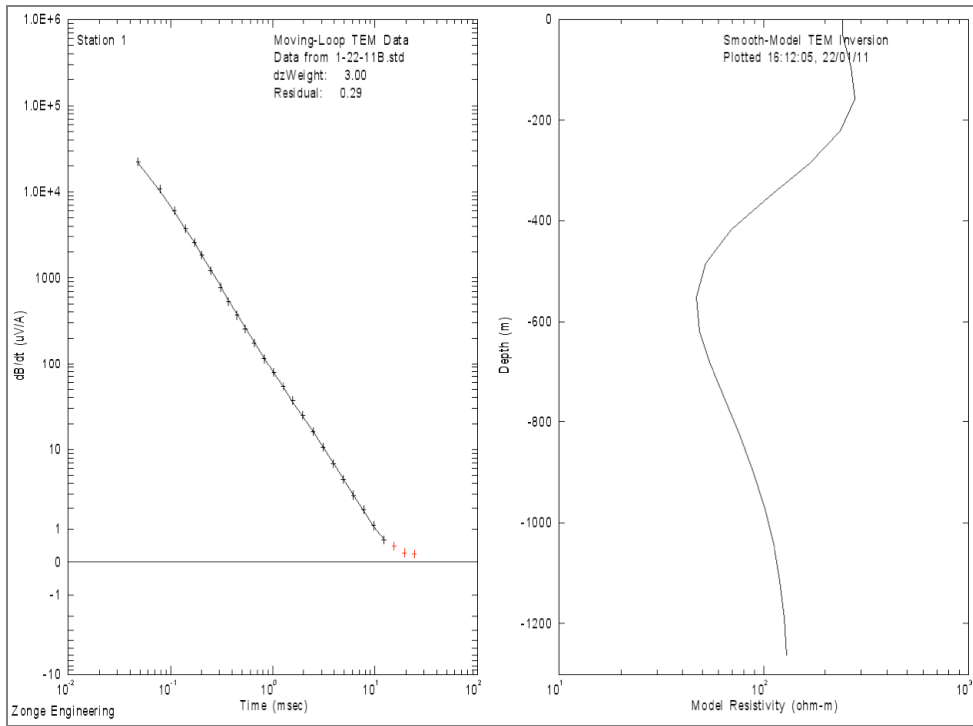


Figure 2.3. TEM loop 1 smooth inversion.

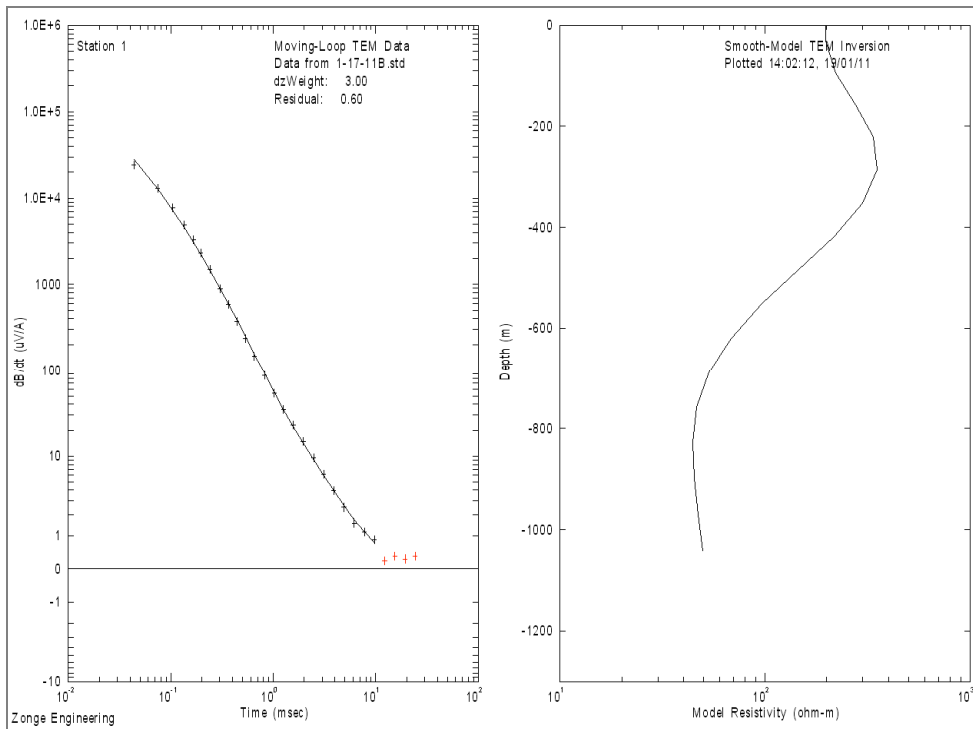


Figure 2.4. TEM loop 2 smooth inversion.

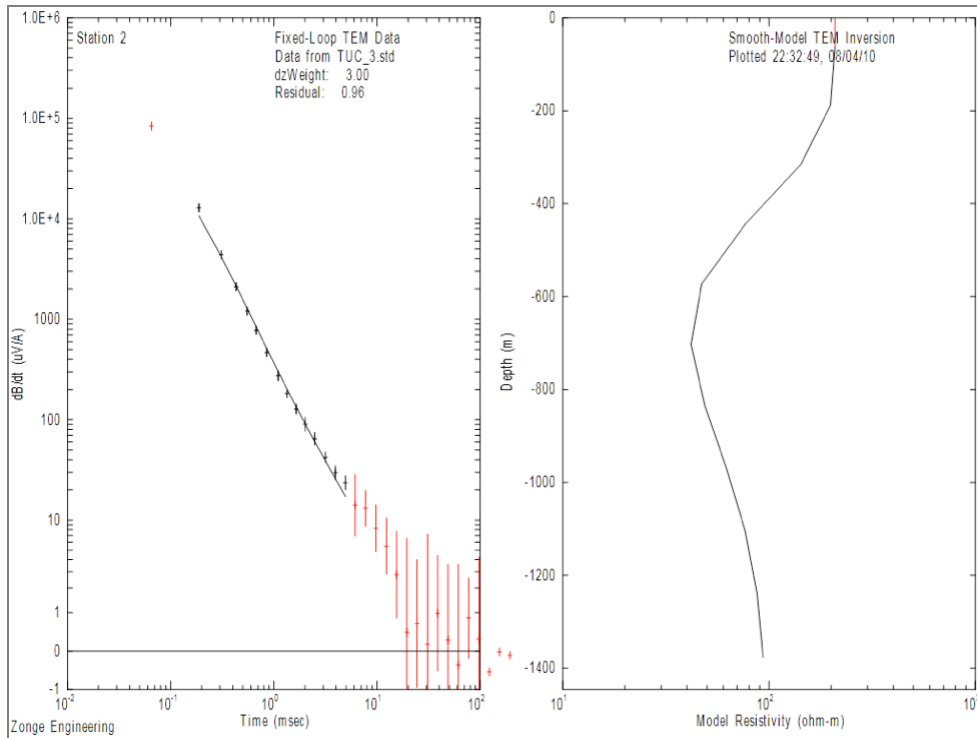


Figure 2.5. TEM loop 3 smooth inversion.

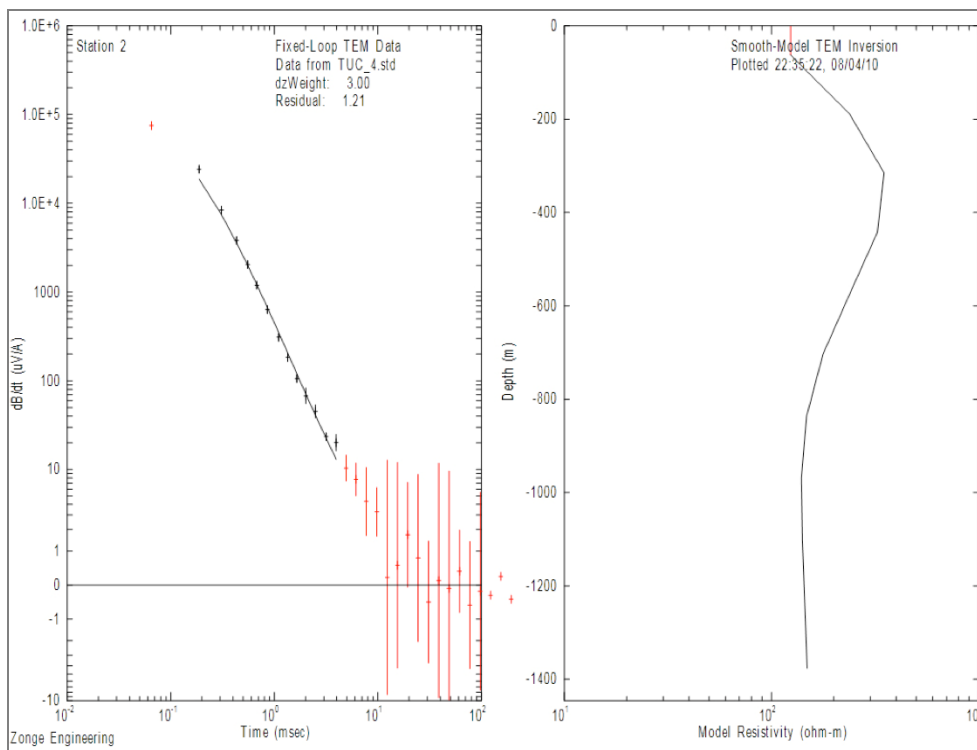


Figure 2.6. TEM loop 4 smooth inversion.

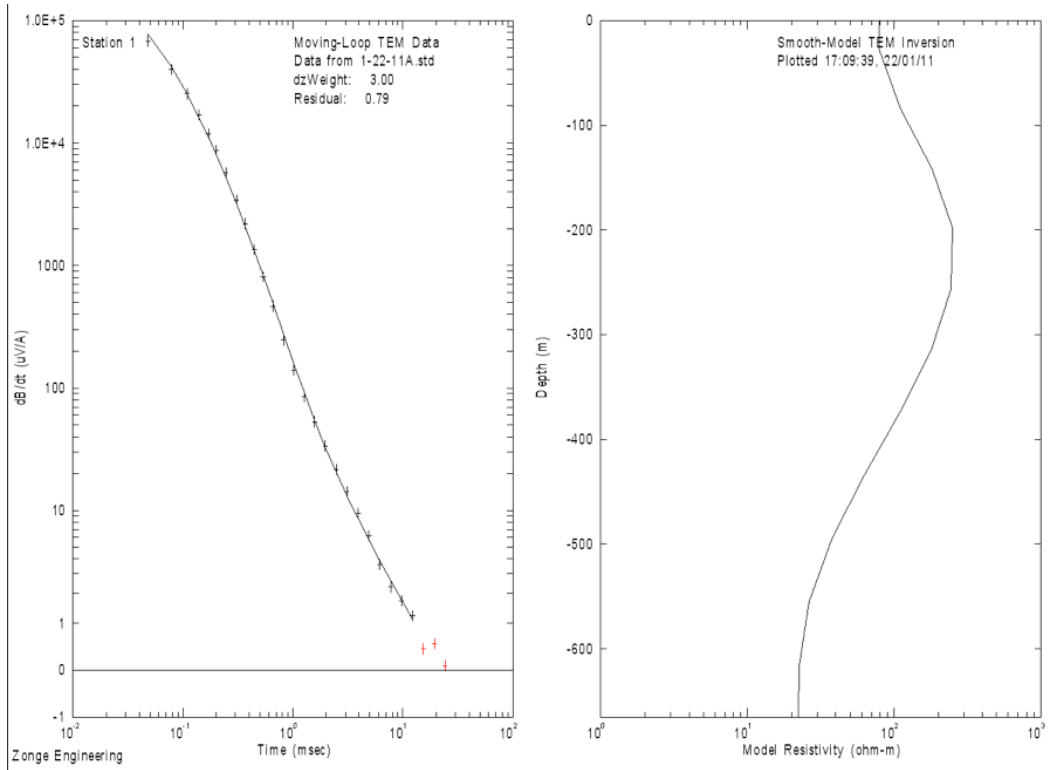


Figure 2.7. TEM loop 5a smooth inversion.

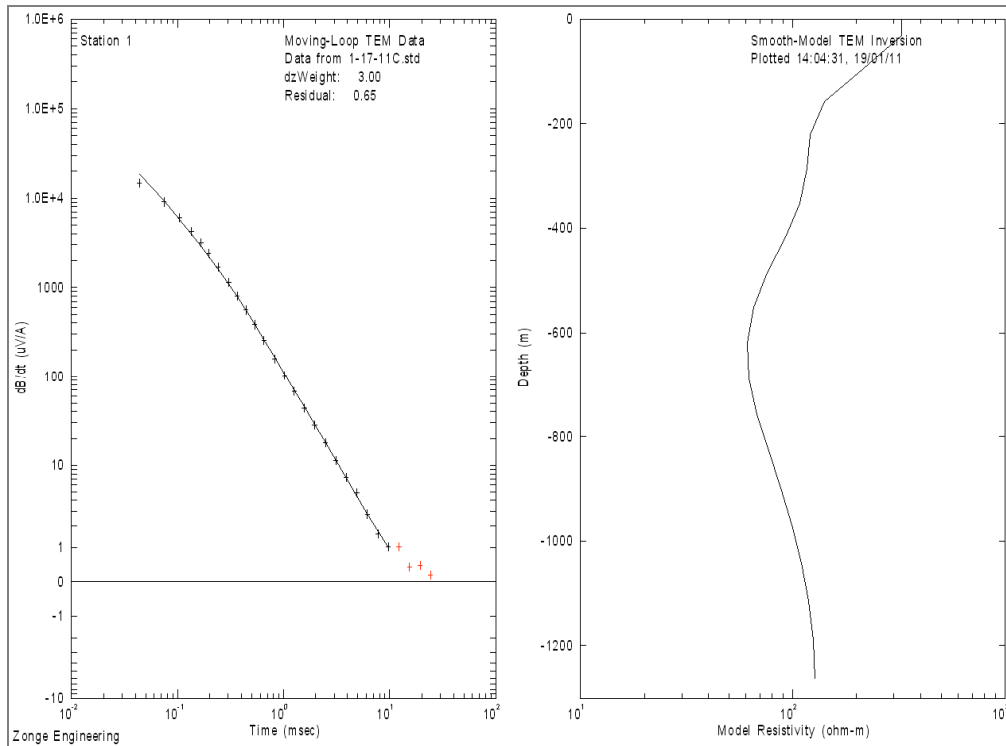


Figure 2.8. TEM loop 6 smooth inversion.

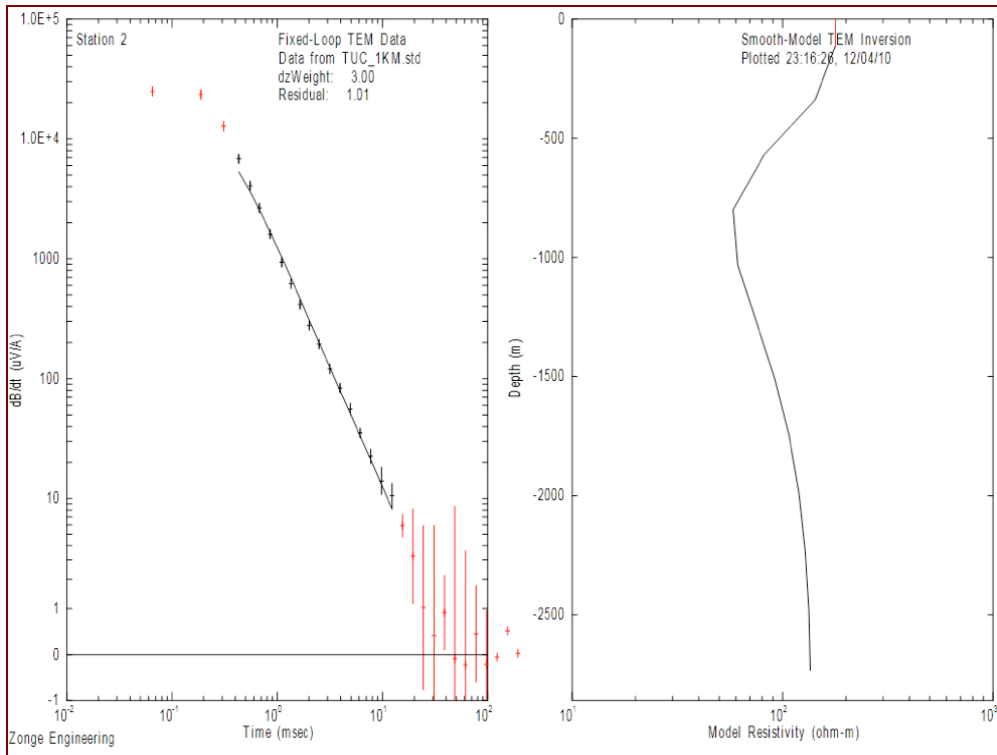


Figure 2.9. TEM loop 7 smooth inversion.

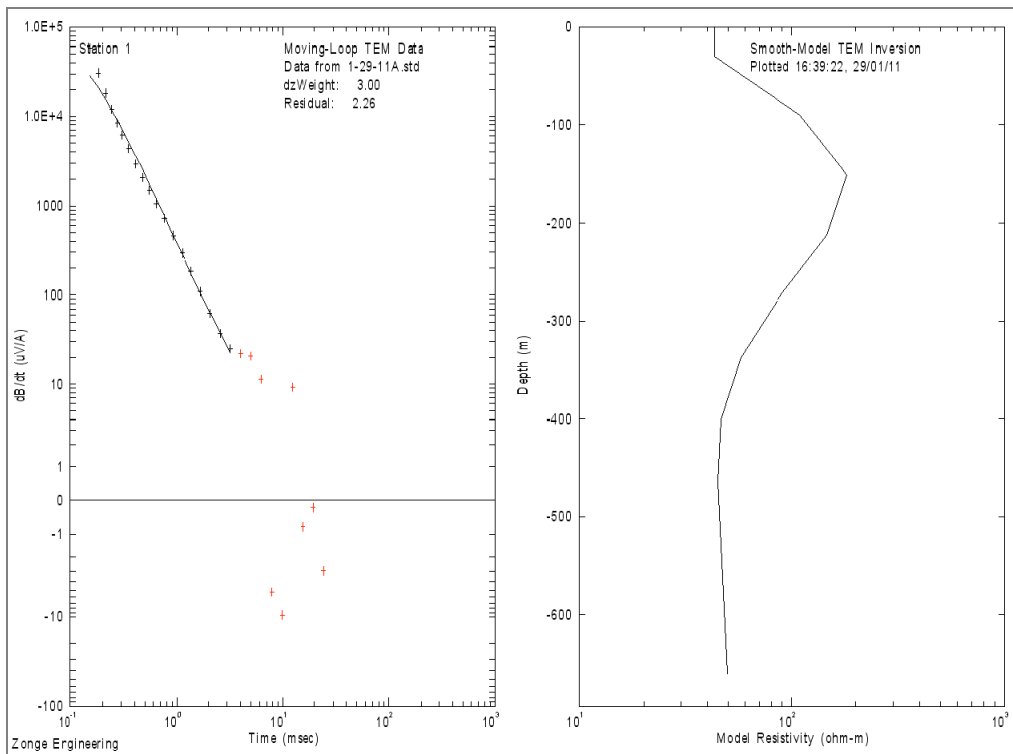


Figure 2.10. TEM loop 8 smooth inversion.

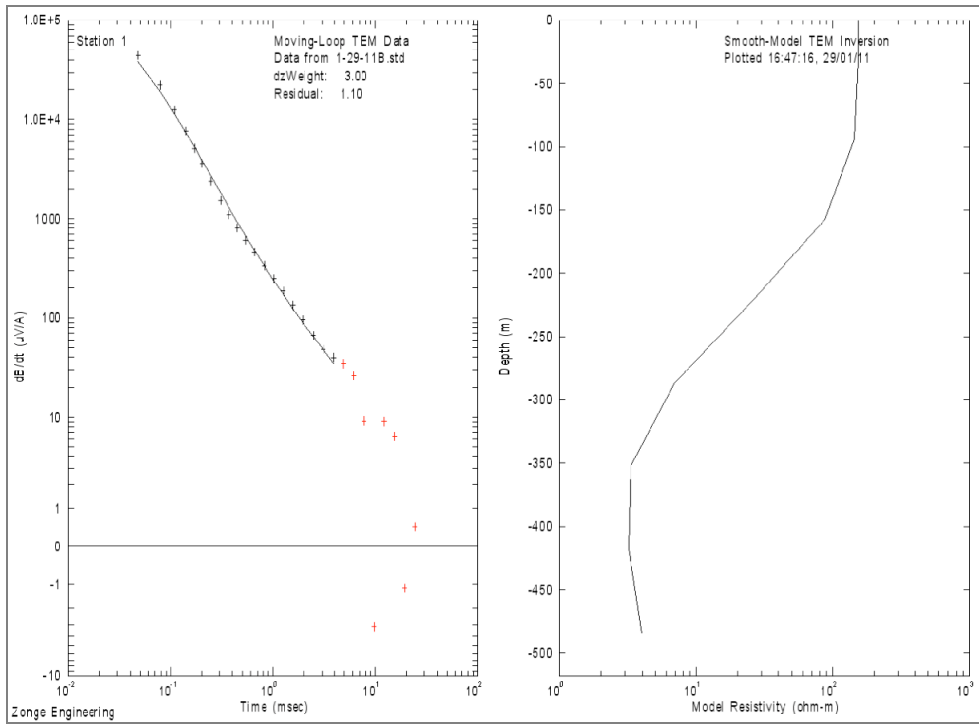


Figure 2.11. TEM loop 9 smooth inversion.

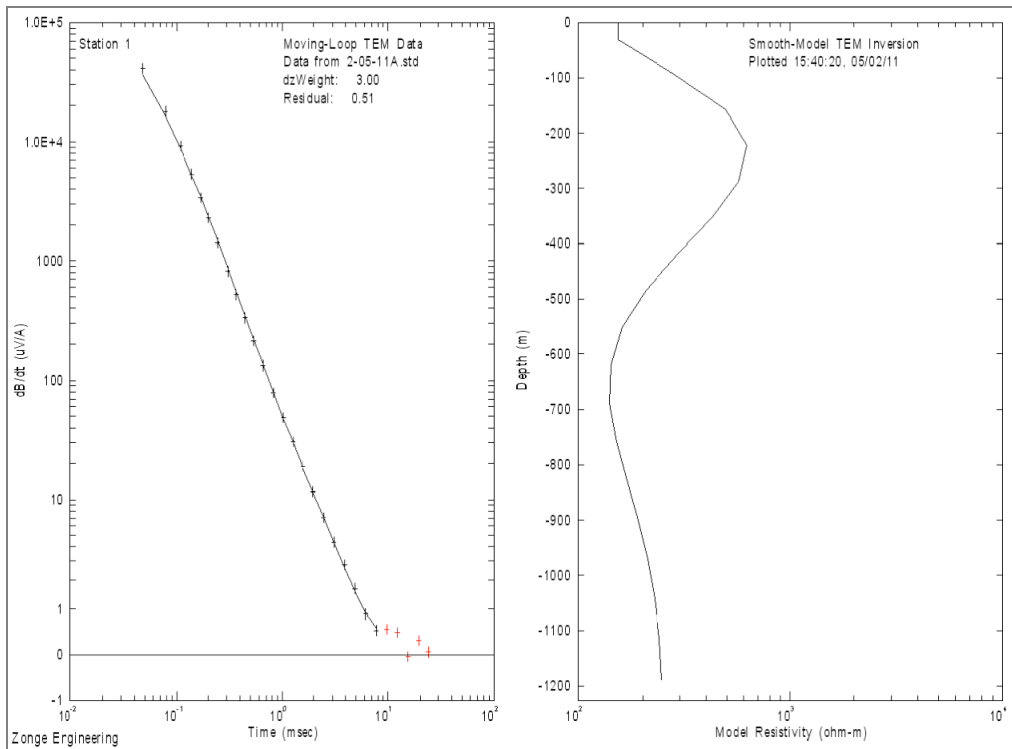


Figure 2.12. TEM loop 10 smooth inversion.

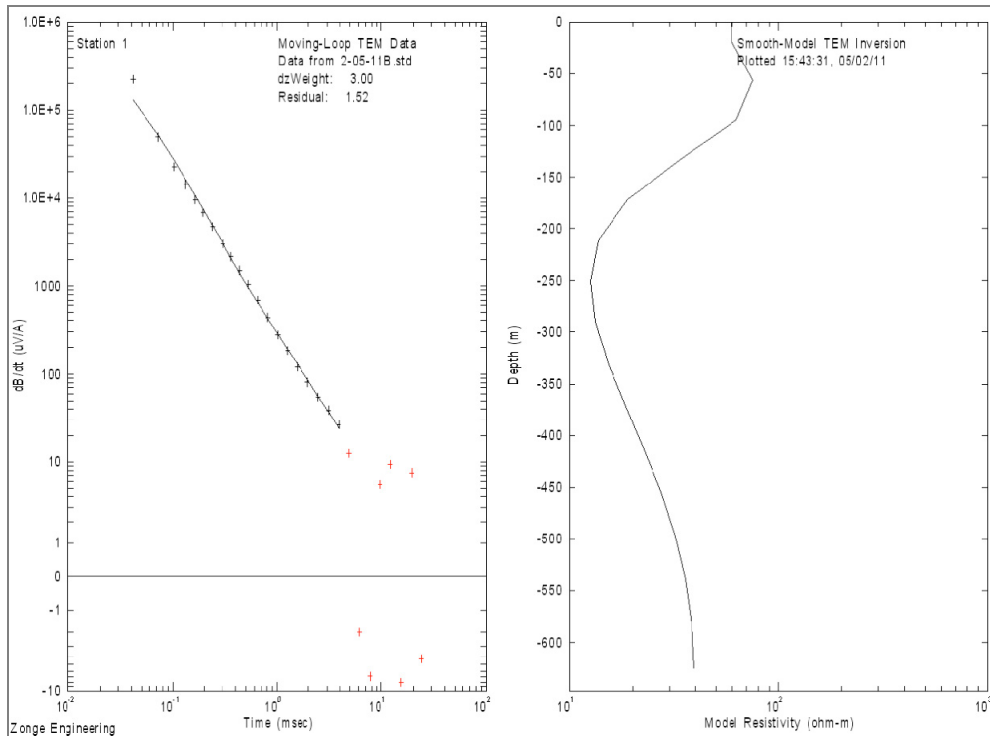


Figure 2.13. TEM loop 11 smooth inversion (potentially affected by cultural interference).

2.5 Layered-Earth Modeling

Further modeling of the TEM data was done using the IX1Dv3 software provided by Interpex Limited. This software allows one to iteratively perform forward and inverse modeling, and to create a discrete layered-earth model with an equivalence analysis calculation. The inversion process uses an Inman style ridge regression approach of nonlinear least-squares curve fitting (Inmann, 1975). The last step includes editing or trimming the data to avoid outliers or inconsistent values. Then, an initial layered-earth model is input into the software, in order to give constraints to the inversion, including the number of layers to be modeled. The procedure is intended to fit the modeled response decay curve with the measured data. Finally, multiple inverse iterations are performed in order to obtain a new layered-earth model, including an equivalence analysis calculation.

Figures 2.14 to 2.24 show the results for the TEM sites. On the left side of the figures, the apparent resistivity (Ohm-m) versus time (ms) is plotted showing the measured data and the modeled decay curve. On the right side of the figures, a section with depth (m) versus resistivity (Ohm-m) shows the earth-layered model with the equivalence analysis calculation.

In addition to the inversion and layered-earth modeling produced with the IX1Dv3 software, two contour plan maps were produced using the Surfer Gridding and Contouring program from Golden Software. These contour maps estimated depth from the surface to the top of the underlying conductive layer and show the differences in depth of this layer in elevation (above sea level). The interpolation algorithm used for these contour maps was kriging. These maps include all TEM sites, with the exception of station 11, which was not considered in the interpretation due a potential cultural interference. Figure 2.25 shows the differences in real elevation, and Figure 2.26 shows the depth from the surface to the top of the conductive layer for the study area.

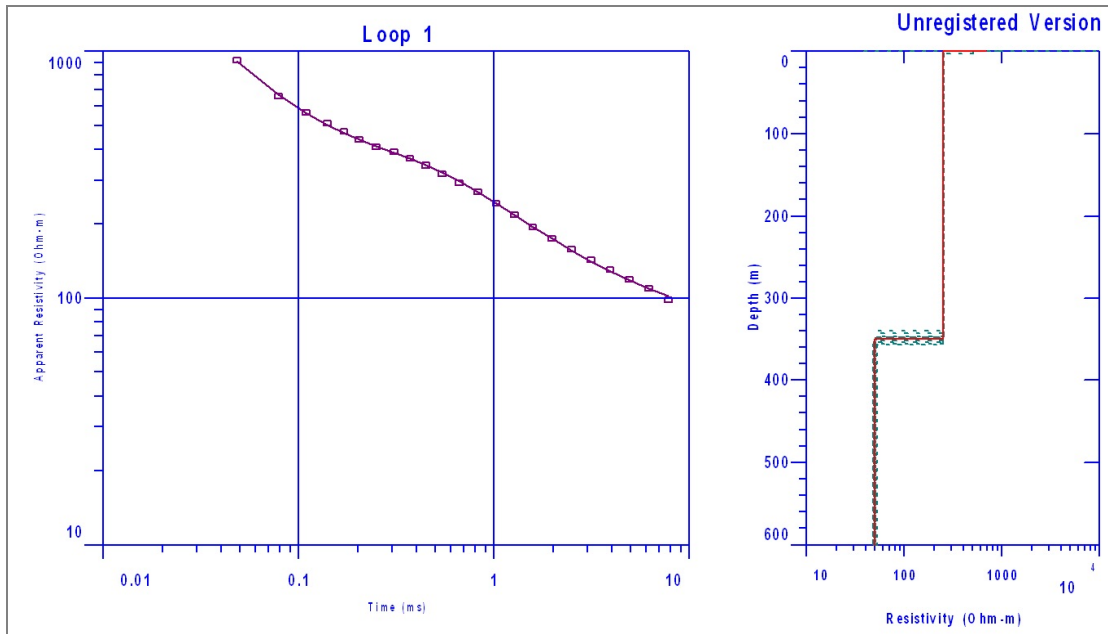


Figure 2.14. TEM loop 1 IX1D inversion model and equivalence analysis.

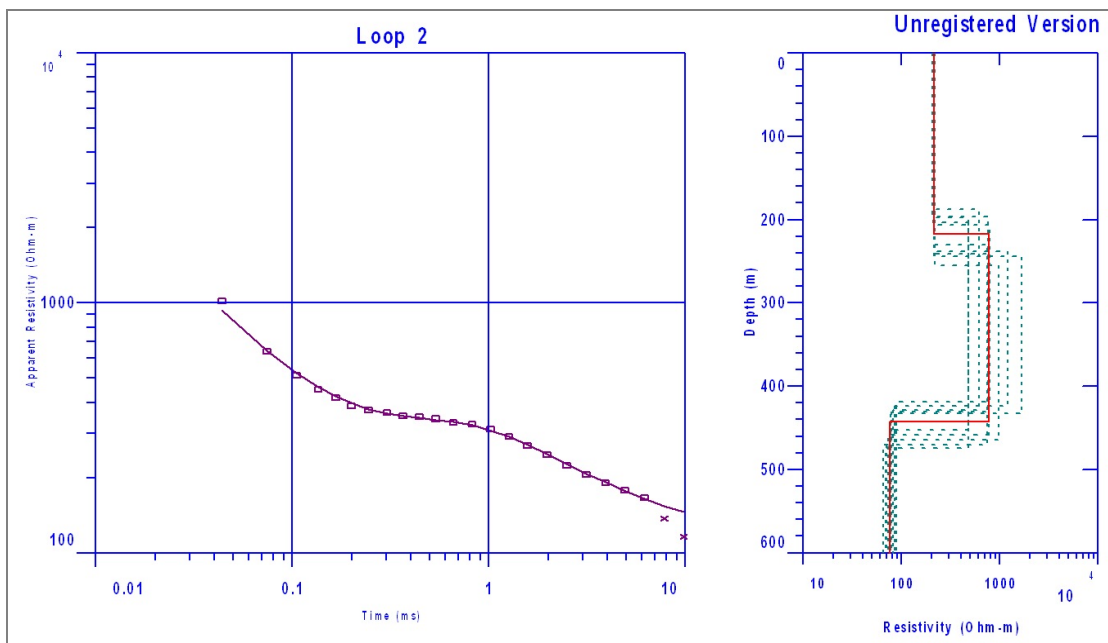


Figure 2.15. TEM loop 2 IX1D inversion model and equivalence analysis.

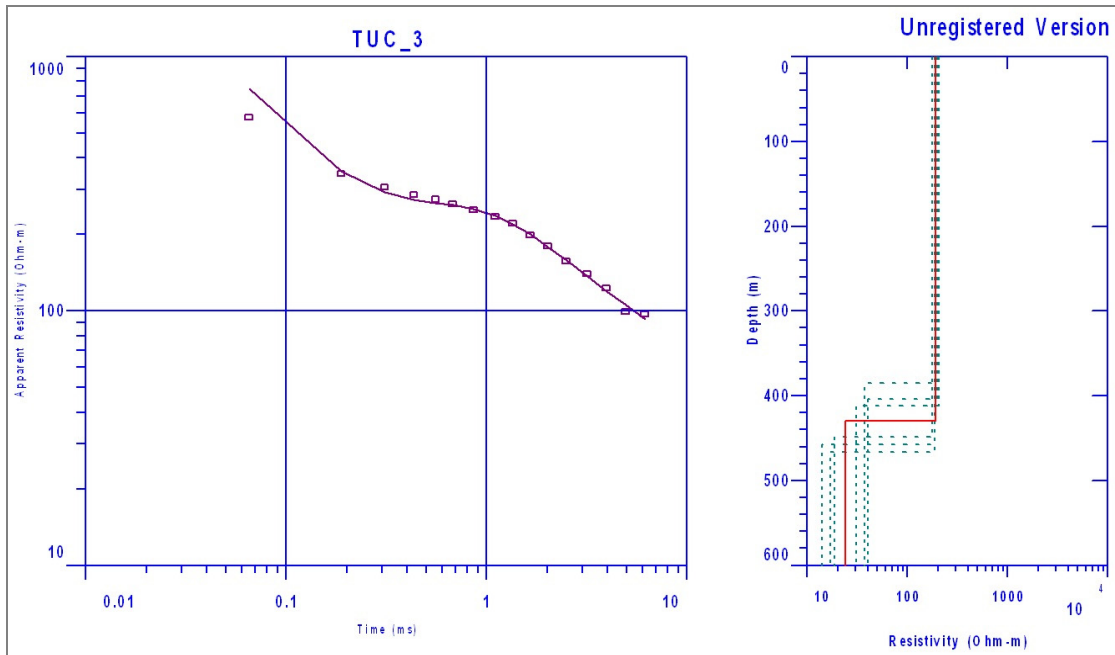


Figure 2.16. TEM loop 3 IX1D inversion model and equivalence analysis.

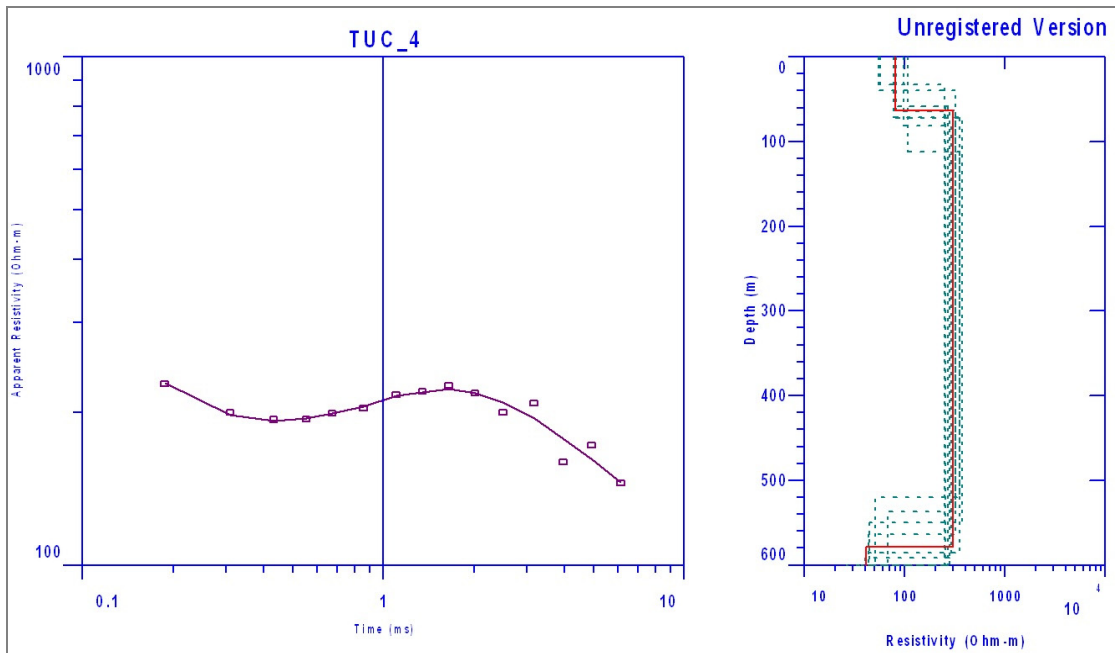
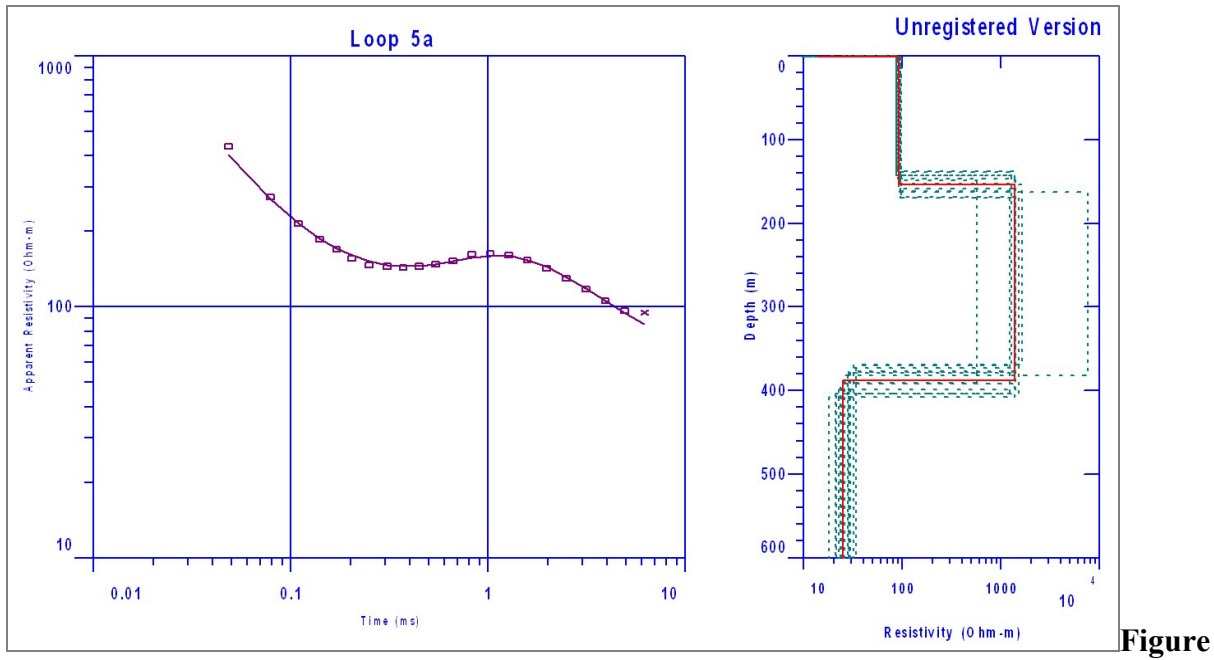


Figure 2.17. TEM loop 4 IX1D inversion model and equivalence analysis.



Figure

2.18. TEM loop 5a IX1D inversion model and equivalence analysis.

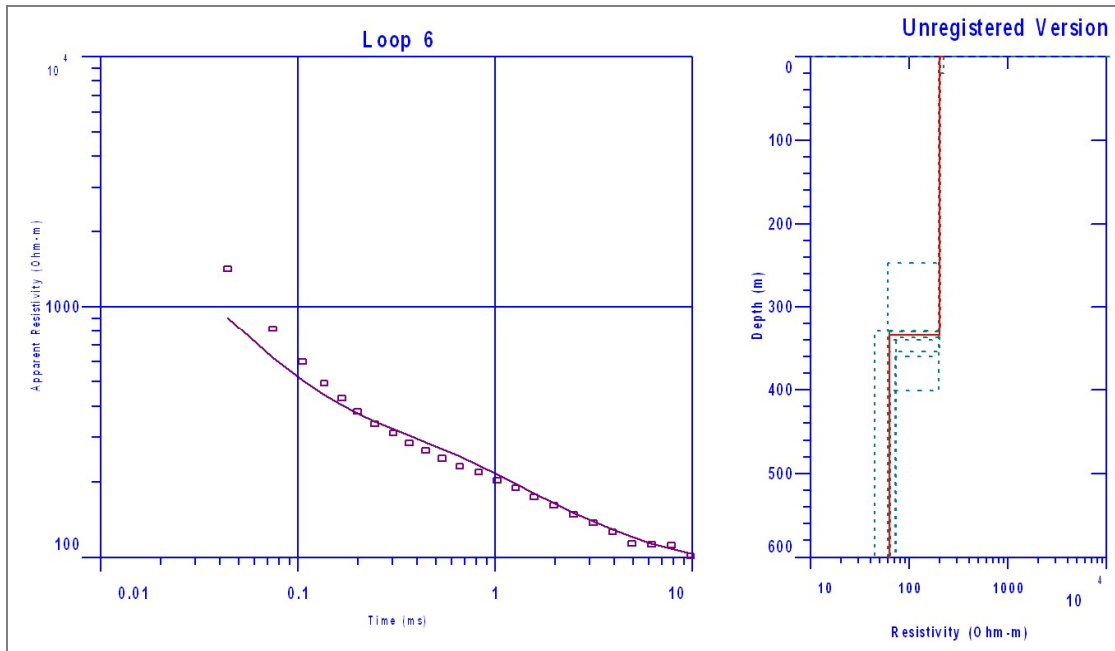


Figure 2.19. TEM loop 6 IX1D inversion model and equivalence analysis.

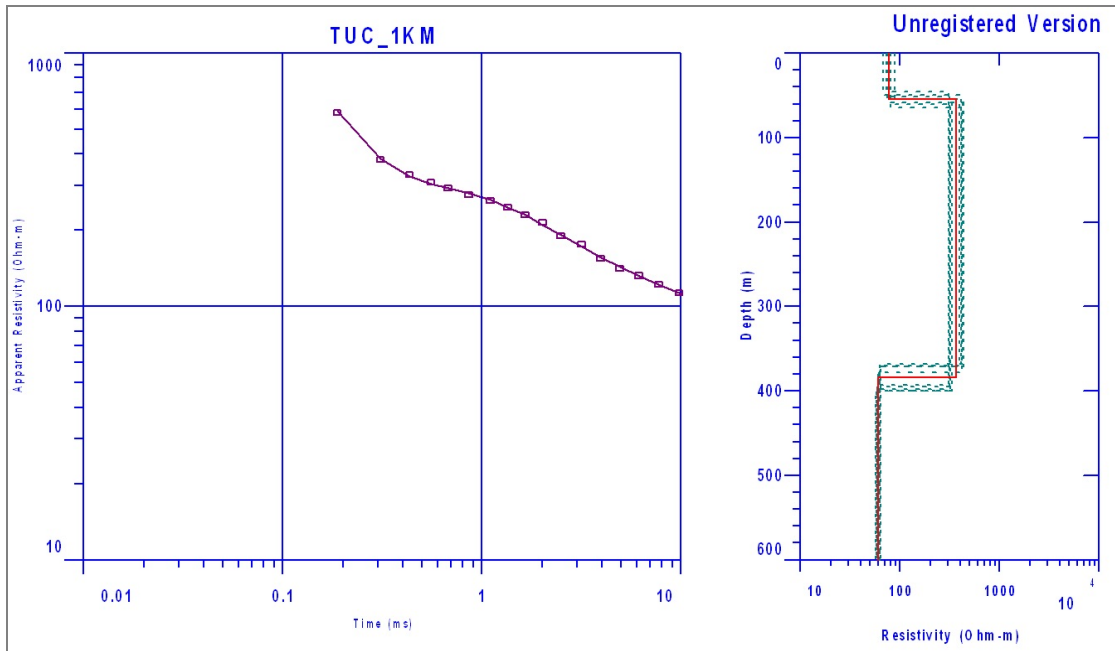


Figure 2.20. TEM loop 7 IX1D inversion model and equivalence analysis.

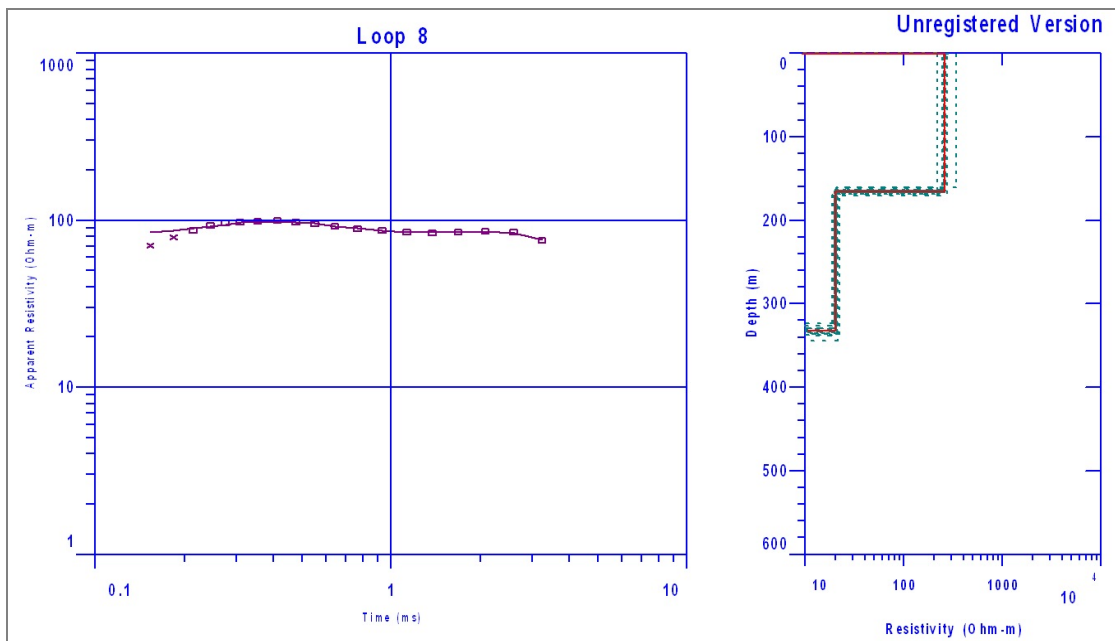


Figure 2.21. TEM loop 8 IX1D inversion model and equivalence analysis.

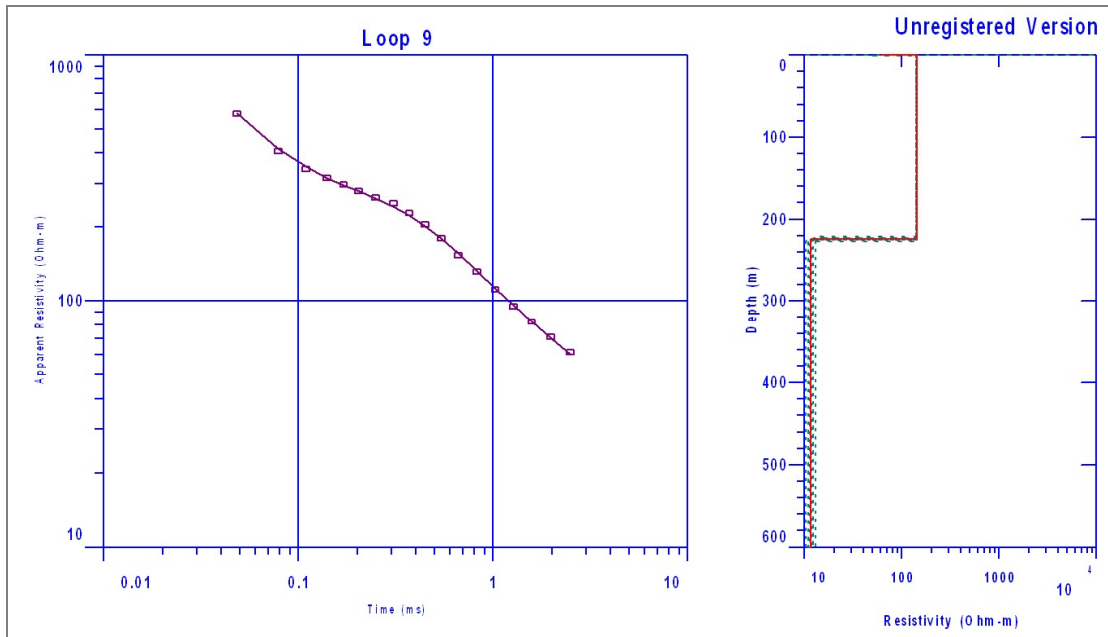


Figure 2.22. TEM loop 9 IX1D inversion model and equivalence analysis.

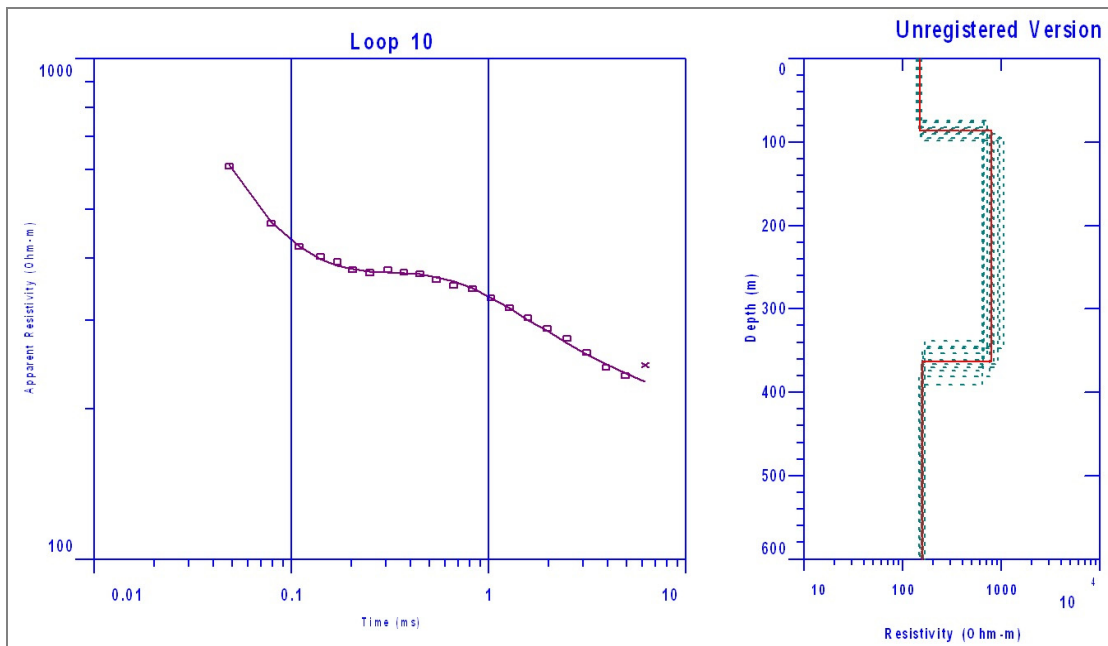


Figure 2.23. TEM loop 10 IX1D inversion model and equivalence analysis.

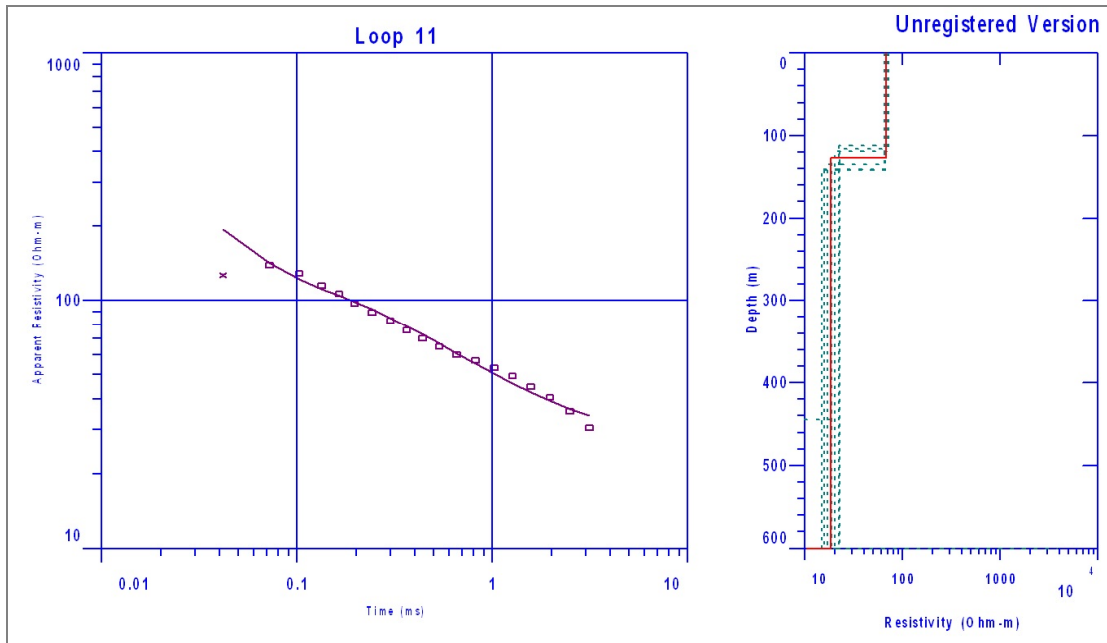


Figure 2.24. TEM loop 11 IX1D inversion model and equivalence analysis (potentially affected by cultural interference).

ELEVATION OF CONDUCTIVE LAYER

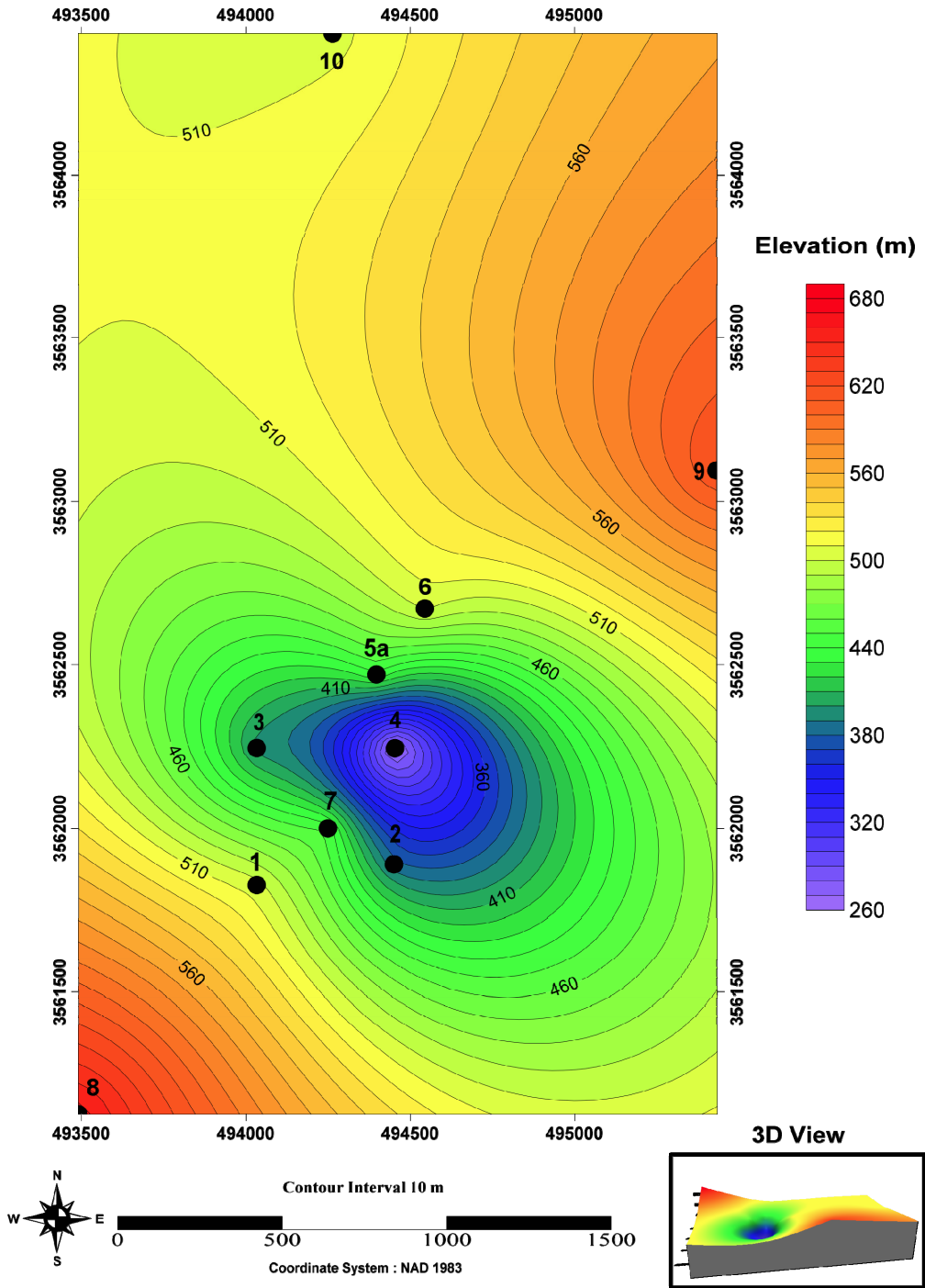


Figure 2.25. TEM contour plan map showing the real elevation every 50 m (above sea level) of the top of the conductive layer.

DEPTH OF CONDUCTIVE LAYER

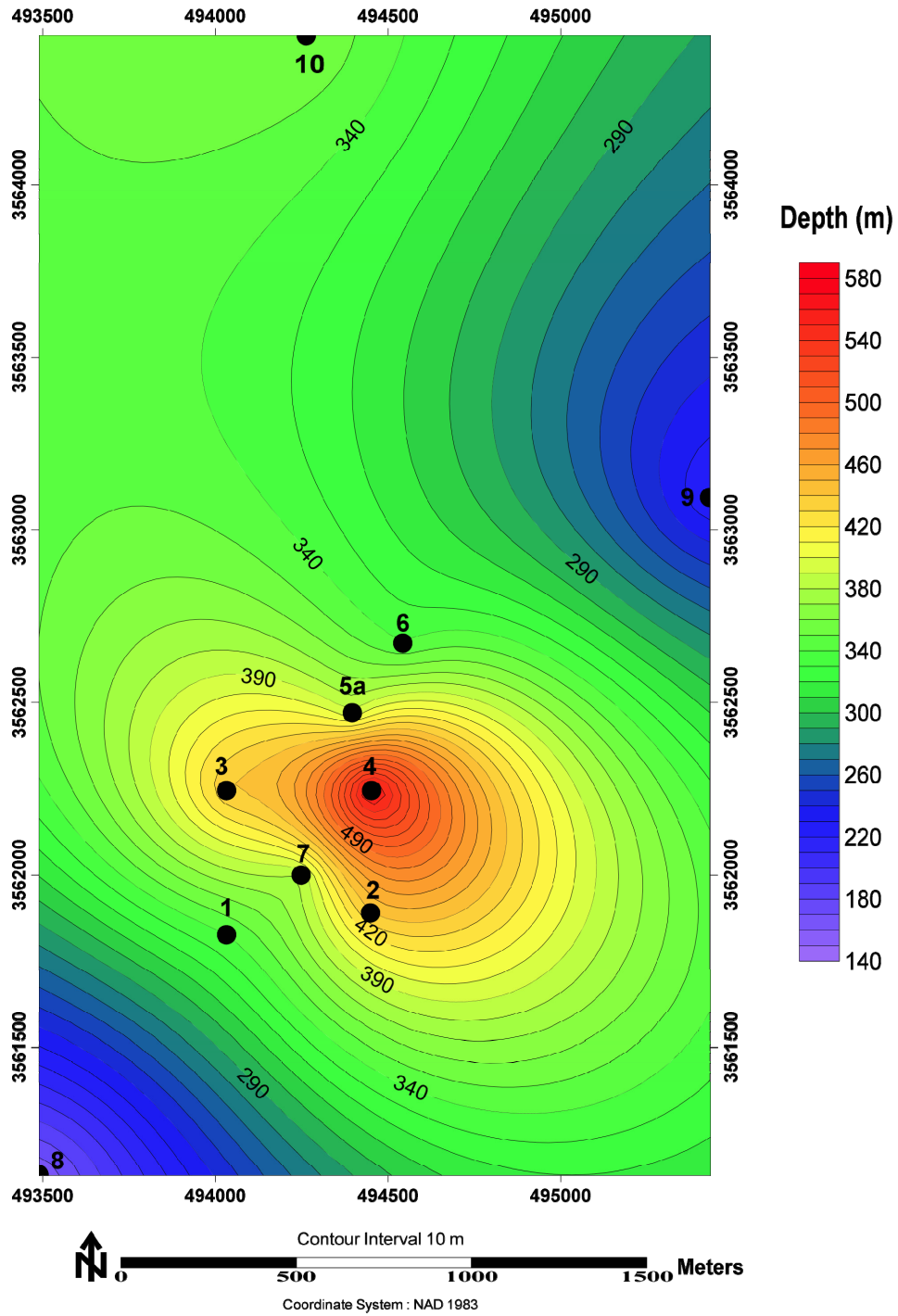


Figure 2.26. TEM contour plan map showing the depth from the surface to the conductive layer.

The layered-earth interpretations for TEM sites 1, 2, 3, 5a, 6, 7 and 10 show a bottom of the resistive layer between 320m and 450m depth from the surface, and resistivities of the resistive layer from 200 to more than 1000 (Ohm-m). At TEM sites 8 and 9, the bottom of the resistive layer is at a much shallower depth, in the range of 120 to 230 m and resistivities of the resistive layer are between 150 and 200 (Ohm-m). TEM site 4 shows a deeper depth to the bottom of the resistive layer at 580 m with 300 Ohm-m.

The results for TEM sites 1, 2, 3, 5a, 6, 7 and 10 are consistent with the hypothesis of a conductive rock layer (and presumably a potential water resource) beneath the volcanic rocks in the Tucson Mountains area. TEM sites 8 and 9 located in the southwest and northeast boundaries of the valley, show that the conductive layer is shallower (Figure 2.25). Finally, TEM site 4 recorded in the lowest topographic part of the valley, gives evidence of a larger depth to the top of the conductive layer.

2.6 Comparison with Geological Sections

The TEM sites with exception of site 11, were projected onto four interpreted geological cross sections from Lipman (1993). Sections C-C', D-D' and F-F' (from Lipman) and section G-G' (adapted from the Lipman data) are shown in Figure 2.27. Section G-G' was produced by projecting the geological contacts and dips of the main units into the profile. Then, faults and their relative movements were inferred from the geological map from Lipman, 1993. The thickness and the stratigraphic variations of the units at depth were interpreted following the closest existing geological cross-sections. The projection of the sites was made by taking into consideration the surface lithology, the strike and dip of the beds, the presence of faults, and

ultimately the distance from the geological cross-section. The comparisons between the modeled TEM sites with the geological cross-sections are shown in Figures 2.28 to 2.31. On the upper part of the figures is the TEM projection along the cross section, showing the layered-earth models with the equivalence analysis. The lower part of the figures shows the interpreted geological cross-section with the TEM projection superimposed on top of the interpreted geologic section.

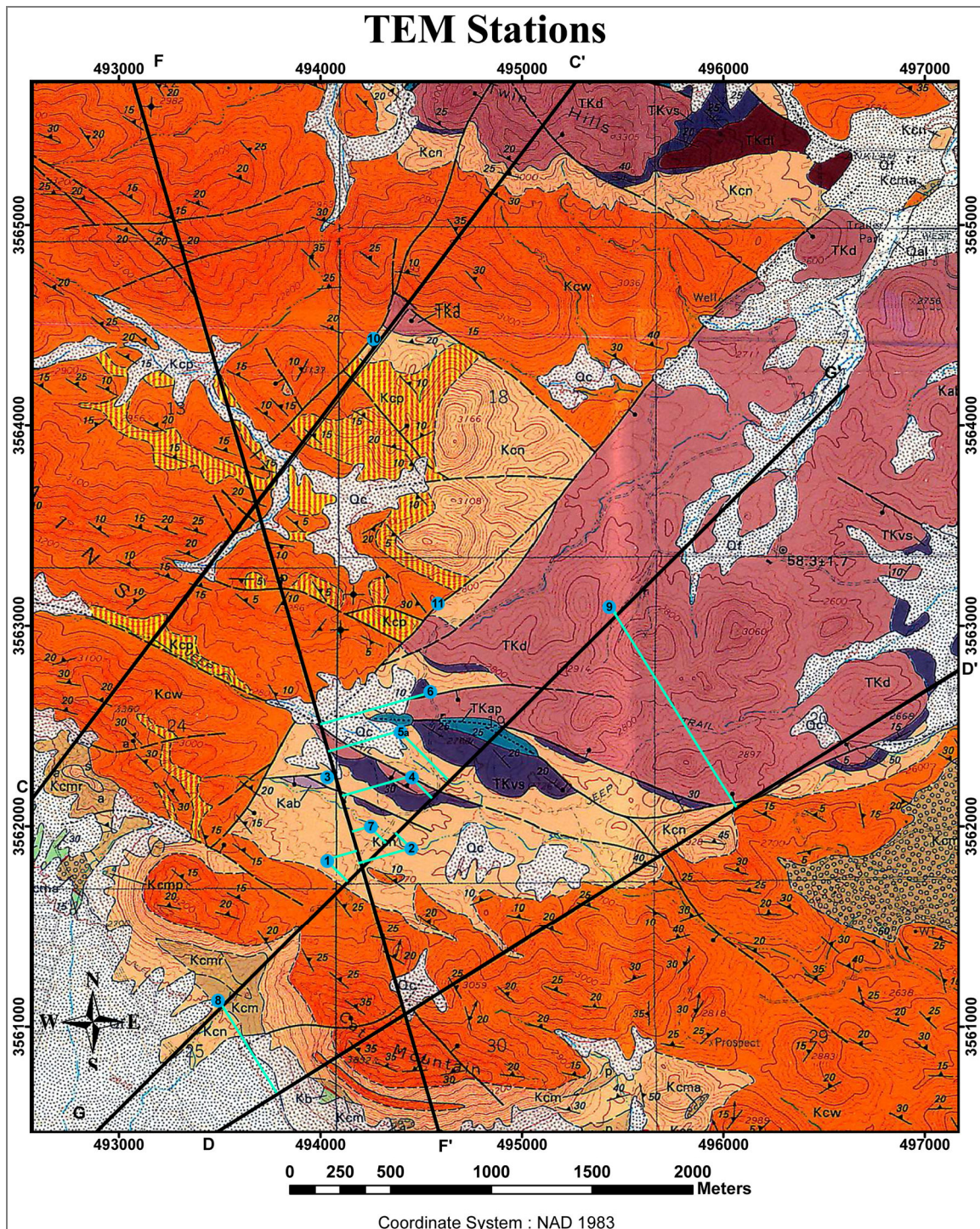


Figure 2.27. Map showing the locations and the projections of the TEM station loop centers on the different geological cross sections.

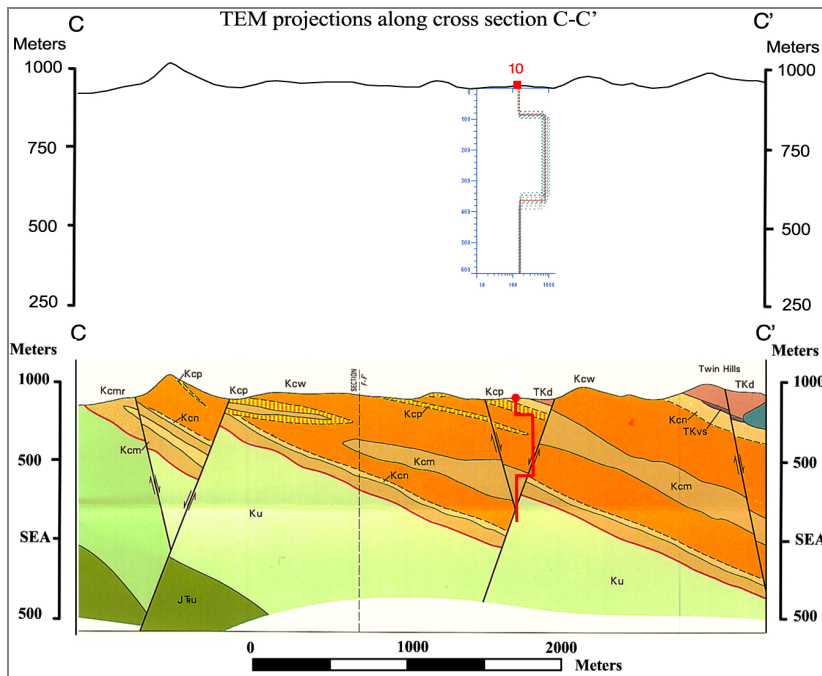


Figure 2.28. Comparison of TEM inversion model with C-C' interpreted geological cross section from Lipman, 1993.

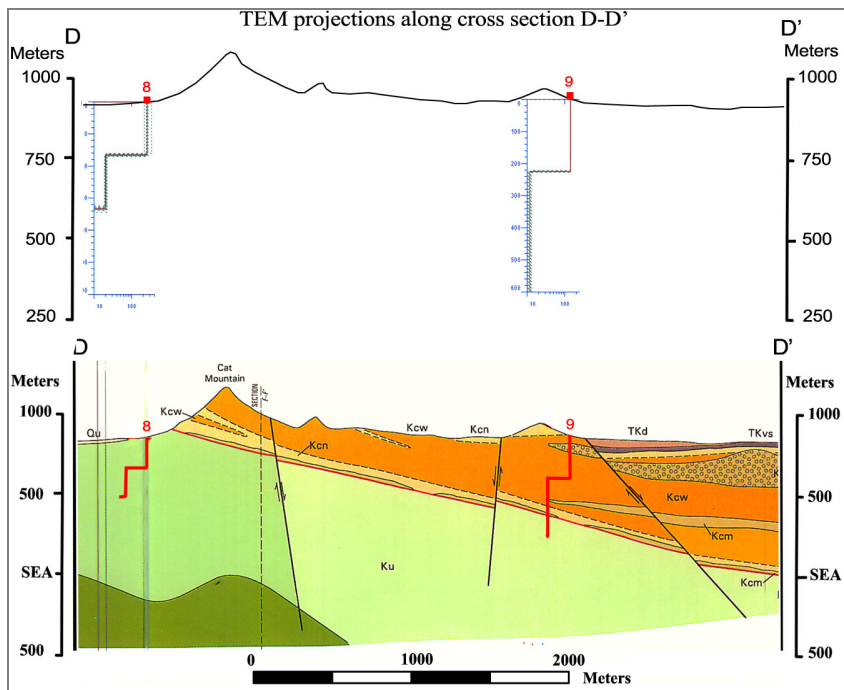


Figure 2.29. Comparison of TEM inversion model with D-D' interpreted geological cross section from Lipman, 1993.

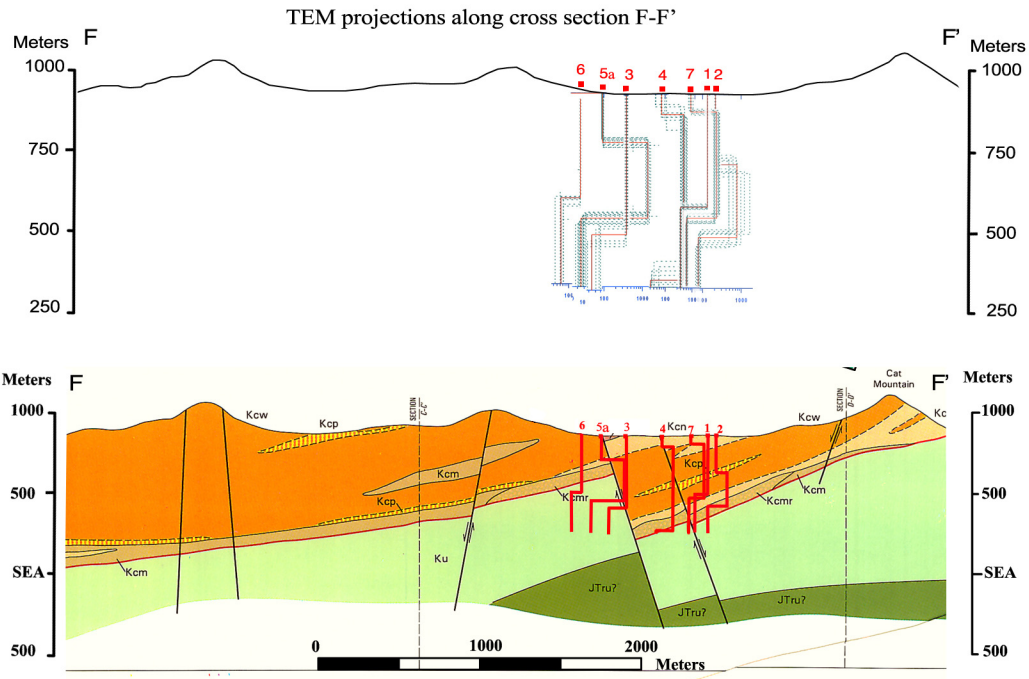


Figure 2.30. Comparison of TEM inversion model with F-F' interpreted geological cross section from Lipman, 1993.

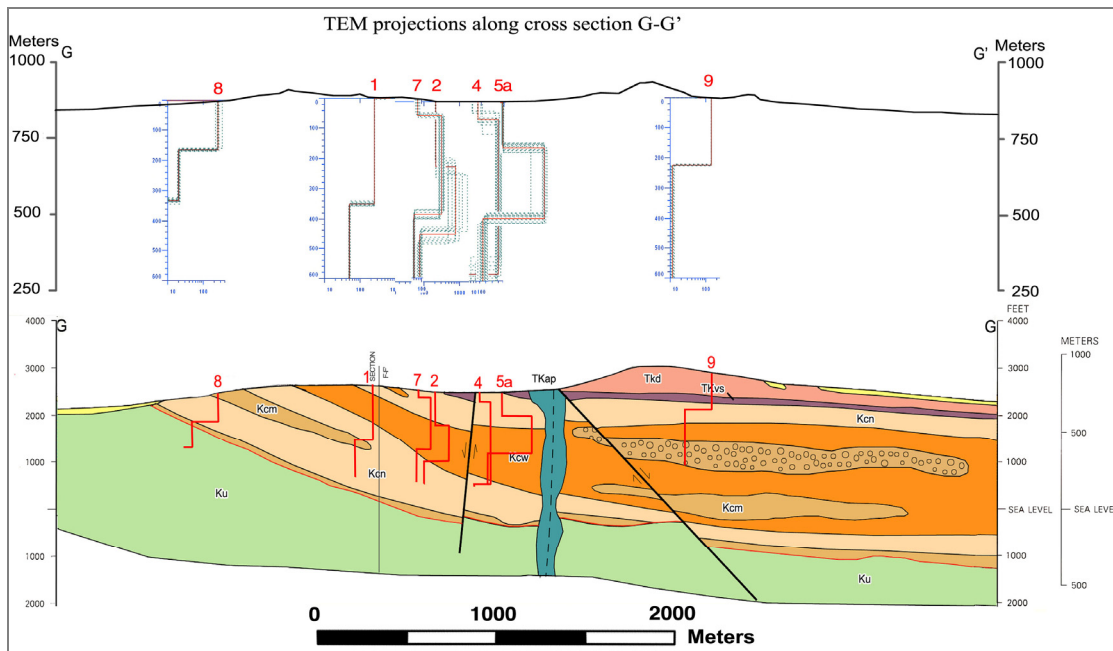


Figure 2.31. Comparison of TEM inversion model with G-G' interpreted geological cross section from this report.

The comparison of the TEM models with the geological cross-sections shows that the volcanic package, specially the densely welded units (Kcw) present in the Tucson Mountains area is similar in the TEM models and in the interpreted geologic cross sections. TEM site 10, projected in the cross section C-C', agrees with an interpreted normal fault, whereas the western block is in a lower position with respect to the eastern block. On the other hand, TEM sites 9 and 8 across section D-D' show a shallower conductive layer that is not affected by a change of lithology. However, along this cross-section, the TEM sites were projected from a longer distance. Along the cross-section F-F' (approximately north-south) several TEM sites were projected across an important normal fault that down-drops the southern block. The top of the conductive layer from TEM sites 3, 5a and 1, at the north side of the fault, is at a higher elevation in comparison with TEM sites 4 and 2 at the southern side of the fault. This case matches well the geological interpretation made by Lipman, 1993, and allows an inference of continuity of the conductive layer across the structures. The geological cross-section G-G' was interpreted for this report, based on the geological map and cross sections previously interpreted by Lipman, 1993. Lipman provided abundant strike and dip data and a good description of the stratigraphic sequence and relative movements of the main faults. The TEM sites 8, 1, 7, 2, 4 and 5a show a continuity of the conductive layer across the volcanic package (Kcw, Kcm and Kcn) following the stratigraphy, starting from shallower to a deeper elevation. However, TEM site 9 is located over a different geologic unit (Tkd, Tkvs), in a higher topographic location, and is showing that the top to the conductive layer is at a higher elevation in comparison with the TEM sites located southwest of this position. Site 9 is also the site that is close to the Tucson Water Reservoir and is likely affected by the large metal-lined reservoir facility. We therefore, have eliminated this site from further interpretation. Finally, TEM models, in comparison with the geological cross-

sections show that the densely welded units (Kcw) from the volcanic sequence in the Tucson Mountains are high resistive, and probably impermeable, whereas the non- to partially-welded volcanic units (Kcn) and the breccias, and the underlying sedimentary rocks can be more permeable, conductive and may form a good reservoir for water.

3. Controlled Source Audio Magnetotelluric (CSAMT) Survey

3.1 Introduction and Location

The Laboratory for Advanced Subsurface Imaging (LASI), in conjunction with Zonge International, Inc., acquired Controlled Source Audio-frequency Magnetotellurics (CSAMT) data along a 500-meter transect in the Tucson Mountains. The location of the survey transect is shown in Figures 3.1 and 3.2, below.

3.2 Methodology and Instrumentation

The CSAMT method involves transmitting a controlled signal at a suite of frequencies into the ground using either a grounded dipole or through a wire loop at one location, and measuring the received electric and magnetic fields in the exploration area of interest. The resistivity structure of the earth is calculated by taking the ratio of orthogonal horizontal electric and magnetic field magnitudes. For this work, scalar CSAMT data were acquired using 100-meter receiver dipoles for measurements of the electric fields (E_x), and a single orthogonal magnetic field measurement (H_y). The CSAMT method is used widely in the geothermal, groundwater, and mining fields and a description of the method, as used in these surveys, can be found at

http://www.zonge.com/PDF_Papers/Intro_CSAMT.pdf.

The signal source was a Zonge GGT-30 transmitter that was powered by a Zonge ZMG-30D motor generator. The GGT-30 is a current-controlled transmitter capable of 30 kW of power output. Transmitter control was accomplished through the use of a Zonge XMT-32 transmitter. Prior to transmission, the transmitter controller and receiver (GDP-32) time bases were synchronized. This synchronization provides an absolute phase reference for the survey.

The CSAMT transmitter was located along a line 125° West of true North, at a distance of 17 km from the center of the survey area. The transmitter dipole was oriented North-South and was 1 km long. The transmitter was located at the Avra Valley Geophysical Test Site, 11415 W. Ajo Way, T15S, R 11E, S22 (Sternberg et al., 1991).

3.3 Data Processing:

Zonge International processed the data to construct data plots of apparent resistivities, and to make pseudo sections and inversions of the results obtained from the field surveying. Raw files were preprocessed using the Zonge program Shred v4.07. This software converts the raw CSAMT data from GDP32-II ASCII format to a common ASCII format that other programs can effectively utilize. The CSAVGW program then converts the electric and magnetic field values into apparent resistivity and phase plots for each station along the survey line. It was then used to average the apparent resistivities for each station, so that a graphic representation of the data could be displayed. The AMTAVG program was used to create plots of phase, apparent resistivity, and E- and H-Magnitude, all versus frequency. These plots allowed the static shift effects to be clearly seen, which helped in creating more effective plots in CSAVGW. The ASTATIC program allowed for further deletion of points within the plots generated in CSAVGW, and also allowed for lines to be shifted up or down.

After the pseudo sections were created, inversions were carried out using SCSINV for successive 1D inversions along the profile. The exported files from SCSINV were imported into MODSECT, producing final contoured inverted pseudo sections for interpretation .

3.4 Interpretation

The CSAMT survey was conducted over a portion of the FF' cross section. The projection of the actual survey sites to the profile line FF' is shown in Figure 3.2. In Figures 3.3 and 3.4, the interpolated 2D CSAMT section shows that the apparent resistivity is high until about 500 m depth. At around 500m depth, the apparent resistivity, decreases by almost half to 25 ohm-meters. Time-Domain EM surveys conducted in the same area show a similar resistivity structure. The high-resistivity over lower resistivity values seen in the 2-D inversion are interpreted as resistive volcanic units that overlay more porous, sedimentary rock units.

CSAMT Stations

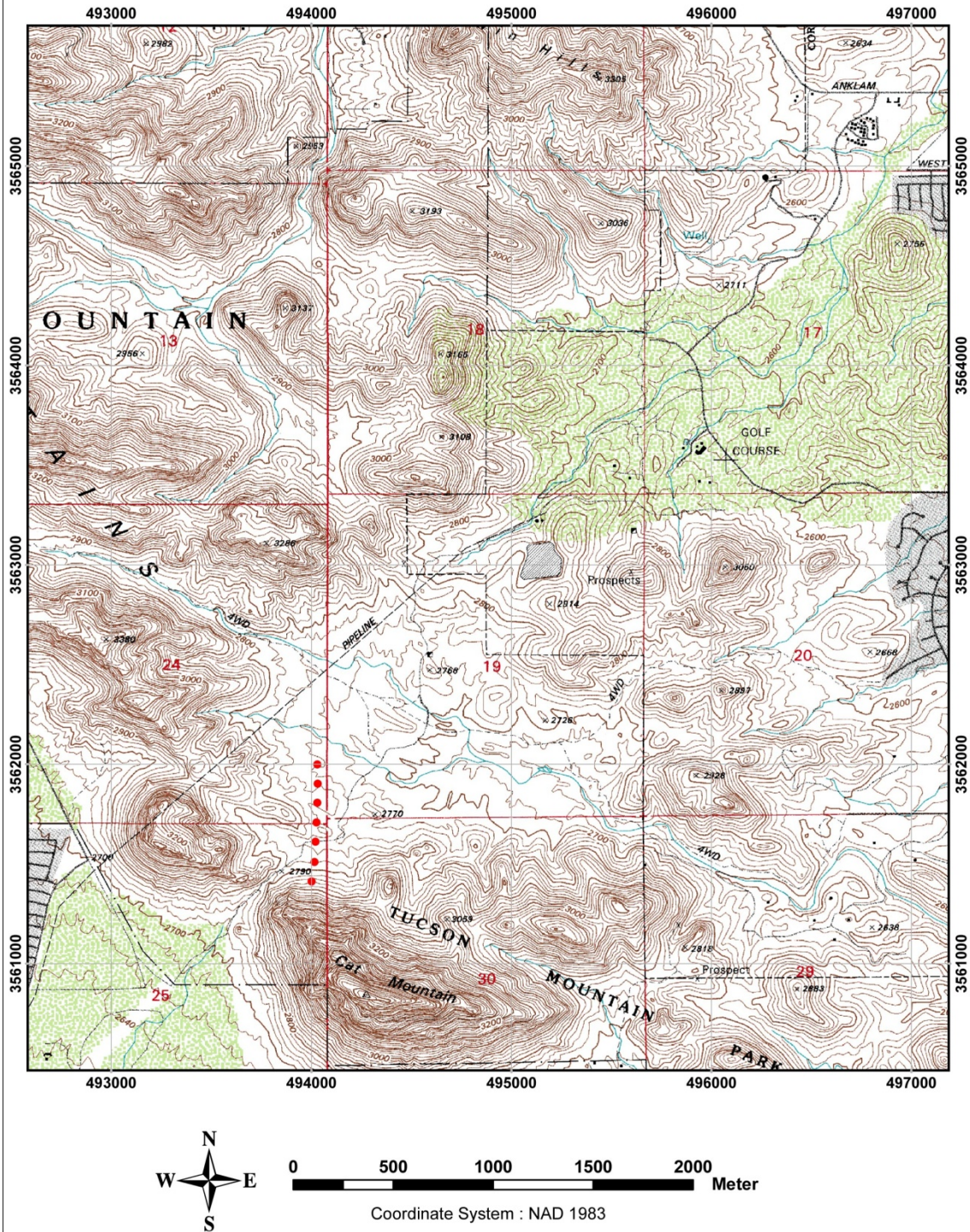


Figure 3.1. Location of CSAMT stations (red points) overlaid on top of the local topographic map of Tucson.

CSAMT stations

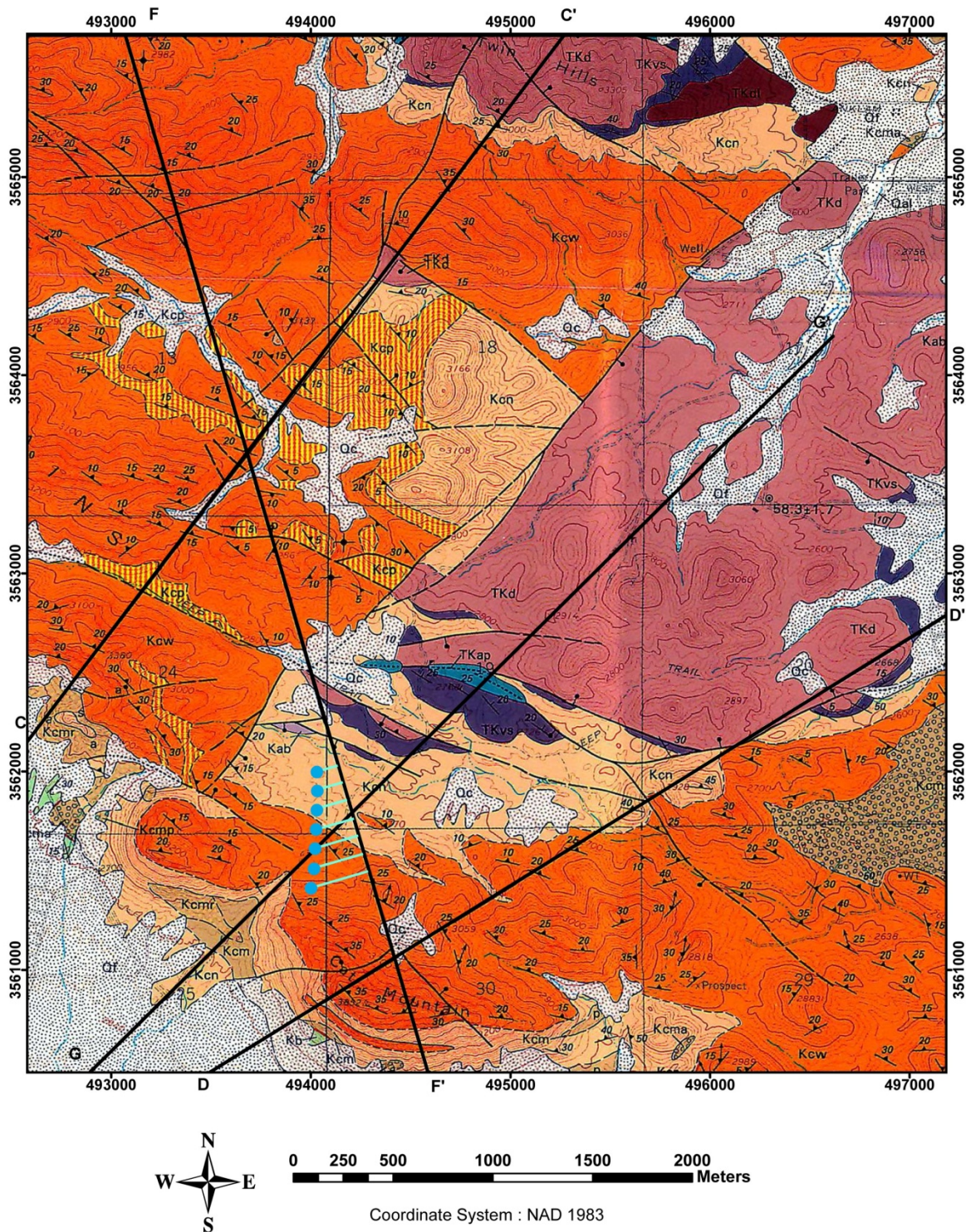


Figure 3.2. Blue dots showing the location of CSAMT station overlaid on top of geological map of Tucson mountain. Light blue lines shows the projection of CSAMT data onto the F-F' cross section.

CSAMT Cross Section

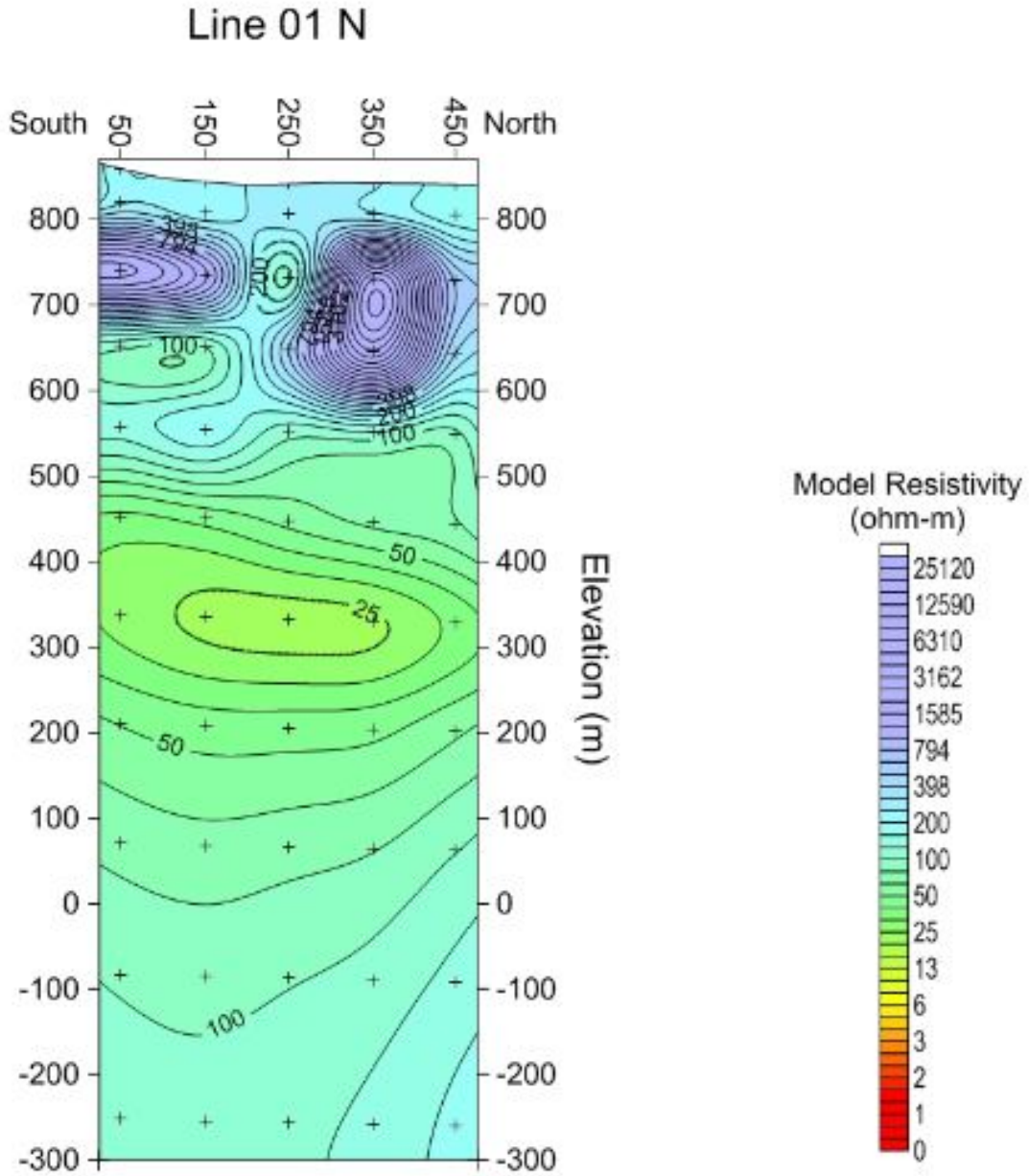


Figure 3.3 – CSAMT smooth-model inversion. Two dimensional pseudosection, using successive one-dimensional inversions.

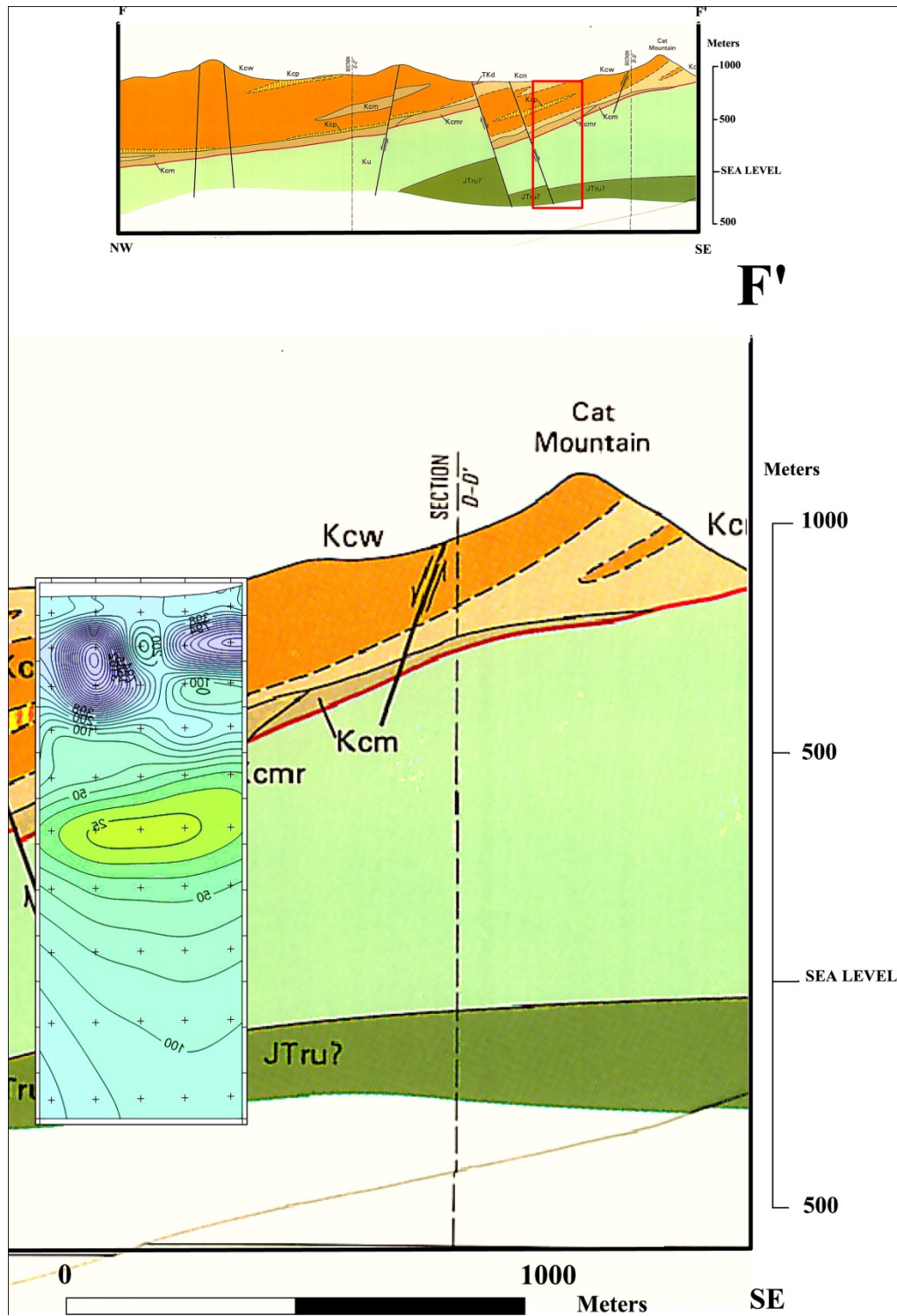


Figure 3.4 - CSAMT smooth-model inversion. Two dimensional pseudosection, using successive one-dimensional inversions. Resistivity cross section compared with geologic section along F-F' line.

4. Magnetic Survey

4.1 Introduction and Location

Total field magnetic data were collected on February 19 and March 5 of 2011. The location was the Tucson Mountains, with data collected along parts of the Yetman Trail, the Starr Pass Trail, the 36th Street Trail, and the Rock Wren Trail (Figure 4.1). A total of 196 points were measured along three survey paths. A magnetic base station was also set up on February 19th next to the Richard E. Genser Starr Pass Trailhead. The Tucson USGS magnetic base station (TUC Geomagnetic Observatory, Saguaro National Park, Arizona) was used to correct our magnetic measurements on both February 19th and March 5th. We obtained regional magnetic data from the USGS Publications Warehouse, from which magnetic strength over the Tucson Mountains survey area has been interpolated (Figure 4.2). The regional data provides a good overview of the magnetic variations in this area, and is in general agreement with our field data.

4.2 Instrumentation and Field Procedures

The magnetometers used for this survey were the GEM Systems GSM-19 Overhauser Magnetometer, the EDA OMNI IV Magnetometer, and the EDA OMNI Plus Magnetometer. The GPS units used for locating the sites were the Garmin Rino 520HCx, and the Garmin Rino 110. The first day of magnetic data gathering involved two separate groups. The first group surveyed a line of magnetic points separated by 50 meters measured with a surveying tape dragged along the trail. A total of 84 points were collected, following the Starr Pass trail, starting at the Richard E. Genser Starr Pass Trailhead and ending at the Cat Mountain Trailhead. A table showing the data collected is shown in Figure 4.3. The instrument used to collect this portion of the data was the GEM Systems GSM-19 Overhauser Magnetometer. A second magnetometer served as a base

station and stayed in one location just West of the Richard E. Genser Starr Pass Trailhead. Measurements were taken at 5 minute intervals, resulting in a total of 65 measurements. The instrument used to collect this portion of the data was the EDA OMNI Plus Magnetometer. The data from this base station magnetometer was compared with the Tucson Geomagnetic Observatory station located in Saguaro National Park. This comparison is shown in Figure 4.5.

The second day of magnetic data collection also involved two separate groups. The first group surveyed a line of magnetic points separated by 50 meters measured by distance to the last point as determined by GPS receivers. A total of 74 points were collected, following the Yetmen Trail starting 50 meters past the last phone line pole at the Camino De Oeste Trailhead, and breaking off at the Rock Wren Trail fork which was followed until it came within 50 meters of the water reservoir. The instrument used to collect this portion of the data was the GEM Systems GSM-19 Overhauser Magnetometer. The second group also surveyed a line of magnetic points separated by 50 meters as measured by distance to the last point as determined by the GPS receivers. A total of 38 points were collected, following the 36th Street Trail, starting at the 36th Street Trailhead and ending at the junction with the Starr Pass Trail. The instrument used to collect this portion of the data was an EDA OMNI IV Magnetometer. Both sets of data from the second day were corrected for geomagnetic field drift using the Tucson Geomagnetic Observatory base station. The data for both groups on this day are shown in Figure 4.4.



Figure 4.1. A trail map covering the area which was used to collect magnetic data, for both February 19, 2011 and March 5, 2011.

Regional Magnetic Intensity Map

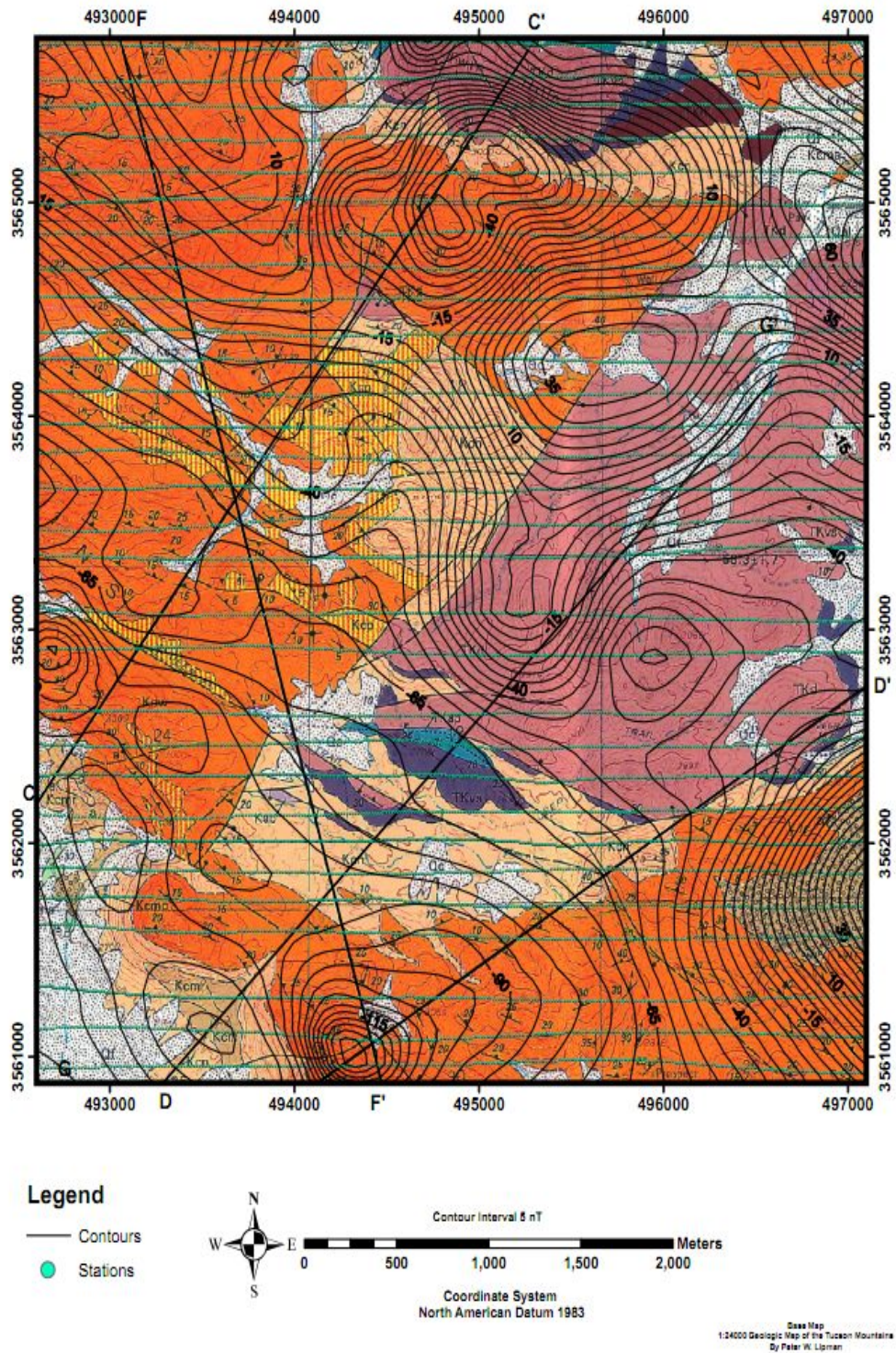


Figure 4.2. A geologic map of the study area overlain with interpolated contours of magnetic strength. Contours are at intervals of 5 nT. Original data are from the USGS Publications Warehouse. Data were gathered along flight lines, 150 meters above ground at 150 meter spacing.

#	Time	Easting	Northing	nT
1	10:39	495585	3563127	47714.000
2	10:33	495555	3563087	47689.000
3	10:28	495519	3563058	47656.000
4	10:25	495492	3563012	47633.000
5	10:48	495478	3562965	47633.000
6	10:54	495474	3562921	47754.000
7	10:57	495499	3562875	47725.000
8	10:59	495531	3562835	47750.000
9	11:03	495556	3562796	47664.000
10	11:04	495585	3562759	47676.000
11	11:05	495632	3562735	47643.000
12	11:08	495674	3562710	47651.000
13	11:12	495699	3562671	47552.000
14	11:16	495746	3562651	47513.000
15	11:18	495782	3562620	47533.000
16	11:20	495810	3562581	47527.000
17	11:22	495821	3562537	47598.000
18	11:25	495772	3562518	47619.000
19	11:27	495731	3562489	47509.000
20	11:30	495685	3562482	47548.000
21	11:35	495641	3562456	47557.000
22	11:37	495600	3562434	47631.000
23	11:39	495569	3562398	47816.000
24	11:41	495546	3562357	47657.000
25	11:44	495522	3562314	47709.000
26	11:46	495492	3562273	47634.000
27	11:47	495481	3562229	47615.000
29	11:49	495448	3562188	47602.000
30	11:51	495410	3562158	47599.000
31	11:54	495368	3562141	47582.000
32	11:55	495323	3562118	47584.000
33	11:57	495275	3562122	47585.000
34	12:03	495225	3562116	47610.000
35	12:15	495177	3562110	47631.000
36	12:20	495129	3562097	47616.000
37	12:21	495076	3562107	47611.000
38	12:23	495037	3562140	47605.000
39	12:25	494988	3562150	47605.000
40	12:27	494940	3562155	47603.000
41	12:30	494892	3562166	47596.000
42	12:32	494844	3562169	47597.000
43	12:36	494799	3562173	47606.000
44	12:40	494752	3562162	47606.000

#	Time	Easting	Northing	nT
45	12:42	494696	3562156	47599.000
46	12:44	494651	3562172	47600.000
47	12:46	494606	3562192	47598.000
48	12:48	494568	3562160	47613.000
49	12:50	494541	3562122	47612.000
50	12:52	494501	3562096	47608.000
51	12:54	494453	3562086	47609.000
52	12:56	494402	3562082	47610.000
53	12:59	494364	3562050	47606.000
54	13:01	494343	3562013	47608.000
55	13:03	494306	3561975	47607.000
56	13:05	494267	3561949	47594.000
57	13:10	494226	3561920	47612.000
58	13:13	494199	3561876	47627.000
59	13:15	494181	3561827	47621.000
60	13:16	494177	3561778	47615.000
61	13:18	494157	3561735	47609.000
62	13:20	494131	3561693	47605.000
63	13:23	494131	3561649	47572.000
64	13:25	494087	3561635	47562.000
65	13:27	494044	3561623	47558.000
66	13:30	493995	3561618	47562.000
67	13:32	493957	3561600	47483.000
68	13:33	493945	3561550	47520.000
69	13:35	493905	3561523	47580.000
70	13:37	493858	3561481	47591.000
71	13:39	493815	3561457	47598.000
72	13:41	493783	3561428	47597.000
73	13:44	493746	3561393	47596.000
74	13:46	493715	3561352	47599.000
75	13:48	493671	3561315	47602.000
76	13:50	493633	3561278	47597.000
77	13:52	493608	3561236	47590.000
78	13:55	493582	3561186	47586.000
79	13:56	493561	3561138	47583.000
80	13:58	493516	3561119	47587.000
81	14:00	493477	3561089	47625.000
82	14:03	493445	3561052	47620.000
83	14:05	493399	3561029	47611.000
84	14:07	493367	3560991	47632.000
85	14:08	493343	3560953	47618.000

Figure 4.3. A table showing the magnetic data measured on February 19, 2011, collected along the Starr Pass Trail. Columns include point #, time data was measured, UTM Easting and Northing, and nT at the location.

#	Time	Easting	Northing	nL
1	10:14:00 AM	494091	3565267	47772
2	10:17:00 AM	494100	3565215	47827
3	10:20:00 AM	494107	3565165	47848
4	10:26:00 AM	494093	3565117	47882
5	10:30:00 AM	494070	3565074	47907
6	10:33:00 AM	494044	3565039	47980
7	10:35:00 AM	494008	3564995	47783
8	10:38:00 AM	493993	3564948	47746
9	10:43:00 AM	493973	3564902	47756
10	10:46:00 AM	493973	3564852	47840
11	10:54:00 AM	493966	3564803	47830
12	10:57:00 AM	493970	3564755	47831
13	11:00:00 AM	493972	3564704	47807
14	11:03:00 AM	493938	3564666	47788
15	11:05:00 AM	493904	3564630	47766
16	11:10:00 AM	493876	3564587	47750
17	11:12:00 AM	493829	3564564	47757
18	11:14:00 AM	493792	3564529	47753
19	11:17:00 AM	493750	3564505	47770
20	11:19:00 AM	493706	3564479	47759
21	11:22:00 AM	493665	3564449	47776
22	11:24:00 AM	493626	3564417	47763
23	11:27:00 AM	493586	3564386	47738
24	11:30:00 AM	493540	3564364	47768
25	11:32:00 AM	493506	3564328	47818
26	11:34:00 AM	493494	3564278	47797
27	11:48:00 AM	493481	3564229	47728
28	11:50:00 AM	493466	3564182	47727
29	11:54:00 AM	493482	3564134	47706
30	11:59:00 AM	493524	3564107	47693
31	12:01:00 PM	493564	3564075	47722
32	12:04:00 PM	493608	3564050	47718
33	12:06:00 PM	493645	3564013	47773
34	12:08:00 PM	493663	3563967	47741
35	12:09:00 PM	493710	3563945	47725
36	12:12:00 PM	493755	3563924	47717
37	12:13:00 PM	493785	3563884	47684
38	12:16:00 PM	493829	3563801	47693
39	12:18:00 PM	493879	3563859	47684
40	12:20:00 PM	493878	3563808	47555
41	12:22:00 PM	493913	3563771	47656
42	12:24:00 PM	493931	3563724	47661
43	12:26:00 PM	493943	3563674	47646
44	12:27:00 PM	493976	3563635	47666
45	12:29:00 PM	494011	3563599	47692
46	12:33:00 PM	494034	3563554	47671
47	12:35:00 PM	494061	3563511	47678
48	12:36:00 PM	494096	3563477	47694
49	12:38:00 PM	494116	3563431	47689
50	12:41:00 PM	494142	3563386	47714
51	12:44:00 PM	494185	3563357	47686
52	12:46:00 PM	494231	3563335	47653
53	12:50:00 PM	494281	3563326	47687
54	12:52:00 PM	494328	3563308	47687
55	12:54:00 PM	494359	3563267	47716
56	12:57:00 PM	494381	3563222	47660
57	12:59:00 PM	494406	3563177	47663
58	01:00:00 PM	494411	3563126	47588
59	01:03:00 PM	494397	3563079	47579
60	01:05:00 PM	494419	3563034	47588
61	01:07:00 PM	494459	3562995	47618
62	01:09:00 PM	494470	3562947	47662
63	01:11:00 PM	494512	3562920	47608
64	01:16:00 PM	494553	3562889	47612
65	01:18:00 PM	494582	3562849	47695
66	01:20:00 PM	494631	3562865	47235
67	01:23:00 PM	494681	3562879	47641
68	01:27:00 PM	494724	3562905	47650
69	01:29:00 PM	494776	3562898	47898
70	01:31:00 PM	494823	3562884	47749
71	01:33:00 PM	494871	3562871	47719
72	01:37:00 PM	494918	3562891	47720
73	01:42:00 PM	494965	3562907	47911
74	01:44:00 PM	494996	3562867	47788

#	Time	Easting	Northing	nL
1	10:39	47719.1	3561707	47719.1
2	10:42	47766.6	3561676	47766.6
3	10:45	47781.7	3561620	47781.7
4	10:48	47783.1	3561565	47783.1
5	10:51	47770.5	3561517	47770.5
6	10:55	47746.5	3561474	47746.5
7	10:58	47720.2	3561430	47720.2
8	11:01	47694.5	3561396	47694.5
9	11:04	47699	3561389	47699
10	11:08	47686.2	3561418	47686.2
11	11:11	47690.4	3561444	47690.4
12	11:14	47693.1	3561464	47693.1
13	11:17	47645.2	3561462	47645.2
14	11:19	47615	3561489	47615
15	11:25	47634.5	3561496	47634.5
16	11:27	47649.4	3561495	47649.4
17	11:30	47633.1	3561496	47633.1
18	11:32	47639.4	3561514	47639.4
19	11:35	47644.1	3561541	47644.1
20	11:37	47651.3	3561558	47651.3
21	11:40	47642.1	3561595	47642.1
22	11:42	47663.4	3561610	47663.4
23	11:47	47654.2	3561650	47654.2
24	11:49	47658.4	3561682	47658.4
25	11:56	47656.9	3561682	47656.9
26	11:59	47613.7	3561700	47613.7
27	12:03	47620.6	3561679	47620.6
28	12:04	47632.4	3561672	47632.4
29	12:08	47630.8	3561675	47630.8
30	12:10	47623.9	3561702	47623.9
31	12:14	47621.6	3561752	47621.6
32	12:15	47623	3561827	47623
33	12:20	47607.9	3561869	47607.9
34	12:22	47615	3561913	47615
35	12:26	47618.3	3561974	47618.3
36	12:28	47617.4	3562006	47617.4
37	12:31	47601.6	3562056	47601.6
38	12:35	47592.6	3562102	47592.6

Figure 4.4. Magnetic points gathered on March 5. The left table corresponds to the Yetman Trail data, and the right table corresponds to the 36th Street Trail data.

4.3 Data Processing and Interpretation

The first step taken in data processing was to compare our base station readings from February 19th against the USGS base station. This information tells us if a local base station is necessary, or if the variation in the Eastern Tucson Basin is similar to the variation in the Tucson Mountains, and therefore no local base station is necessary. As seen in Figure 4.5, there was a remarkable similarity between the two base stations. This led us to conclude that no local base station is needed and that the USGS base station in the Saguaro National Park is sufficient to correct for variation in measurements taken in the Tucson Mountains.

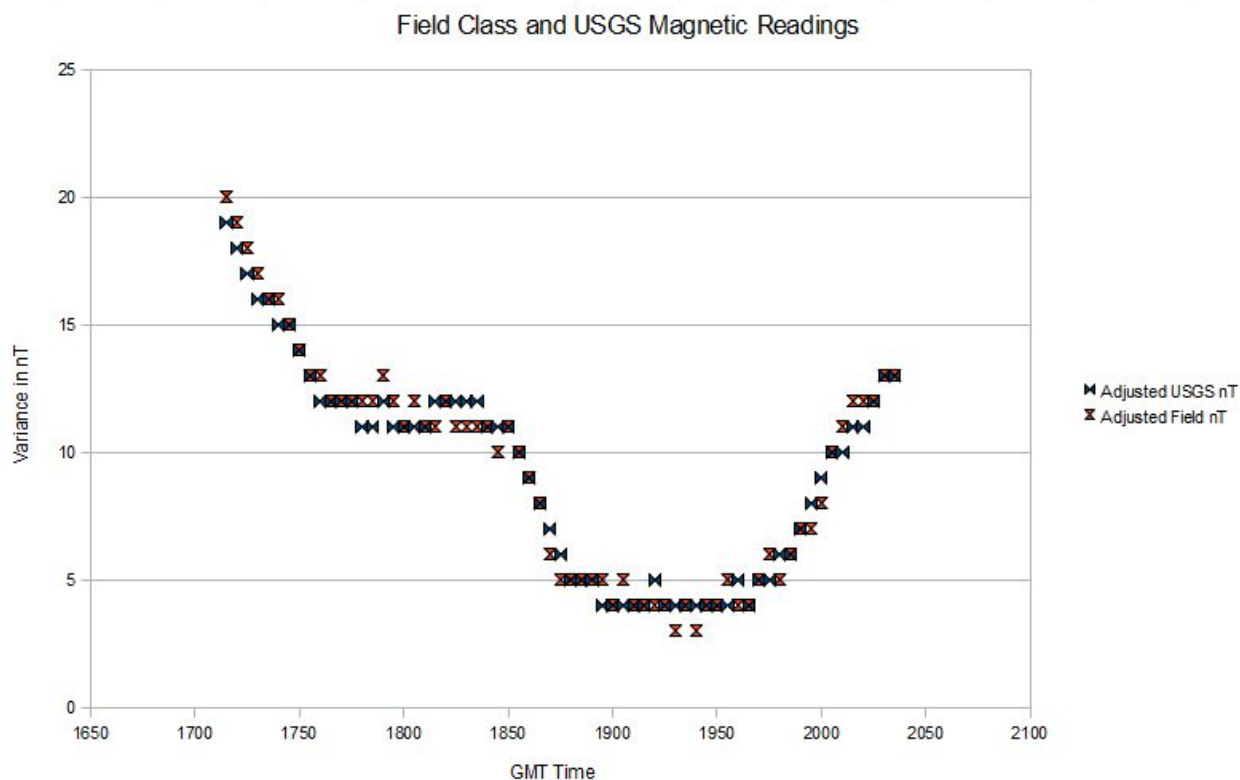


Figure 4.5. This graph shows the total field magnetic drift measured by the field team magnetometer and by the USGS Tucson Geomagnetic Observatory station (marked in red). Both data sets have been rounded to the nearest nT for all measurements, and both data sets have been adjusted to share an arbitrary starting nT value in order to remove a static difference of 170 nT between the two sites.

The second step of data processing was to run a correction for the data we collected using the USGS base station. This removes the temporal variation in the magnetic field throughout the days we gathered data. In order to do this, we correlated the time of measurement for each of our data points with the nearest time in the USGS base station data. Next, we took the selected set of USGS base station measurements and averaged them, then subtracted each USGS base station measurement from the average. This number was then added to our measurements from the field for each point, removing the temporal variation in our data throughout the period of collection.

The third step was to plot all the data over the Tucson Mountains using the X,Y UTM coordinates recorded by our GPS units. The resulting data are shown in Figure 4.6, which is overlain upon a topographic map. Next we plotted the location of four cross sections, CC', DD', FF', and GG', from Lipman (Lipman, 1993). Magnetic station locations were then projected orthogonally onto each cross section. The criteria used to determine which points to include in each projection were:

- 1) Distance of measurement from cross section.
- 2) Whether projection would cross different geologic structures.
- 3) Whether the projection would cross any major faults.

The selected projections are shown in Figure 4.7 (CC'), Figure 4.8 (DD'), Figure 4.9 (FF'), and Figure 4.10 (GG'). The volcanic layers were largely of similar composition and crossing them did not play a large role in influencing our decisions (so long as deep sedimentary layer boundaries were not crossed). Whether or not projected points crossed large faults was heavily weighted, and resulted in high data omission on the Eastern edge of the GG' and DD' cross sections.

To finish our projections, we graphed the projected data along the X-Z axis with each cross section. The results are shown in Figure 4.11 (CC'), Figure 4.12 (DD'), Figure 4.13 (FF'), and Figure 4.14 (GG').

Magnetic Stations

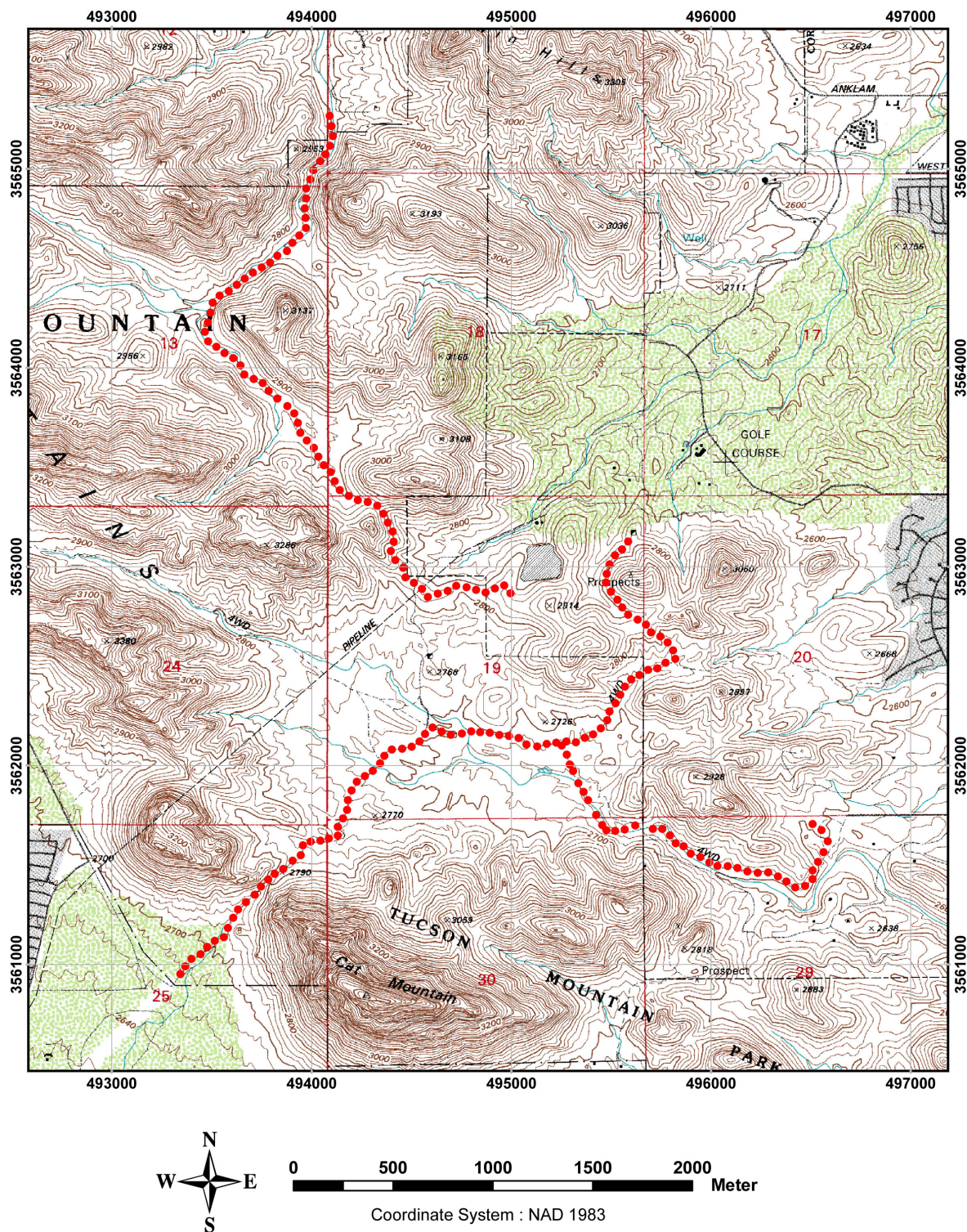


Figure 4.6. Topographic contour map of study area with all magnetic data points marked as red dots.

Magnetic Stations

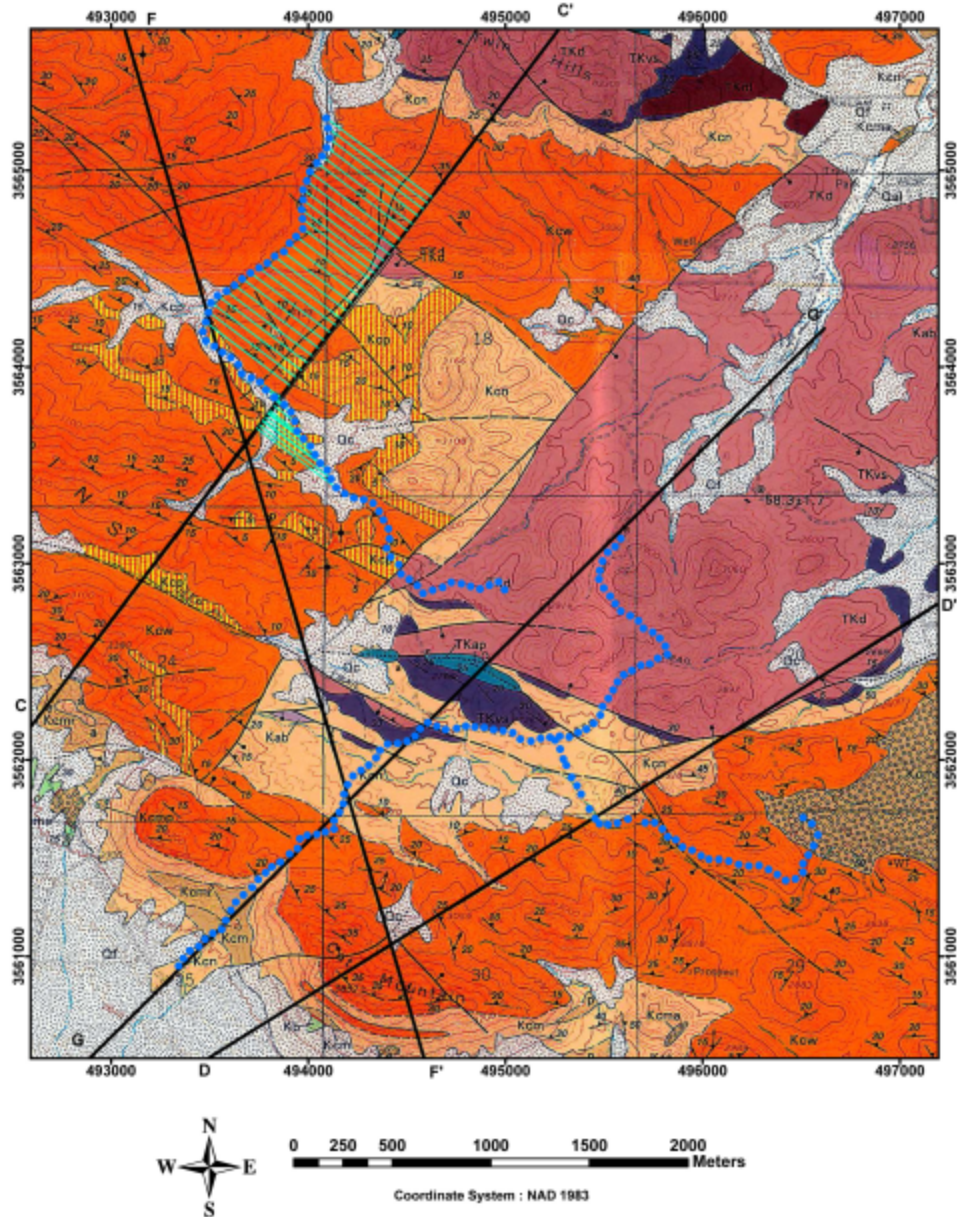


Figure 4.7. A map showing which magnetic points were projected onto the CC' cross section line. Blue dots represent locations of magnetic total field strength measurements. Projection lines are shown in green. Lipman cross sections are marked by black lines.

Magnetic Stations

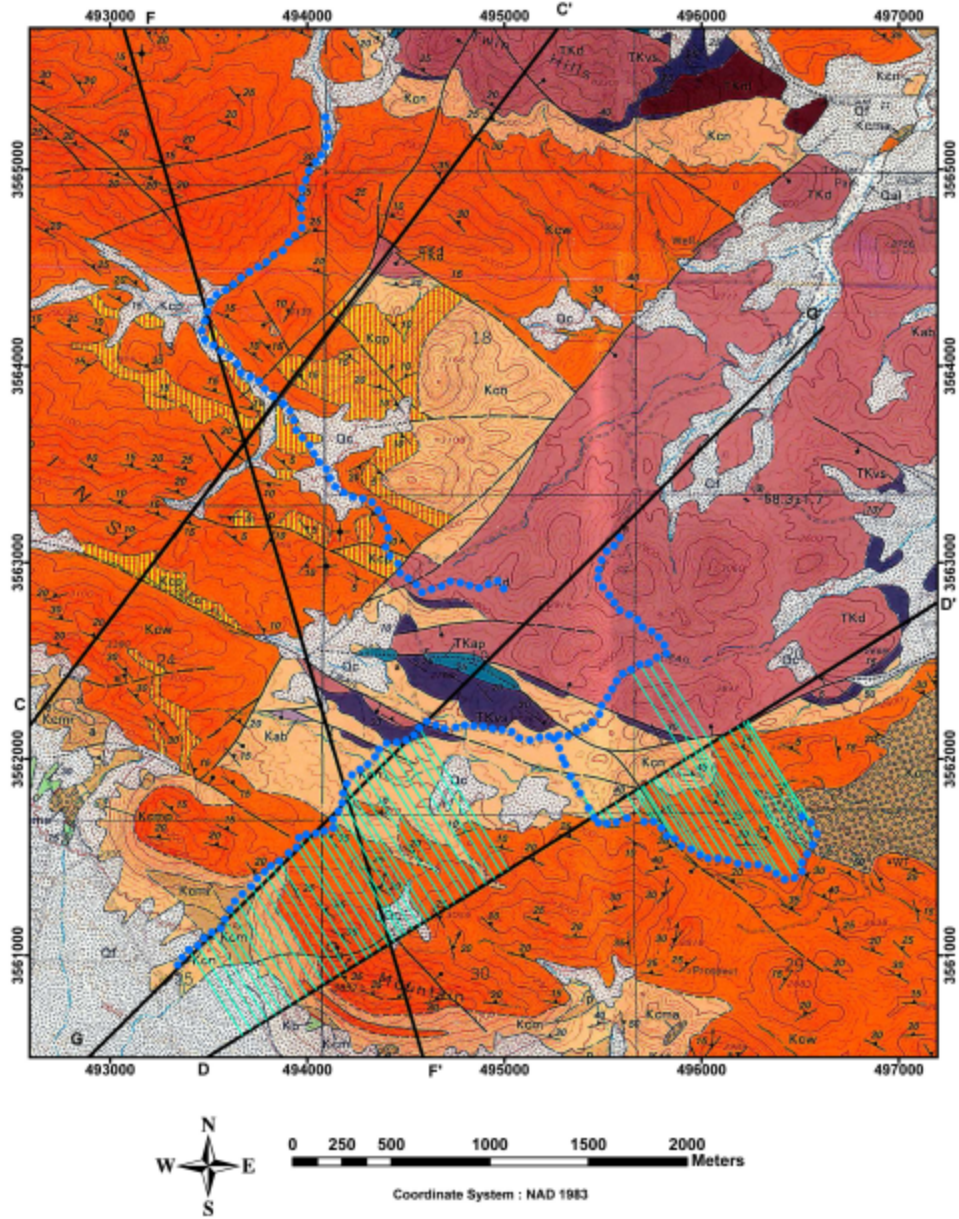


Figure 4.8. A map showing which magnetic points were projected onto the DD' cross section line.

Magnetic Stations

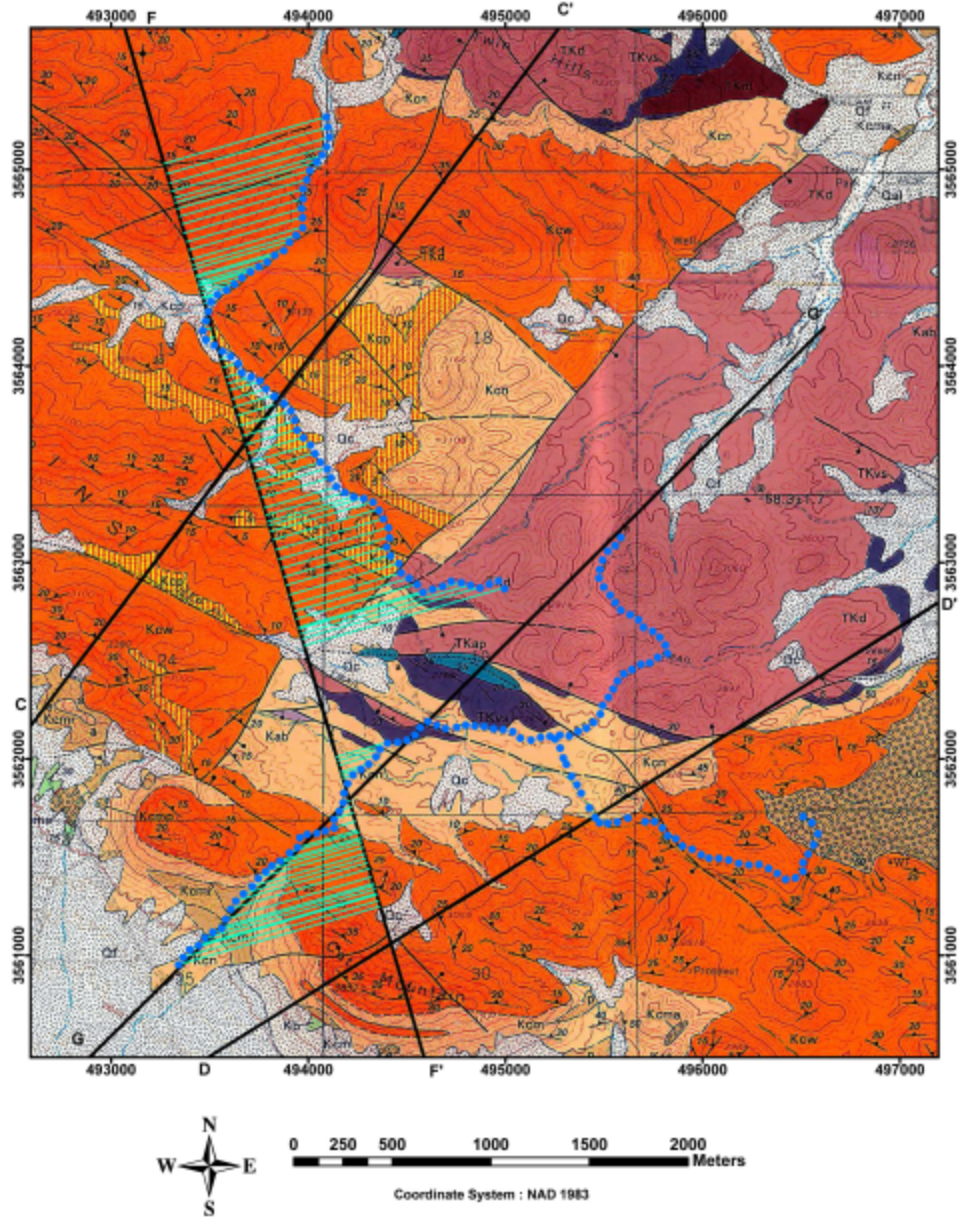


Figure 4.9. A map showing which magnetic points were projected onto the FF' cross section line.

Magnetic Stations

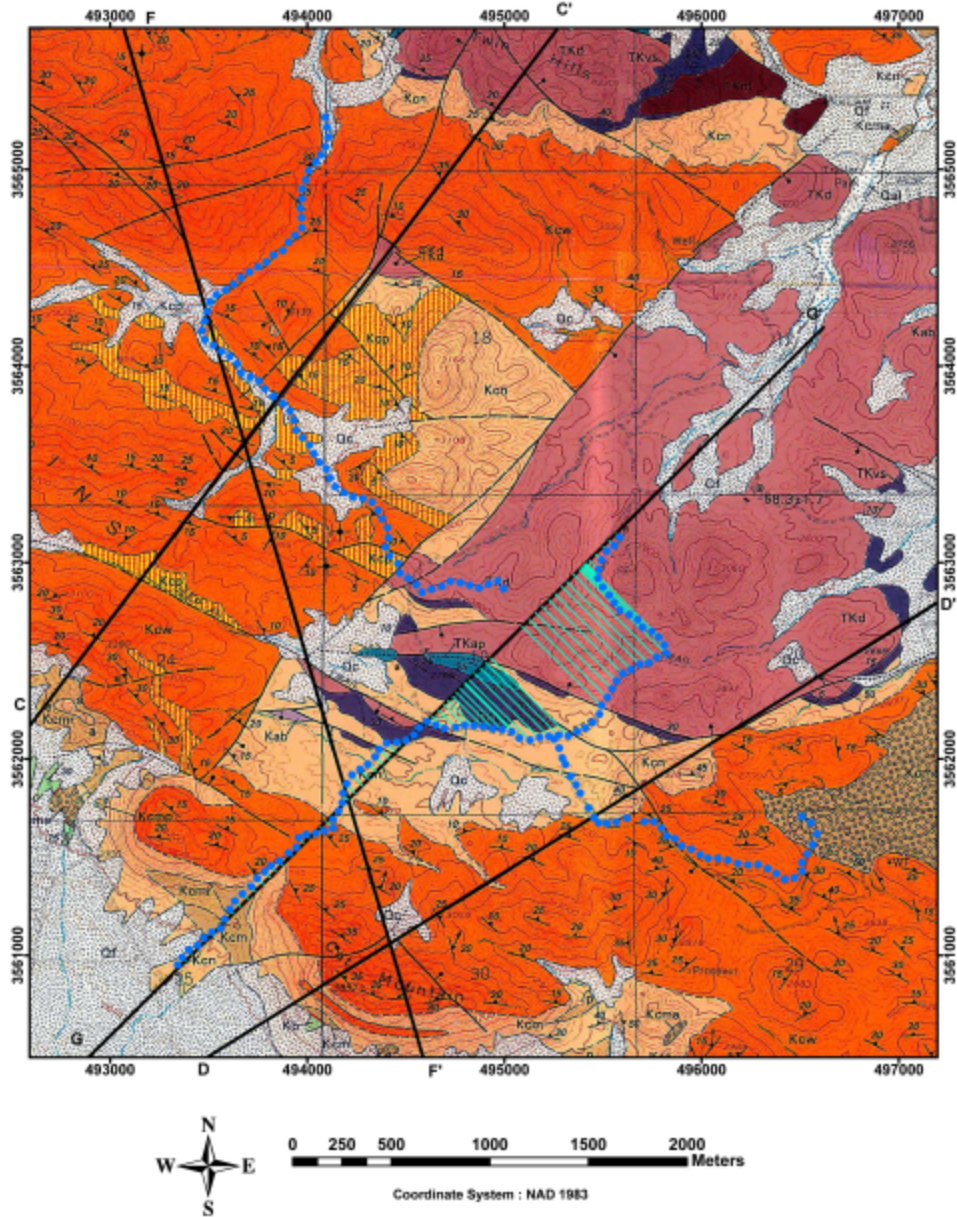


Figure 4.10. A map showing which magnetic points were projected onto the GG' cross section line.

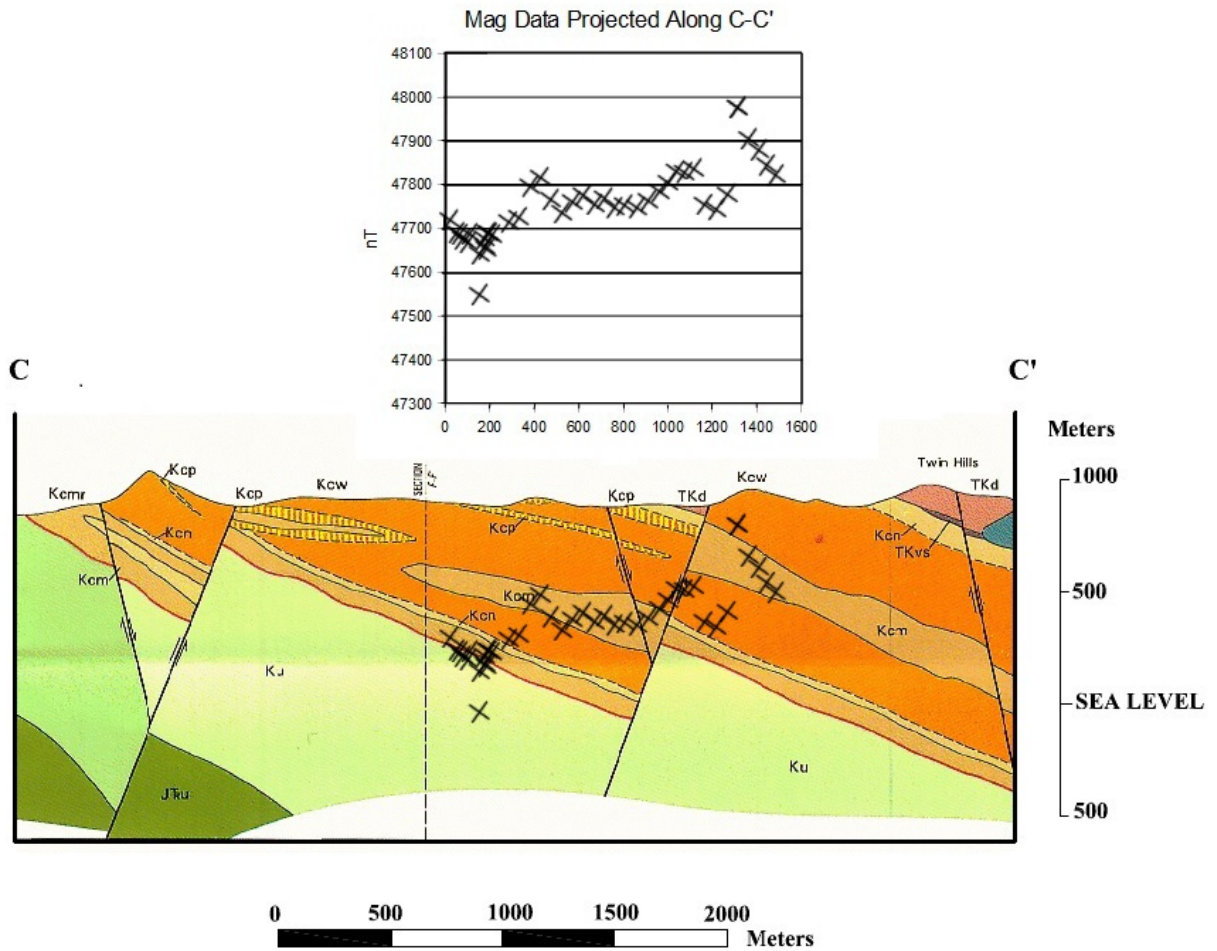


Figure 4.11. A graph of our drift corrected magnetic measurements projected onto the CC' line. The top graph shows the quantitative magnetic data, while the bottom graph overlaying the geology facilitates the correlation of the magnetic data with structures/faults. Geologic units are hypothesized by Lipman, 1993.

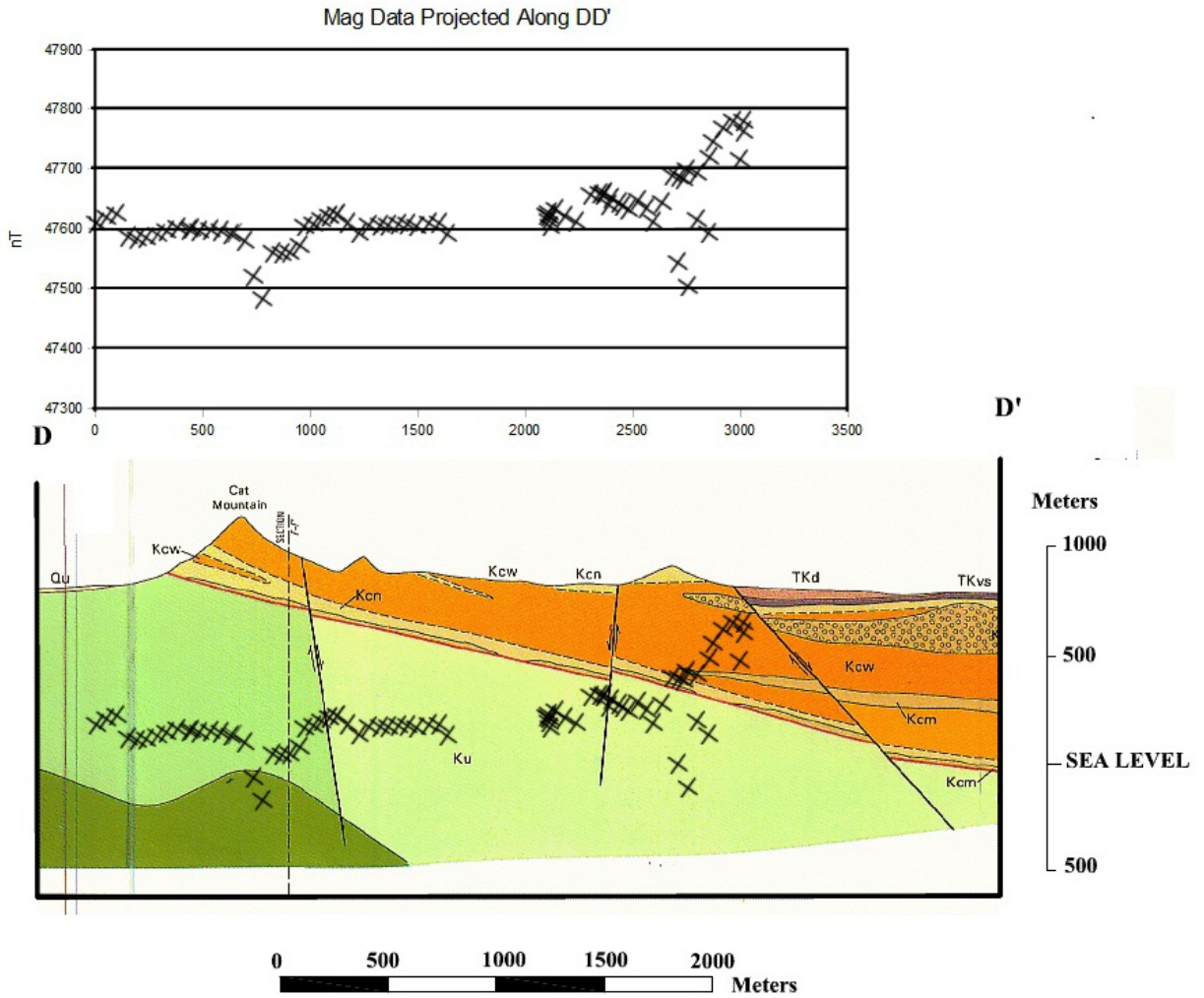


Figure 4.12. A graph of our drift corrected magnetic measurements at their location projected onto the DD' line.

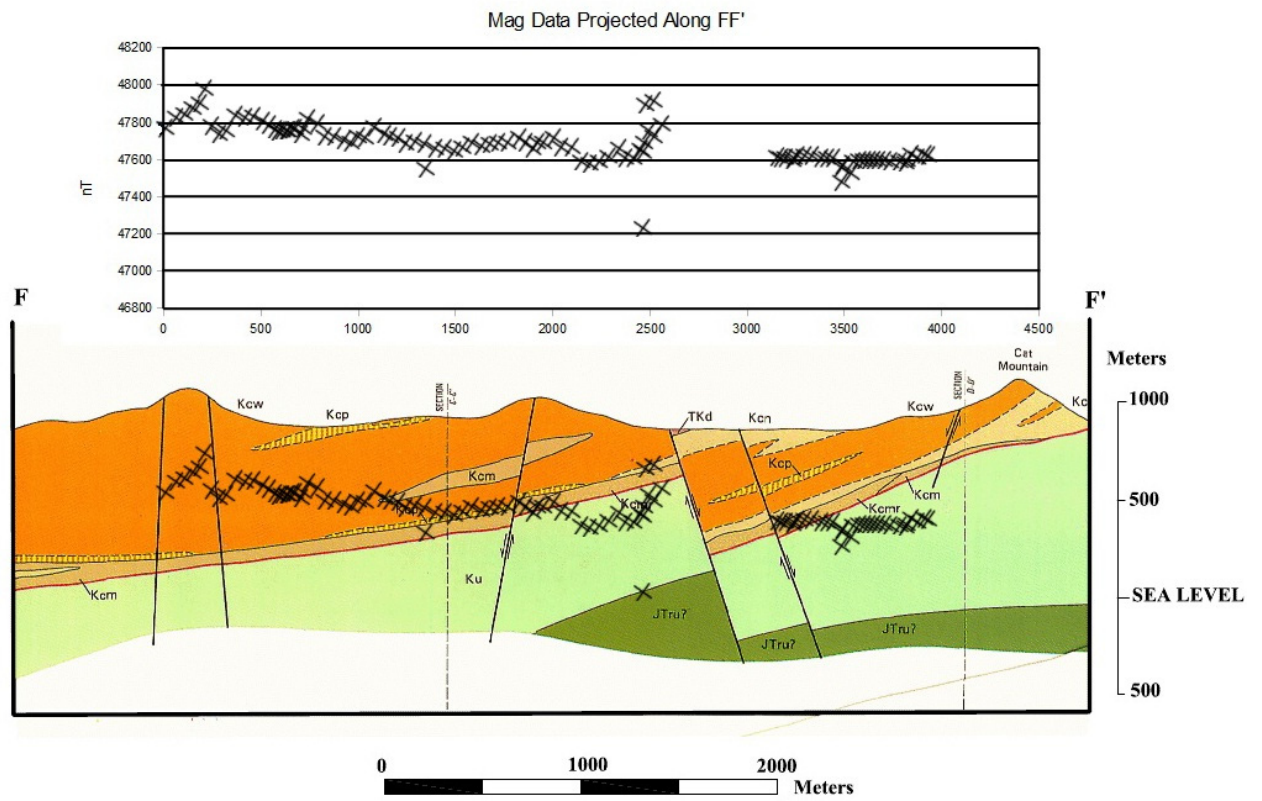


Figure 4.13. A graph of drift our corrected magnetic measurements at their location projected onto the FF' line.

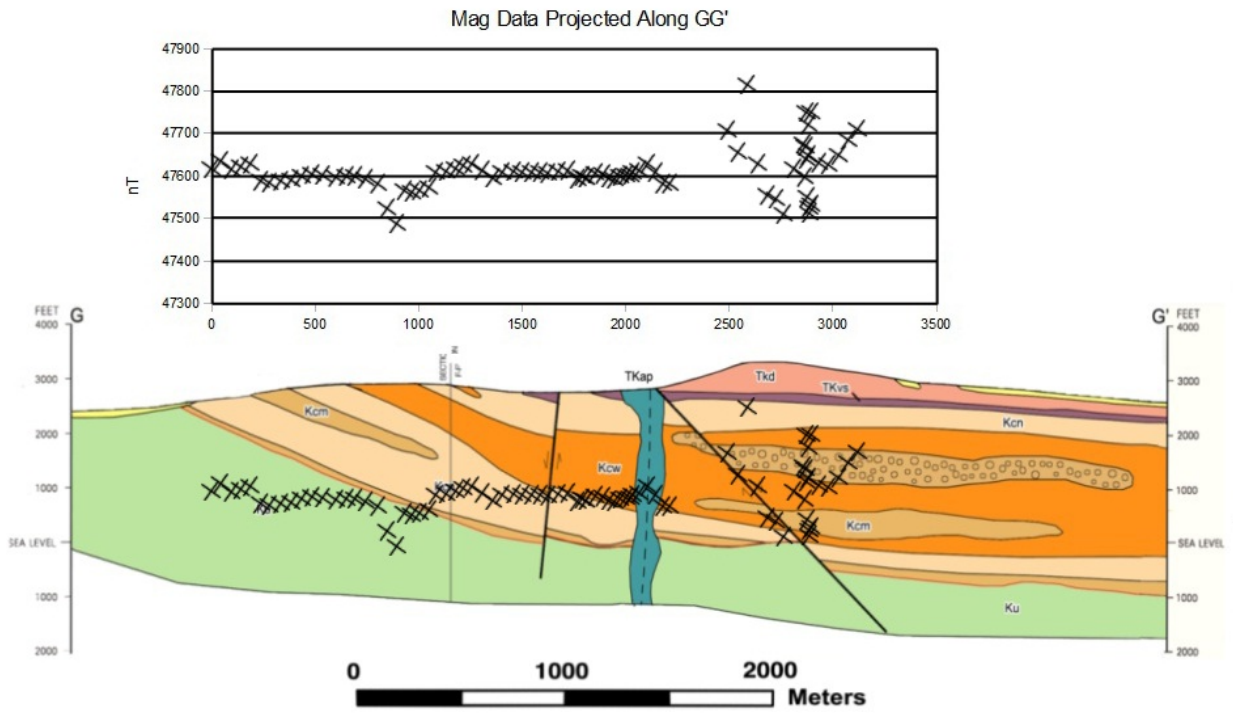


Figure 4.14. A graph of our drift corrected magnetic measurements at their location projected onto the GG' line. Multiple large faults near the right half of the GG' cross section are a likely cause for the data variability there.

4.4 Modeling and Inversion

Modeling was carried out using the IX2D modeling program from Interpex. A total of three geologic profiles on the FF' cross section were created, each one was modeled using forward calculations. All three profiles include three layers of varying magnetic susceptibility. The top blue layer represents colluvium with low magnetic susceptibility of 10 microcgs (negligible). The middle orange layer represents volcanics and was given a magnetic susceptibility of 1000 microcgs. The bottom blue layer represents sediments and was given a magnetic susceptibility of 1 microcgs (negligible). A weak top layer was created in order to remove the impact of topography which were not traversed in our data collection. This worked by modeling the weak magnetics directly below our measurements, which were taken in or close to wash settings between hills. This top layer extends several meters below the elevation of our lowest point.

The first profile only modeled a simple volcanics layer as hypothesized by Lipman, 1993, with a single major fault modeled. Expected total magnetic strength was calculated and is shown in Figure 4.15. This calculation shows the expected effect of this single fault in the volcanics.

The second profile shown in Figure 4.16 increased the size of the major fault, and kept all other parameters the same. This calculation shows the expected impact the size of this major fault would have on magnetic strength. As seen in the differences between Figure 4.15 and 4.16, there is only a minor change in the modeled magnetic strength.

The final profile shown in Figure 4.17 added a series of faults in the volcanics in order to see what a hypothetical volcanic subsurface may result in. The hypothetical faults did result in a

model that correlated with the measured magnetic strengths from the field. It should be noted that this hypothetical model does not look at how variance in magnetic susceptibility within the volcanics could play a role.

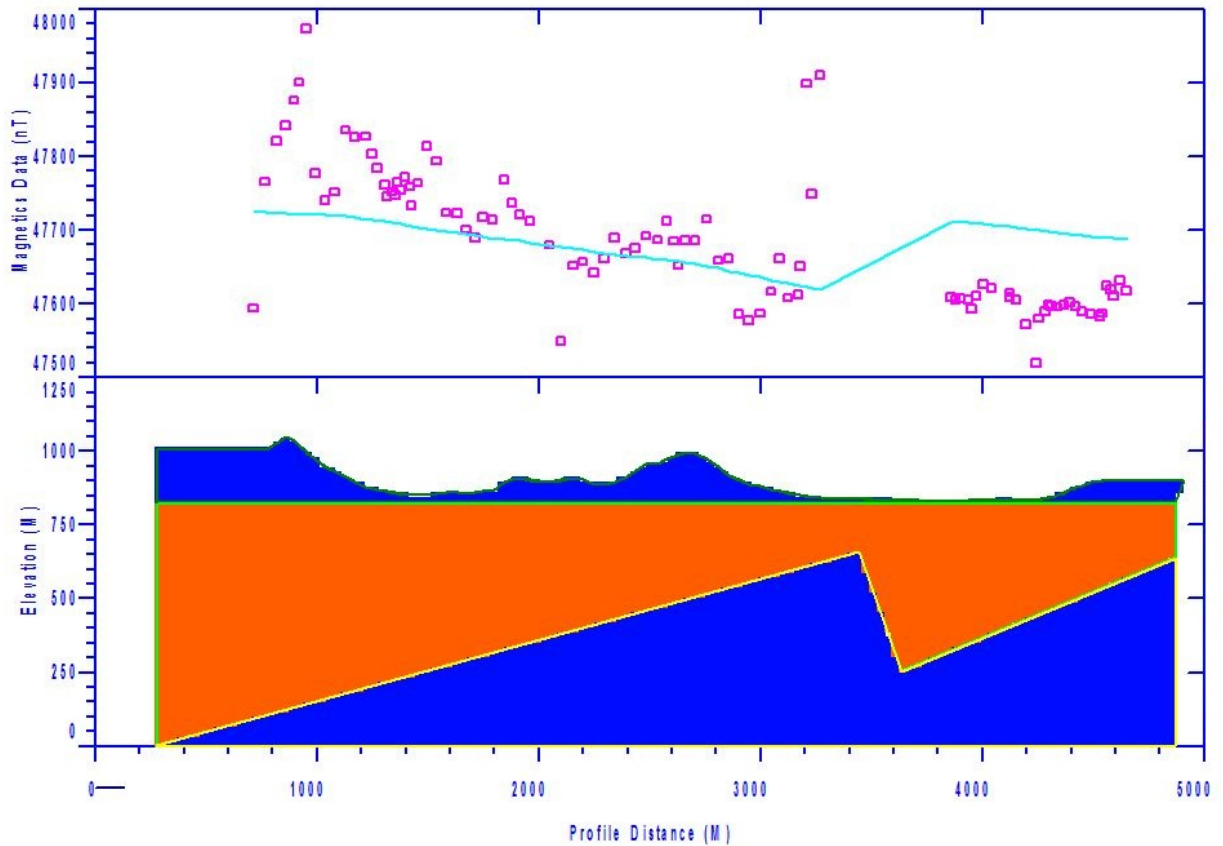


Figure 4.15. Simple geologic model with two rock layers shown on the bottom half of the figure. The top blue layer represents colluvium of negligible susceptibility. The middle orange layer represents volcanics of moderately high susceptibility. The bottom blue layer represents sediments of negligible susceptibility. The purple points represent actual measured magnetic strengths and the blue line represents expected magnetic strength determined from the forward modeling.

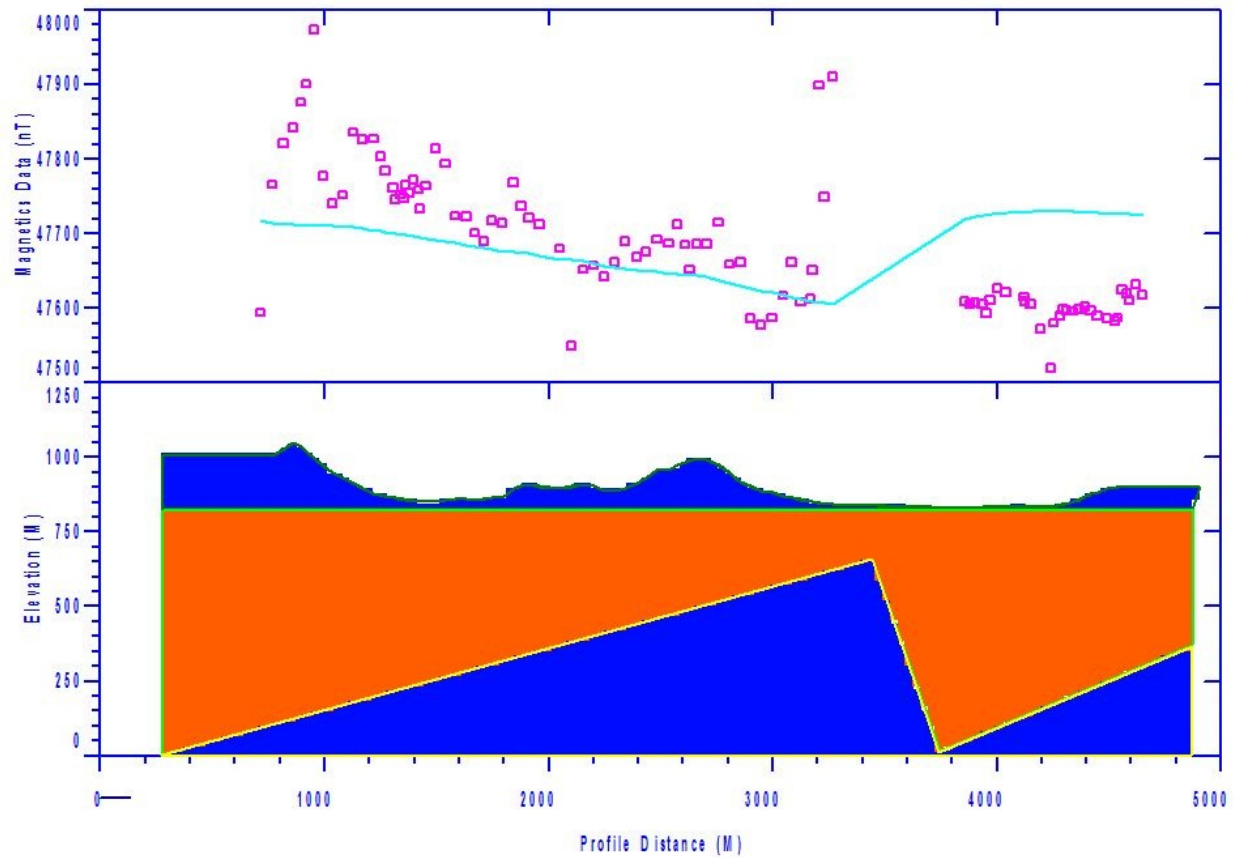


Figure 4.16. Geologic model similar to the previous model, but with the major fault modeled as approximately 200 meters larger. The additional size of the fault makes negligible impact on the expected surface magnetic strength, suggesting near-surface features will have by far the largest impact on magnetic susceptibility.

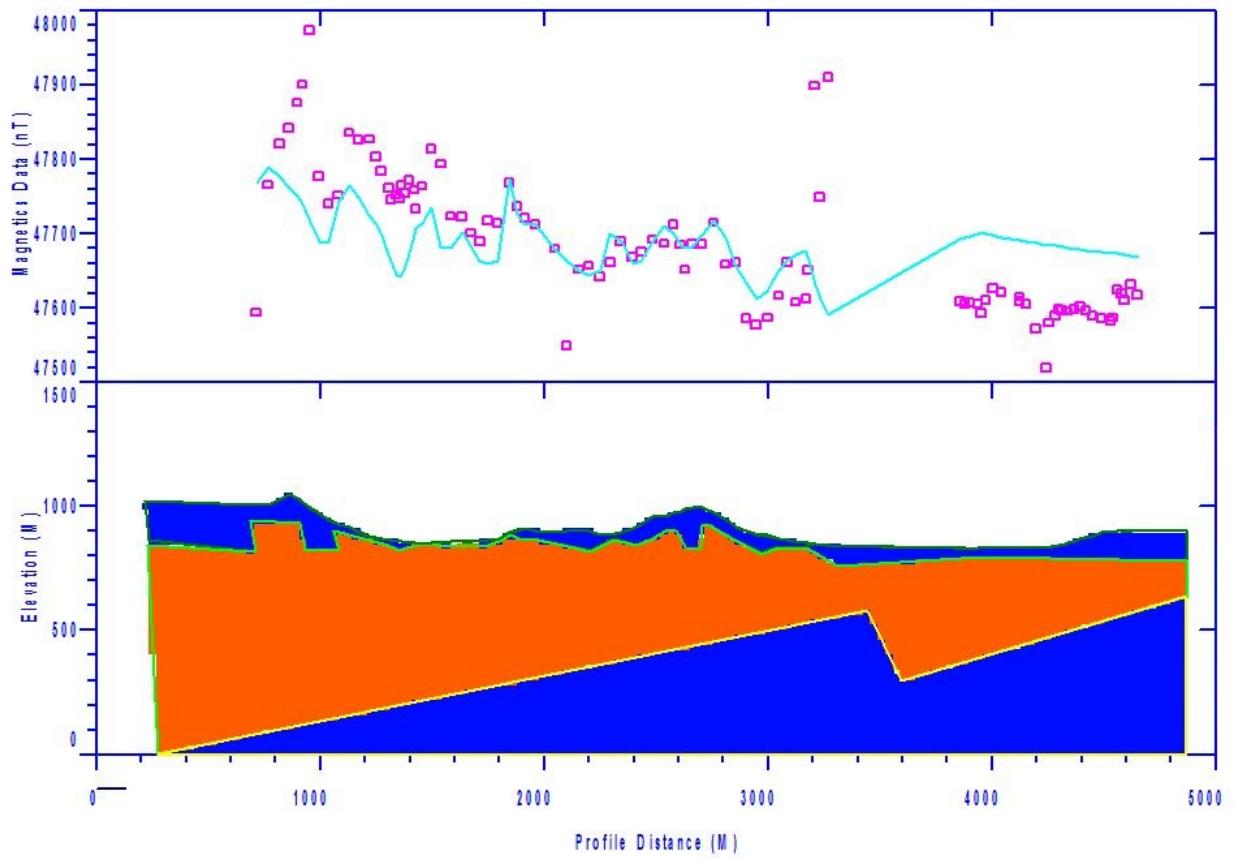


Figure 4.17. Geologic model with additional fault offsets added to the surface of the volcanics layer. This shows that relatively small variations in the volcanics layer are sufficient to explain most of the variation we observed in the field.

5. Gravity Survey

5.1 Introduction and Location

Gravity measurements were made on February 19th and March 5th of 2011. Measurements were made on the Star Pass and Yetmen trails in the Tucson Mountains. The objective of the gravity survey was to investigate faults that were interpreted on the geological cross sections by Lipman, 1993. The Lipman interpretation was based on surface observations of formation strike and dip. Surface observations provide valuable insights into the geology in this region. However, they cannot provide a quantitative subsurface model with accurate displacement of faults. The (Lipman,1993) cross sections were tested by forward modeling the geologic cross section and comparing the cross section with the data that we collected. Gravity was measured at 200m intervals, a total of 50 points were collected. Elevations were measured using three methods, Rhino 520HCx GPS system, altimeter, and contour maps.

A base station in the basement of the Harshbarger/Mines building was measured in the morning before each survey and in the evening after surveying in order to correct for any instrumental drift. See Table 5.1 for a summary of these measurements.

The regional gravity that has been previously measured across this area is shown in Figure 5.1. The contour map is a map of the complete Bouguer gravity anomaly across the field area. Complete Bouguer gravity includes terrain correction and curvature correction (Gettings 1996). The regional data provides a good overview of the gravity variations in this area, but the station spacing is too large for detailed modeling of the faults and other structures in the area.

Bouguer Anomaly Map

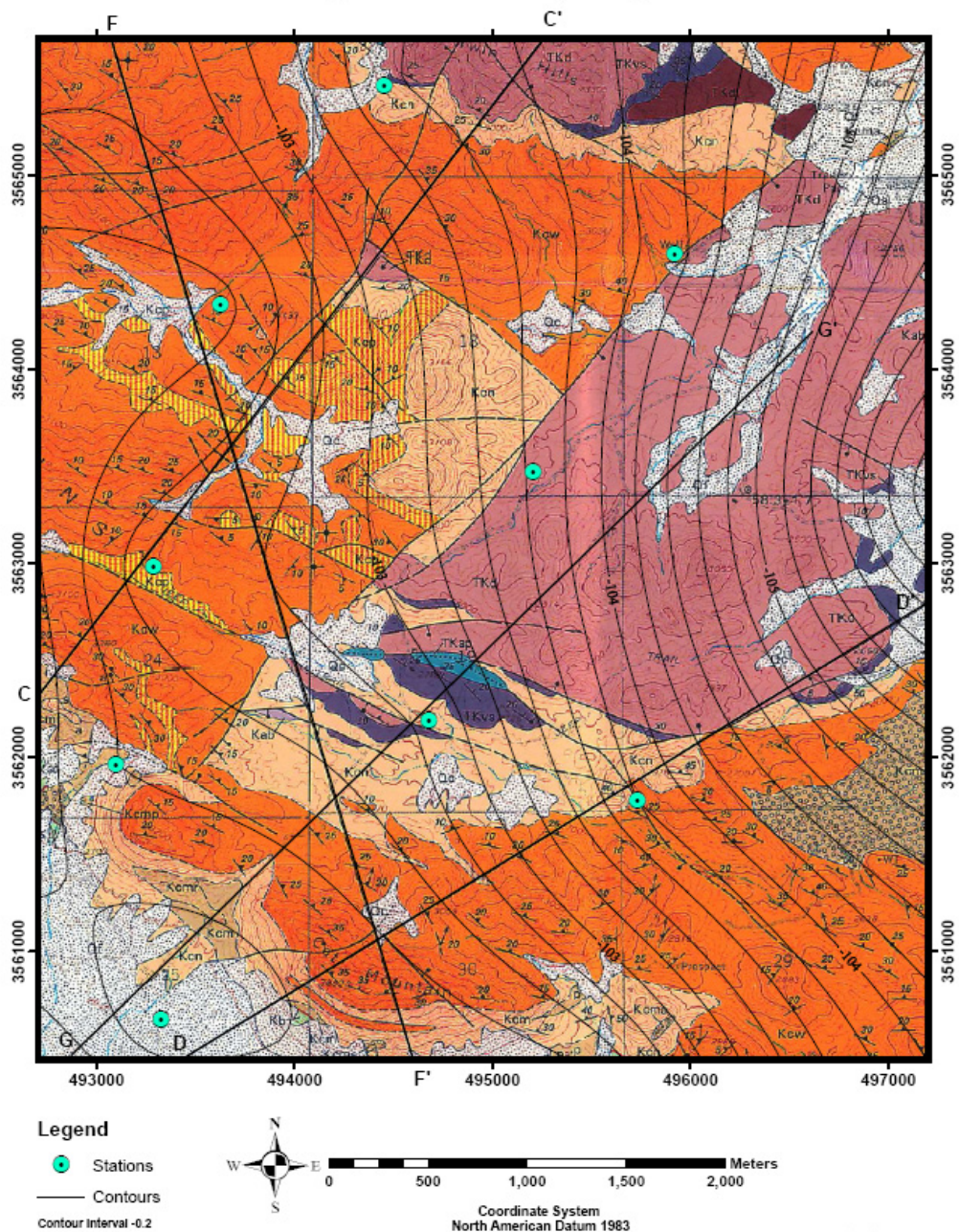


Figure 5.1. Regional gravity over the surveyed area. Black lines are gravity contours and light blue dots are gravity stations where readings were taken. Gravity in mGal that is plotted is the complete Bouguer gravity anomaly as it includes the terrain and curvature corrections as well as the Bouguer correction. Contours are overlaid on the geological map from Lipman, 1993; gravity data from Gettings, 1996.

5.2 Instrumentation and field procedures

Gravity points were measured using a Lacoste and Romberg gravimeter (G-575). A reading was taken by each of the two operators at a known gravity datum and at a base station in the field. The difference between the two operators from readings at the gravity datum was 0.01 mGals. Therefore along the trails, readings were taken by alternating operators after each point. The point spacing was 200m along a straight line. This distance was measured using the GPS.

A reading was made at the beginning of each survey day at the base station in the basement of Harshbarger/Mines on the UA campus (northwest corner of the building, just across from room 22). A repeat measurement was made at the end of the day. Instrumental drift for the readings is shown in Table 5.1. The drift was deemed to be negligible compared with the magnitude of the anomalies of interest in this survey. Note earth tides and the curvature of the earth were also not corrected for as they were considered negligible as well.

Field day #	Reading at datum start of day (mGal)	Reading at datum end of day (mGal)	Reading at base start of day (mGal)	Reading at base end of day (mGal)	Absolute Gravity reading at datum
1	2900.546	2900.372	2893.503	2893.400	979240.15
2	2900.885	2900.731	2893.698	2893.790	

Table 5.1. Gravity measurements at the base station used to check that instrumental drift is negligible and at a known gravity datum so the data can be compared to regional gravity. Absolute gravity measurement from Sternberg, 1986.

Gravity Stations

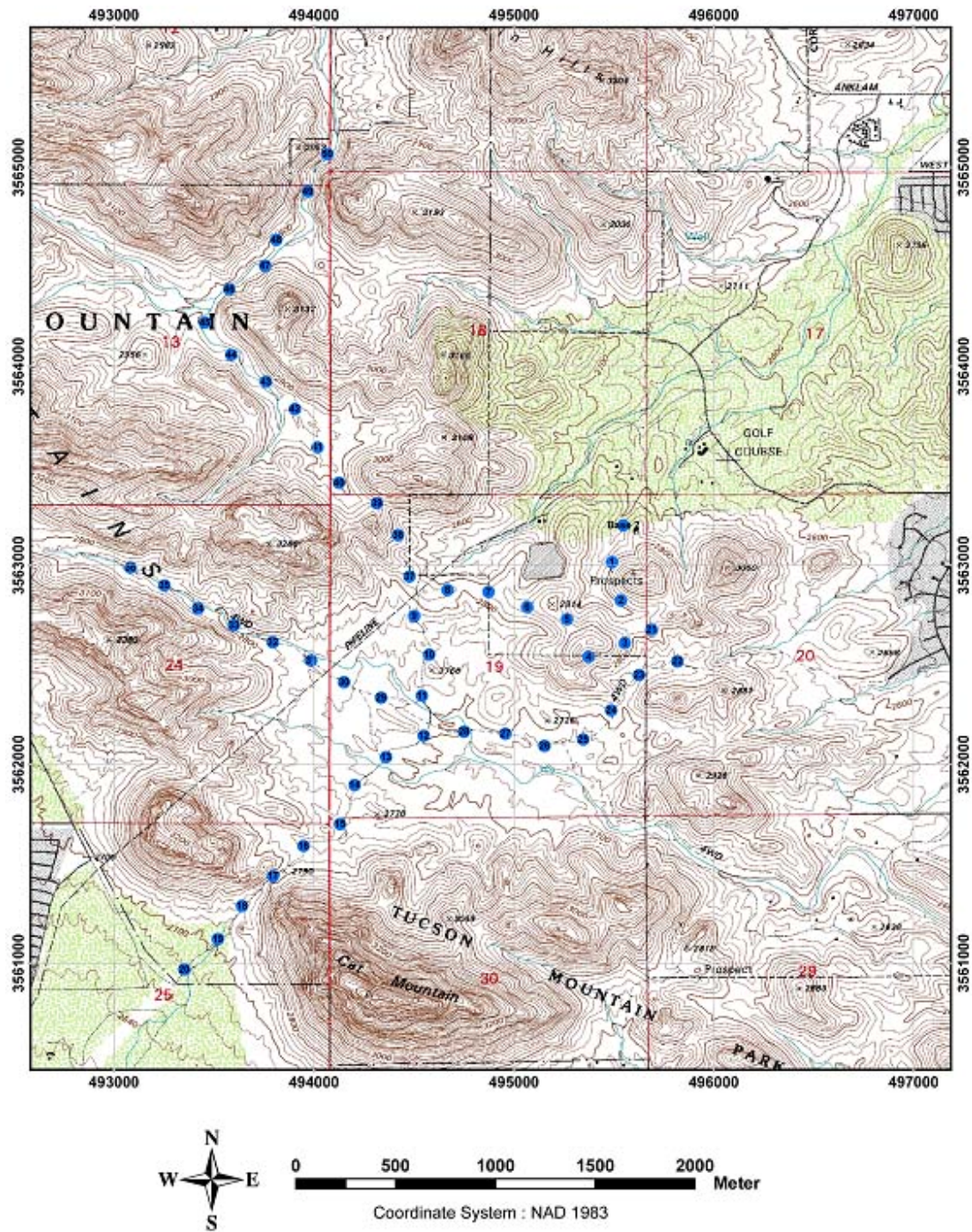


Figure 5.2. General overview of the Tucson mountains with gravity stations and field base station.

5.3 Data processing and interpretation

Gravity readings from the instrument were converted into mGals using tables that were included with the Lacoste and Romberg instrument. Corrections were applied to raw gravity measurements to account for changes in elevation (Free-Air correction). The contour elevation values were used as these were the most reliable. The Bouguer Correction was applied using a density value of 2.67 gm/cc. Data processing was done with an Excel spreadsheet (Table 5.3.).

5.4 Gravity Meter Test

In order to verify the calibration and accuracy of the gravity meter, a gravity reading was taken inside room 241A in the Mines building on the UA campus and on the ground outside and below this office. The distance to the ground was measured using a tape measure (5.83 meters). Using that known elevation, the difference in gravity was corrected to a baseline. For this test and all others, the datum was defined as sea level.

Gravity reading	Gravity difference with no correction	Gravity difference with free air correction
Gravity reading in office	2826.35	2900.889
Gravity reading outside office	2827.95	2900.733
Gravity difference	1.6	0.156

Table 5.2. Results from test using free air correction.

The difference between the two data points is 0.156 mGal (Table 5.2). Ideally, we would expect a small difference as the building is mostly empty space and should have a small effect on a gravity reading after the free air correction. The difference of 0.156 mGal is reasonable, given the free-space approximation for the building.

STATION	Easting (m)	Northing (m)	Time	OBSERVED GRAVITY (mGal)	ELEVATION (m)	v	f	Δg (mGal)	FREE AIR (mGal)	BOUGUER (mGal)	FINALGRAVITY (mGal)
Harshbarger Basement 1				2828.67	740	2871.11	1.02673	2900.546	0.000	0.000	2900.546
Harshbarger Basement 2				2828.5	740	2871.11	1.02673	2900.372	0.000	0.000	2900.372
Dr. Sternberg office				2826.35	751	2871.11	1.02673	2898.164	3.395	1.227	2900.332
Outside office				2827.95	741	2871.11	1.02673	2899.807	0.309	0.112	2900.004
Base 1	495548	3563202	09:35	2821.81	829.056335	2871.11	1.02673	2893.503	27.482	9.934	2911.051
Base 2	495548	3563202	15:28	2821.71	829.056335	2871.11	1.02673	2893.400	27.482	9.934	2910.949
Harshbarger Basement 1			7:00	2829	740	2871.11	1.02673	2900.885	0.000	0.000	2900.885
Harshbarger Basement 2			16:00	2828.85	740	2871.11	1.02673	2900.731	0.000	0.000	2900.731
Base 1	495548	3563202	8:15	2822.26	829.056335	2871.11	1.02673	2893.965	27.482	9.934	2911.513
Base 2	495548	3563202	15:32	2822.09	829.056335	2871.11	1.02673	2893.790	27.482	9.934	2911.339
1	495491	3563017	10:07	2817.65	847.647461	2871.11	1.02673	2889.232	33.220	12.008	2910.443
2	495536	3562825	10:28	2816.37	859.516541	2871.11	1.02673	2887.918	36.882	13.332	2911.468
3	495556	3562612	11:04	2814.71	868.88623	2871.11	1.02673	2886.213	39.774	14.377	2911.610
4	495374	3562541	11:24	2813.01	879.138123	2871.11	1.02673	2884.468	42.937	15.521	2911.885
5	495265	3562731	11:44	2812.88	878.078186	2871.11	1.02673	2884.334	42.610	15.402	2911.542
6	495067	3562792	11:54	2815.1	869.311279	2871.11	1.02673	2886.614	39.905	14.424	2912.094
7	494873	3562868	12:06	2817.46	860.409668	2871.11	1.02673	2889.037	37.158	13.432	2912.763
8	494668	3562877	12:21	2817.46	860.222656	2871.11	1.02673	2889.037	37.100	13.411	2912.726
9	494501	3562747	12:34	2819.49	849.274902	2871.11	1.02673	2891.121	33.722	12.189	2912.653
10	494576	3562552	12:47	2822.23	836.324158	2871.11	1.02673	2893.934	29.725	10.745	2912.915
11	494540	3562346	13:00	2823.38	827.25769	2871.11	1.02673	2895.115	26.927	9.733	2912.309
12	494549	3562145	13:13	2824.06	825.007446	2871.11	1.02673	2895.813	26.233	9.482	2912.564
13	494360	3562038	13:30	2822.8	826.293091	2871.11	1.02673	2894.519	26.630	9.626	2911.523
14	494203	3561898	13:45	2821.85	833.140747	2871.11	1.02673	2893.544	28.743	10.390	2911.897
15	494130	3561701	13:53	2821.02	837.631653	2871.11	1.02673	2892.692	30.129	10.891	2911.930
16	493947	3561591	14:03	2819.43	841.96759	2871.11	1.02673	2891.059	31.467	11.374	2911.152
17	493795	3561440	14:14	2818.67	847.901001	2871.11	1.02673	2890.279	33.298	12.036	2911.541
18	493641	3561290	14:26	2821.13	835.493225	2871.11	1.02673	2892.805	29.469	10.652	2911.621
19	493520	3561122	14:34	2823.7	826.223877	2871.11	1.02673	2895.444	26.608	9.618	2912.434
20	493351	3560970	14:44	2825.05	817.604858	2871.11	1.02673	2896.830	23.949	8.657	2912.121
21	495688	3562679	8:45	2815.44	863.811218	2871.11	1.02673	2886.963	38.208	13.811	2911.359
22	495818	3562518	8:57	2820.58	839.266785	2871.11	1.02673	2892.240	30.633	11.073	2911.800
23	495625	3562449	9:13	2822.3	832.747498	2871.11	1.02673	2894.006	28.621	10.346	2912.282
24	495487	3562273	9:22	2822.83	829.041809	2871.11	1.02673	2894.550	27.478	9.932	2912.096
25	495347	3562126	9:32	2825.08	817.433411	2871.11	1.02673	2896.860	23.896	8.638	2912.118
26	495152	3562094	9:43	2825.52	817.320129	2871.11	1.02673	2897.312	23.861	8.625	2912.548
27	494957	3562155	9:53	2824.74	822.060852	2871.11	1.02673	2896.511	25.324	9.154	2912.681
28	494750	3562165	10:02	2824.63	820.838745	2871.11	1.02673	2896.398	24.946	9.017	2912.327
29	494336	3562336	10:26	2822.97	833.457153	2871.11	1.02673	2894.694	28.840	10.425	2913.109
30	494150	3562414	10:35	2822.07	837.012756	2871.11	1.02673	2893.770	29.938	10.822	2912.886
31	493985	3562523	10:44	2821.72	841.480774	2871.11	1.02673	2893.411	31.317	11.320	2913.407
32	493794	3562615	10:53	2820.6	847.946716	2871.11	1.02673	2892.261	33.312	12.041	2913.531
33	493600	3562700	11:00	2819.81	853.136963	2871.11	1.02673	2891.450	34.914	12.620	2913.743
34	493420	3562785	11:10	2818.82	858.133911	2871.11	1.02673	2890.433	36.456	13.178	2913.711
35	493251	3562901	11:20	2817.98	862.396851	2871.11	1.02673	2889.571	37.771	13.653	2913.689
36	493083	3562990	11:29	2816.92	867.632385	2871.11	1.02673	2888.482	39.387	14.237	2913.632
37	494478	3562945	12:20	2816.47	867.150452	2871.11	1.02673	2888.020	39.238	14.183	2913.075
38	494420	3563153	12:32	2813.58	882.380554	2871.11	1.02673	2885.053	43.938	15.882	2913.109
39	494314	3563314	12:43	2810	901.276917	2871.11	1.02673	2881.377	49.769	17.990	2913.156
40	494125	3563417	12:57	2813.85	883.222473	2871.11	1.02673	2885.330	44.198	15.976	2913.552
41	494018	3563595	13:06	2815.58	876.928345	2871.11	1.02673	2887.106	42.256	15.274	2914.088
42	493905	3563787	13:16	2817.51	871.275635	2871.11	1.02673	2889.088	40.511	14.644	2914.956
43	493760	3563924	13:26	2818.35	864.822144	2871.11	1.02673	2889.950	38.520	13.924	2914.546
44	493587	3564060	13:33	2818.78	861.987061	2871.11	1.02673	2890.392	37.645	13.607	2914.429
45	493455	3564221	13:40	2820.47	854.211426	2871.11	1.02673	2892.127	35.245	12.740	2914.632
46	493577	3564389	13:52	2820.91	849.533447	2871.11	1.02673	2892.579	33.802	12.218	2914.162
47	493755	3564507	14:05	2821.57	846.917542	2871.11	1.02673	2893.257	32.994	11.926	2914.324
48	493811	3564638	14:14	2823.06	850.61499	2871.11	1.02673	2894.786	34.135	12.339	2916.583
49	493969	3564881	14:25	2823.36	834.228882	2871.11	1.02673	2895.094	29.079	10.511	2913.662
50	494067	3565069	2:34	2824.84	829.715576	2871.11	1.02673	2896.614	27.686	10.008	2914.292

Table 5.3. See caption on next page.

Table 5.3. All gravity readings along with processing. Location shows where reading was taken, reading is the raw Gravity meter reading, elevation was derived using all three methods for elevation measurement, V and F are constants from the Lacoste and Romberg table to convert the gravity readings to mGals (note there is also a C constant = 2800 for these data), Δg is the value of gravity in mGals converted using: $V+F*(\text{Grav Reading}-C)$, Free Air is the free air correction: $(0.3085*\text{elevation}-738)$, where 0.3085 is the accepted correction per foot except here it has been converted to mGals per meter and 738 is this is the elevation of the Datum point above sea level (Harbarger/Mines Basement). For every gravity survey, the data must be corrected back to a common datum point; here we have corrected back to sea level. Bouguer is the Bouguer Correction where: $((\text{elevation}-738)*0.1154)$, where 738 corrects back to sea level and 0.1154 is again the common value used per foot for Bouguer corrections, that has been converted to per meter. Final Gravity is Δg with both the Bouguer and Free air corrections applied to it. Note that we have not included terrain or curvature correction for these data.

To summarize these corrections, they are graphed in Figure 5.3. As each correction is applied, it lowers the variation, so we see that the calculations and elevation values are correct. If they were not, we would expect to see an increase in the variations.

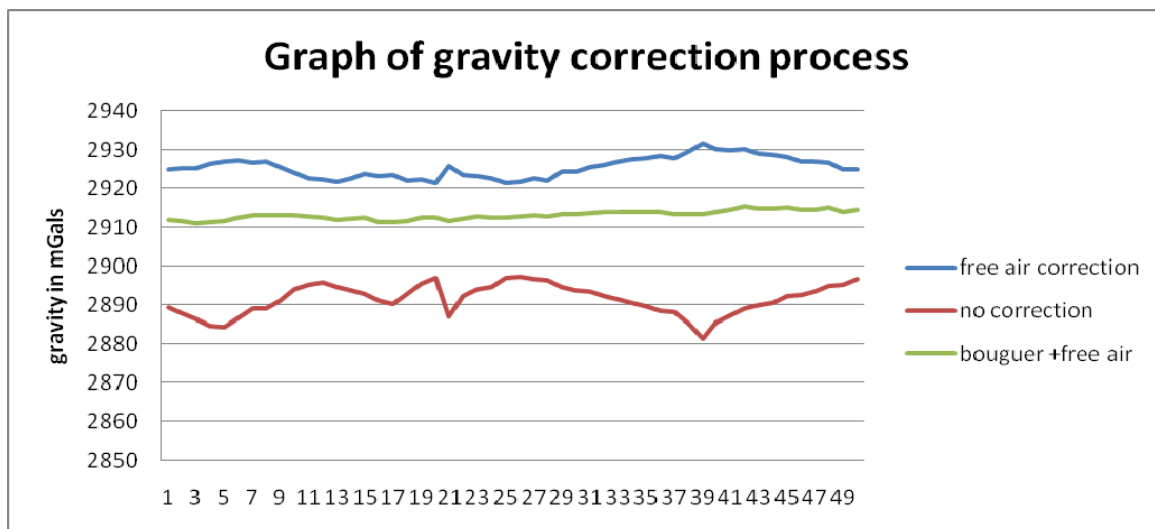


Figure 5.3. Effect of gravity corrections. Note that the corrections have smoothed out the variations in the data. Stations 1-50 have been graphed. The base stations and datum point have not been included as we are only interested in the variations along this profile line.

Once the data have been processed. The gravity data were projected onto the geological cross sections C-C', D-D', F-F' and G-G'. Location maps of these cross sections, and where points were projected to, can be seen for C-C' (Figure 5.4), D-D' (Figure 5.5), G-G' (Figure 5.6), F-F' (Figure 5.7). The projected points resulted in the following plots for each of the cross sections. C-C' (Figure 5.8), D-D' (Figure 5.9), F-F' (Figure 5.10), and G-G' (Figure 5.11). From these resulting plots, it was clear that only F-F' and G-G' had enough data projected onto them to be useful in our interpretation.

Gravity stations

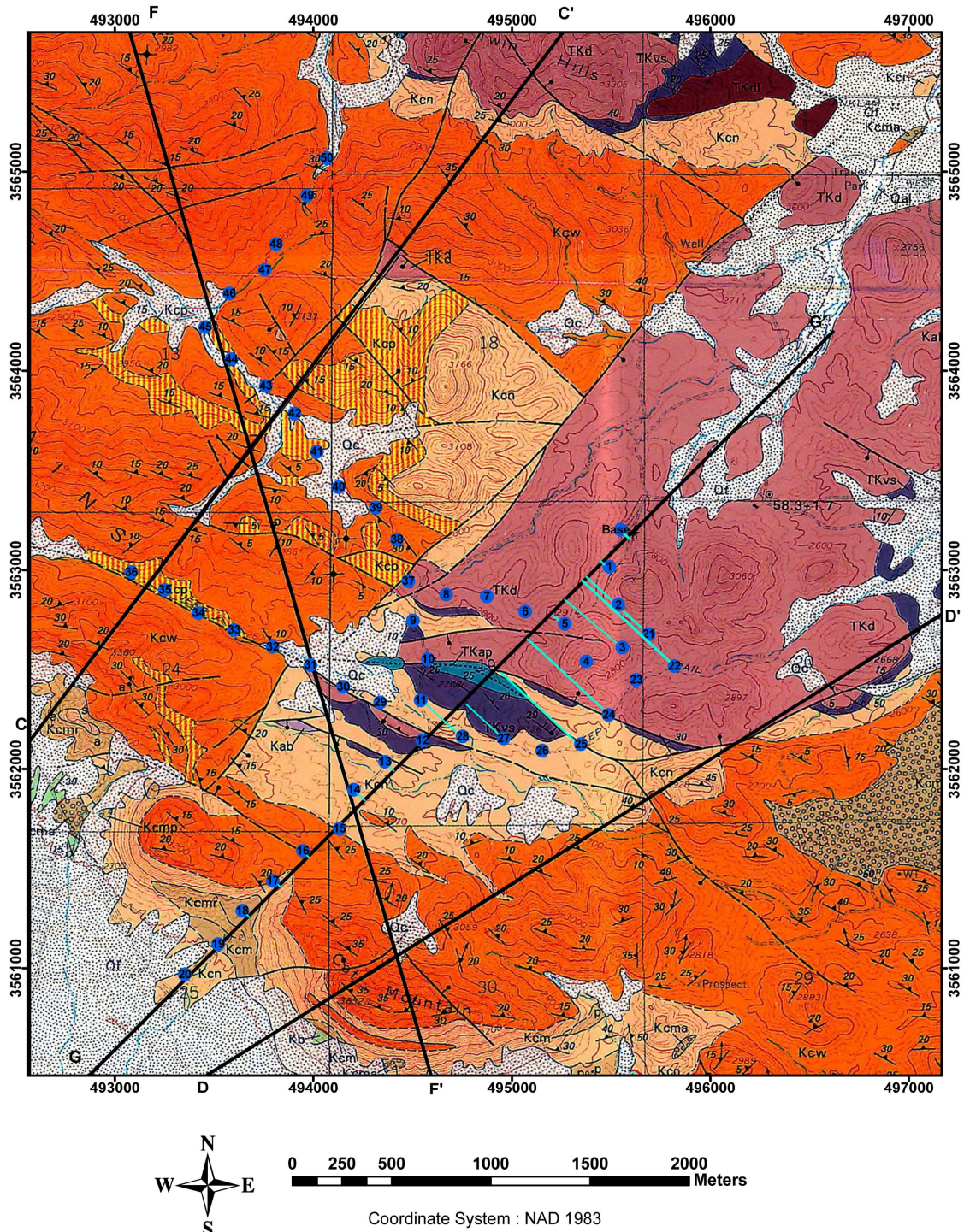


Figure 5.6. The survey area with all measured gravity stations (blue points). Location of geological cross sections (thick black lines) and points projected onto G-G' by the blue lines showing which point was projected and where it was projected. Modified from (Lipmann, 1993)

Gravity projection along C-C'

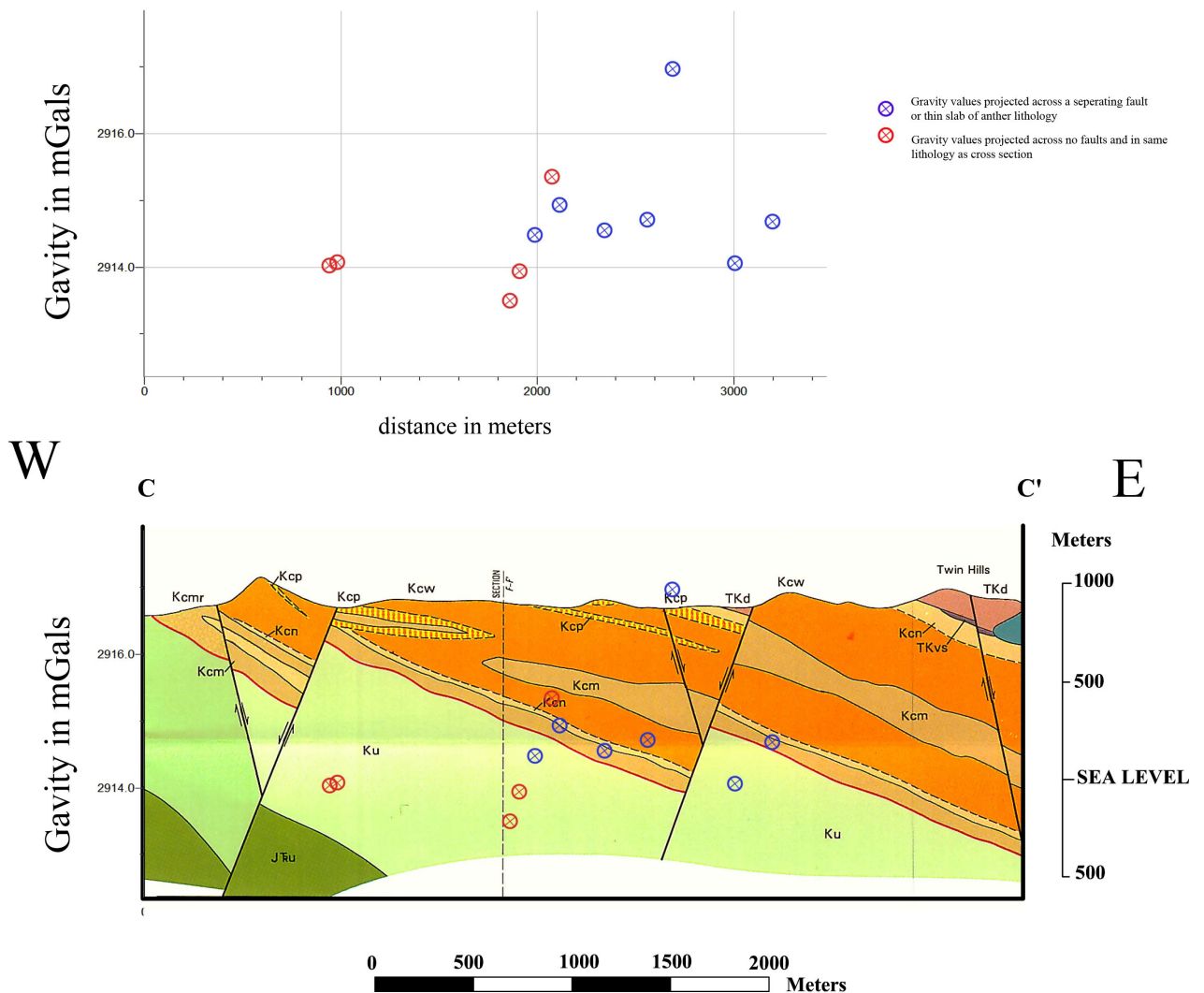


Figure 5.8. Gravity projection for C-C'. The graph on top shows gravity values in mGals on the y axis and distance in meters on the x-axis. The cross section below has had the points from the gravity survey superimposed so the correlations can be more easily seen. Modified from (Lipman,1993)

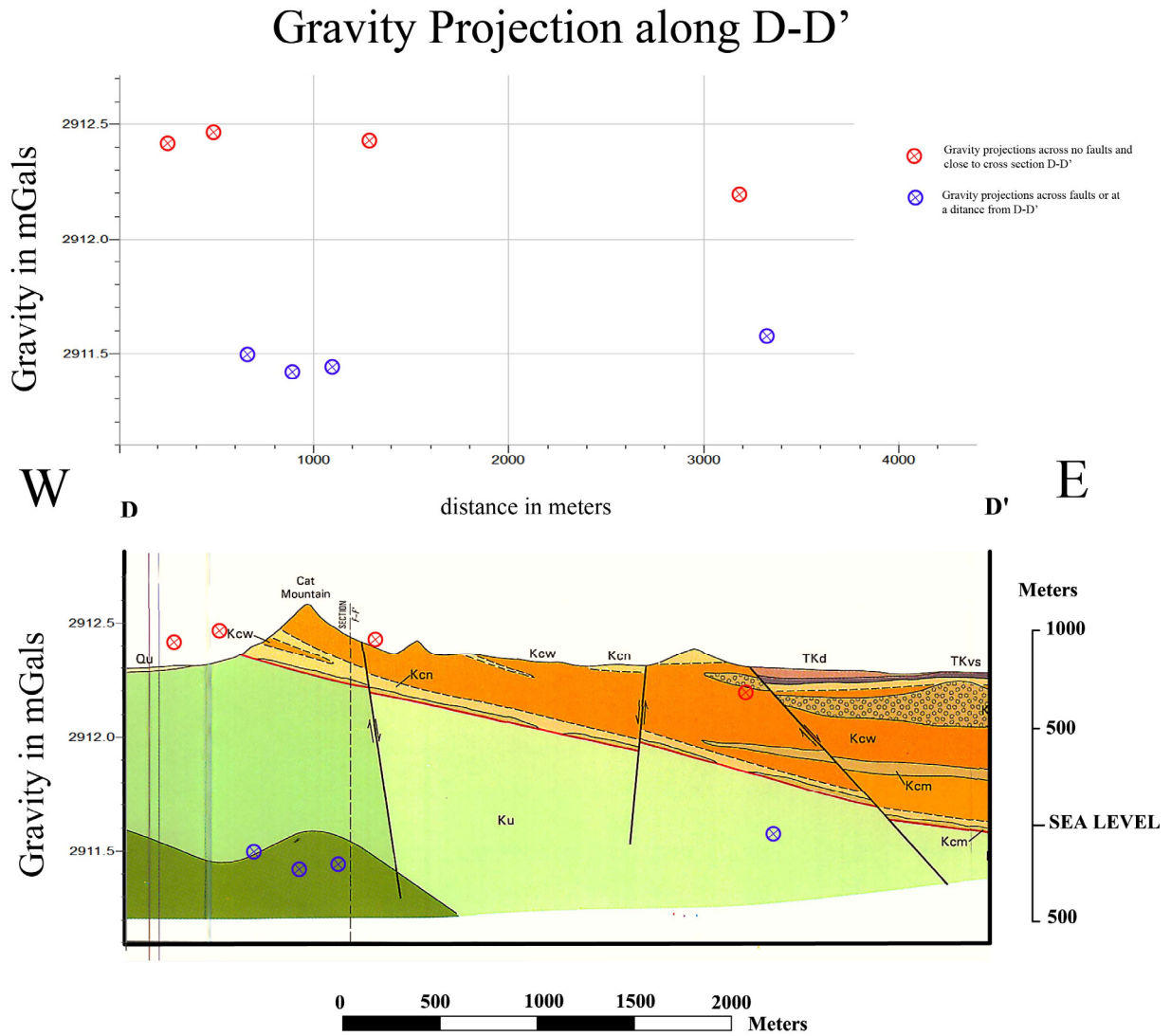


Figure 5.9. Gravity projection for D-D' The graph on top shows gravity values in mGals on the y axis and distance in meters on the x-axis. The cross section below has had the points from the gravity survey superimposed so the correlations can be more easily seen. Modified from (Lipman,1993)

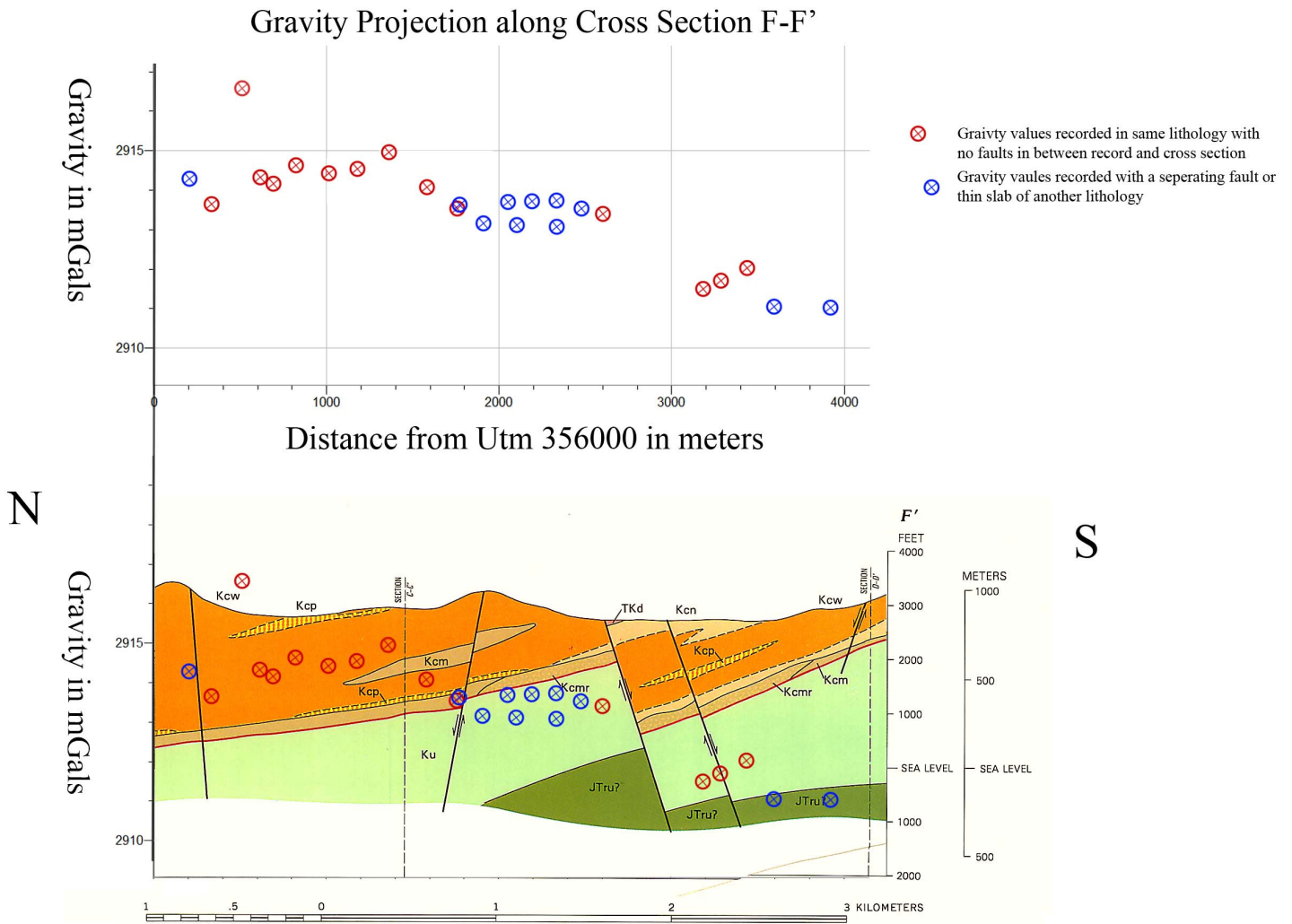


Figure 5.10. Gravity projection for F-F' The graph on top shows gravity values in mGals on the y axis and distance in meters on the x-axis. The cross section below has had the points from the gravity survey superimposed so the correlations can be more easily seen. Modified from (Lipman,1993)

Gravity projection along cross section G-G'

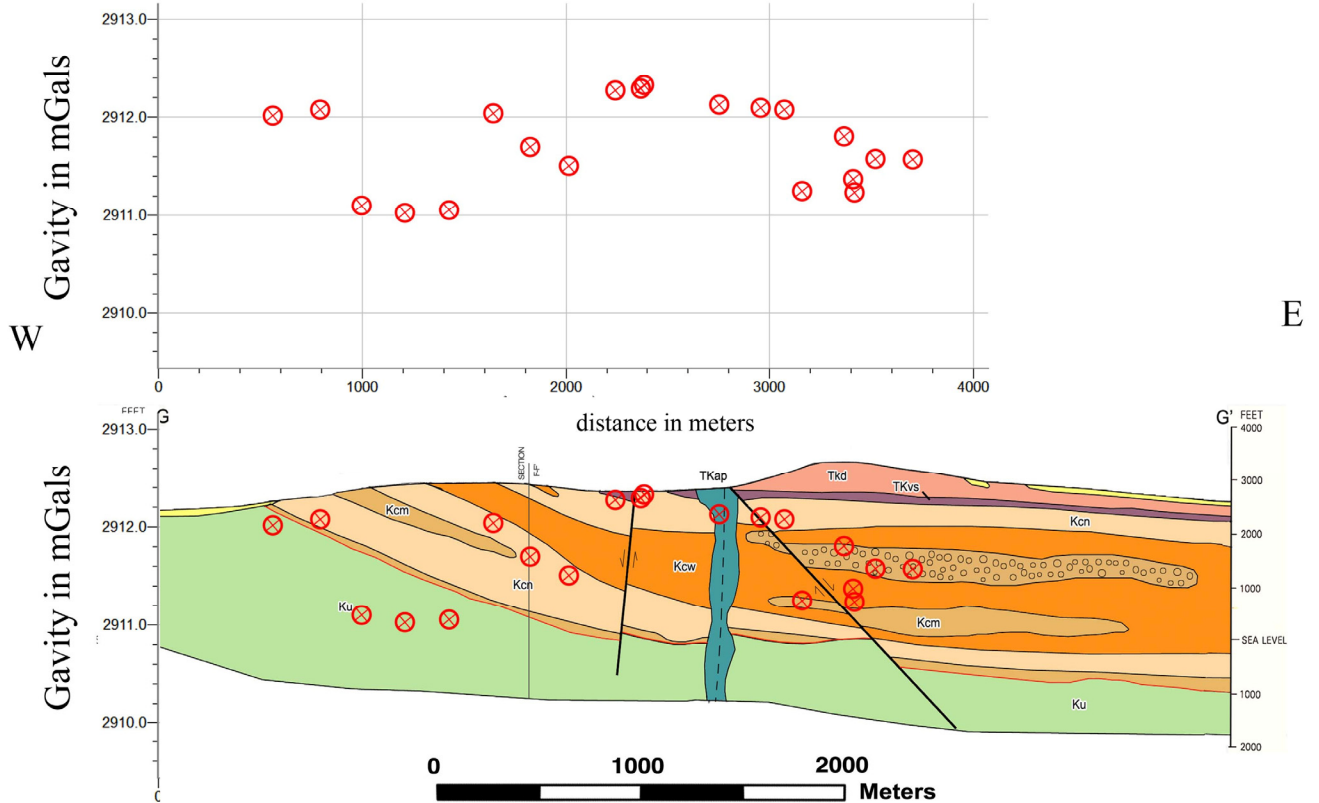


Figure 5.11. Gravity projection for G-G' The graph on top shows gravity values in mGals on the y axis and distance in meters on the x-axis. The cross section below has had the points from the gravity survey superimposed so the correlations can be more easily seen.

There were no clear anomalies evident from faults on G-G' in the gravity measurements. This may be due to the low amount of displacement on the faults. Cross section F-F' shows a possible effect from the main fault that has enough displacement in it to result in a gravity anomaly. We decided to only model F-F' for this reason. The fault is of interest, as it could be of importance for investigation into water resources or compressed air energy storage.

5.5 Gravity Modeling/Inversion

Modeling was carried out using IX2D from Interpex Limited. The first scenario was just a simple model of two different rock densities for the volcanics and the underlying porous rocks using the values for bed thickness and dip shown on the cross section Figure 5.12.

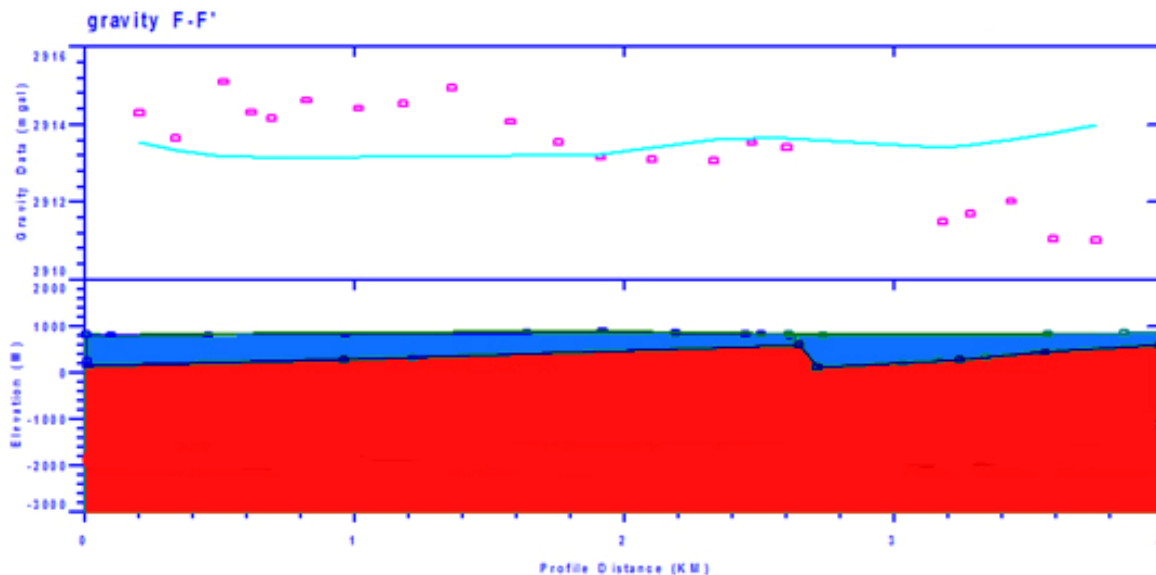


Figure 5.12. Simple gravity model with two layers of rock density - 2.4 g/cc for the volcanics (blue) and 2.55 g/cc for sedimentary rocks (red). Note topography varies across this section hence the changes in the projected gravity from 0-2 km. Densities were based on Houser, 2005.

The first model (Figure 5.12) shows that the outlined cross section model fault is not large enough to account for the difference in gravity that we see across that area. What should be noted is that it has created a decrease in gravity near 2.6 km – 3km, roughly where the anomaly in the data is, but the decrease is not large enough. There are some small variations in gravity from 0 - 3 km as a result of topography variations. The next iteration will require larger fault offset in the volcanic layer than proposed by (Lippman 1993), Figure 5.13.

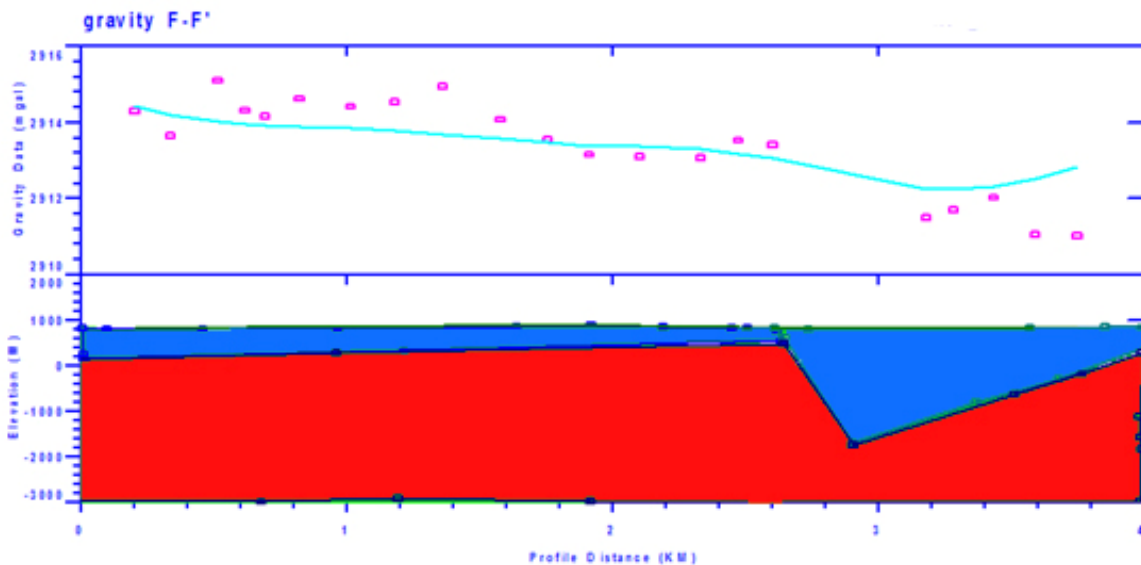


Figure 5.13. A greater displacement on the fault gives the expected shift in gravity. But does not match the rest of the data well. Volcanics - 2.4 g/cc (blue), sedimentary rocks – 2.55 g/cc (red). Note that topography varies across this section, hence the changes in the projected gravity from 0 - 2 km. Densities based on Houser, 2005.

Next, the fault offset has been increased from 500 m to approximately 2 km. This is still not a good match between data and model. We know that the fault location is correct, since the magnetic data show an anomaly across the fault. It appears that we cannot match the data with a simple two-layer model. The next step is to look at a more complicated model.

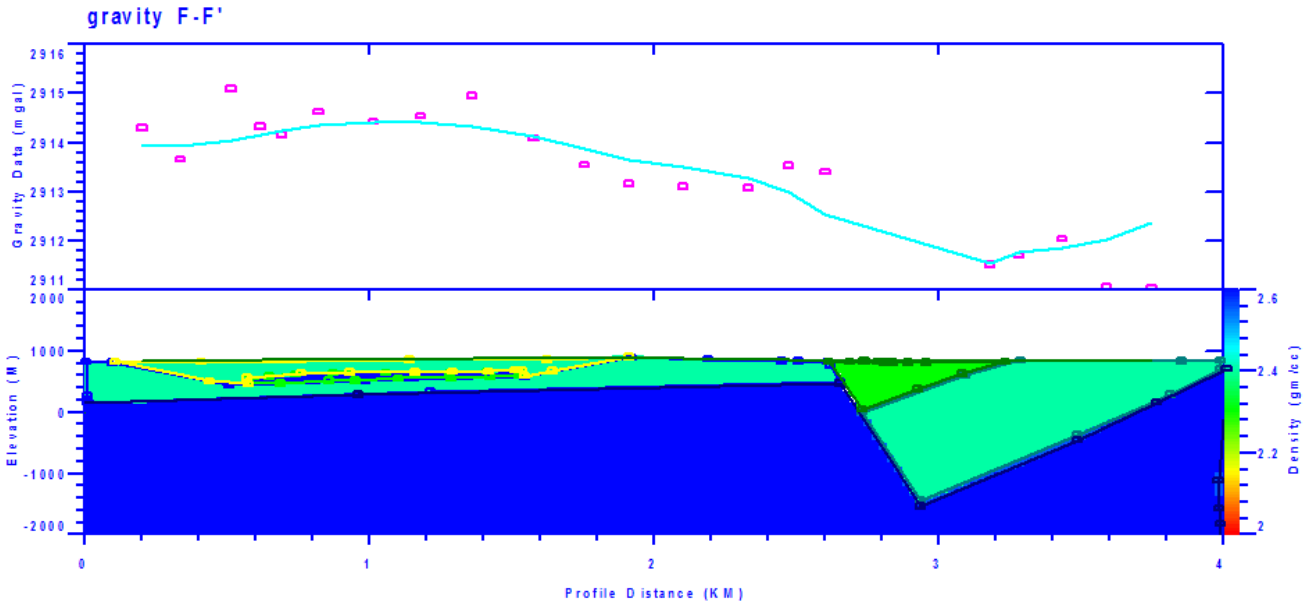


Figure 5.14. Four different layers in the model provides a better match to the observed anomaly over the fault. The following layers were used: Kcn partly welded rhyolite 2.3 g/cc (green), kcw densely welded rholite 2.4 g/cc (light blue), Ku Cretaceous sediments undivided 2.6 g/cc (blue) and a thin dense layer indicated by the lipman cross section Kcm dark blue in the middel of kcw at 2.6 g/cc the size of this layer has been modified to try and match the data.

In Figure 5.14, the model includes a total of 4 different layers. This results in a closer fit. Where the data do not match, this may be either a result of varying thicknesses in layers or due to projecting across small faults. This fault is very large compared to the results from CSAMT and TEM. So taking the lowest reasonable density for the overlying volcanic rocks we calculated the model in Figure 5.15.

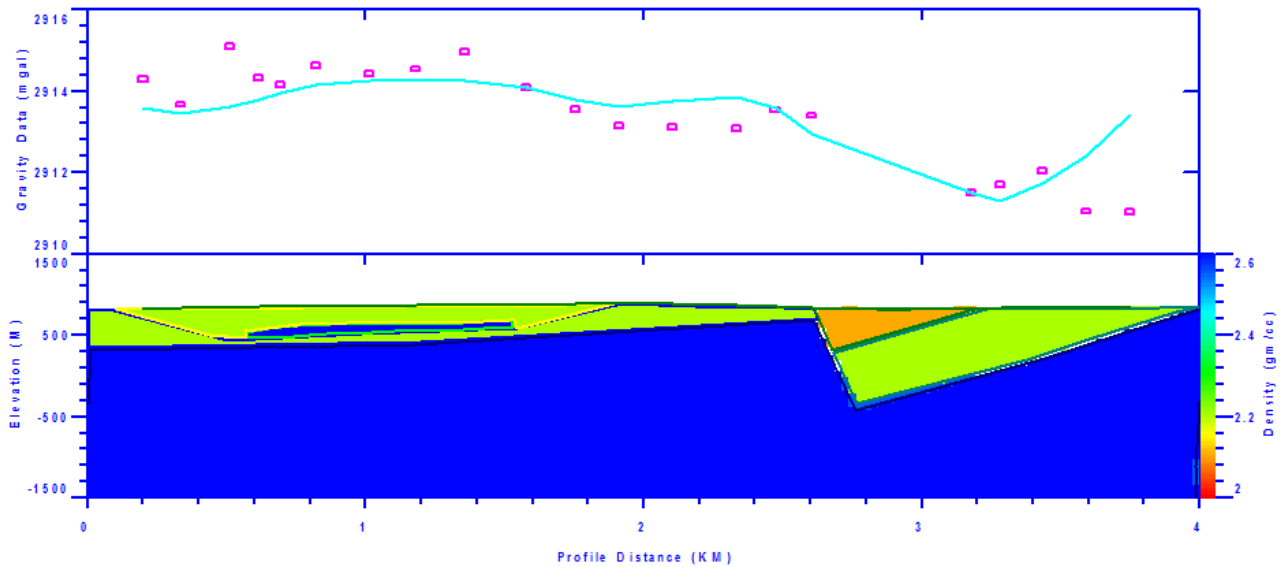


Figure 5.15. Again four different layers were used, but the density of the overlying volcanics has been lowered to try and reduce the fault size, fault offset has been brought down to 1 km. The following layers were used: Kcn partly welded rhyolite 2.3 g/cc (orange), kcw densely welded rhyolite 2.2 g/cc (green), Ku Cretaceous sediments undivided 2.6 g/cc (blue) and a thin dense layer indicated by the lipman cross section Kcm dark blue in the middle of kcw at 2.6 g/cc the size of this layer has been modified to try and match the data. Note that the volcanics layer on the left side had to be reduced in thickness compared to (Lipmann, 1993).

The gravity data and final models indicate that there is a large fault with a 1.0 - 1.6 km offset that penetrates down to the less dense sedimentary rocks. The 1 km offset is closer to the data from the TEM survey. This depth was achieved by reducing the density of the volcanics to the lower limit of the expected density range.

6. Summary and Conclusions

6.1. Data profile summaries.

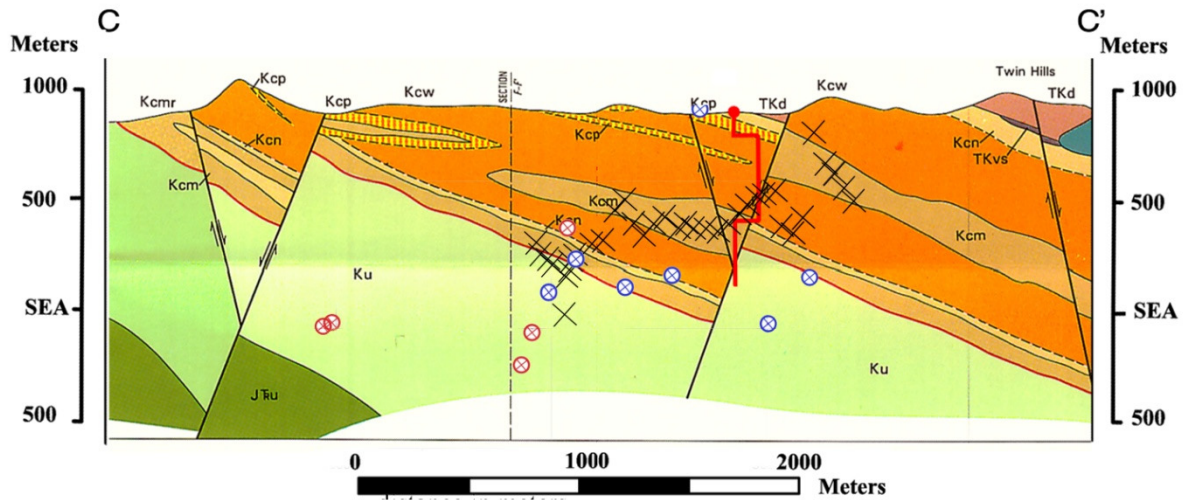


Figure 6.1. C-C' Summary. TEM (red line): The single TEM site distinguishes the volcanic rocks that are high resistivity from the deeper sedimentary rocks that are lower resistivity. Magnetics (black crosses): A magnetic field anomaly correlates with the central fault. Gravity (blue/red circles): The gravity readings vary widely across the profile, with no clear correlation with the fault. Geologic section modified from (Lipmann, 1993).

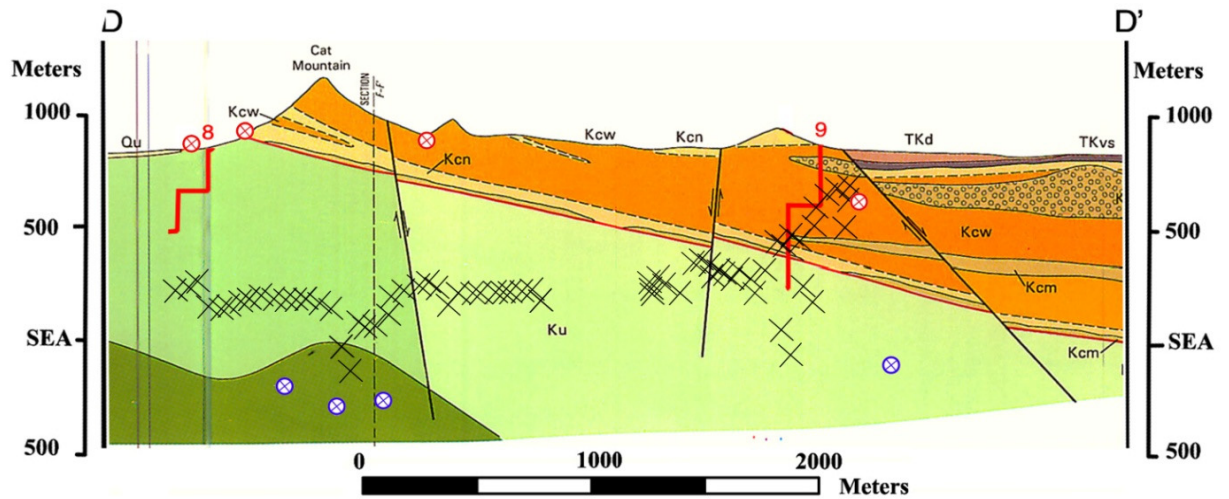


Figure 6.2. D-D' Summary. TEM (red lines): The two TEM sites show no clear correlation with the geologic cross section. Site 9 is likely affected by the Tucson Water Reservoir and should be ignored. Site 8 may be mapping depth to water table within the sedimentary rocks. Magnetics (black crosses): The magnetic field increases near the fault. However, the data set does not extend far enough East to provide a clear correlation with fault proposed by Lippman, 1993. Gravity (blue and red circles): The gravity readings are too sparse to make any conclusions concerning the gravity data on this profile. Geologic cross section modified From (Lipmann, 1993).

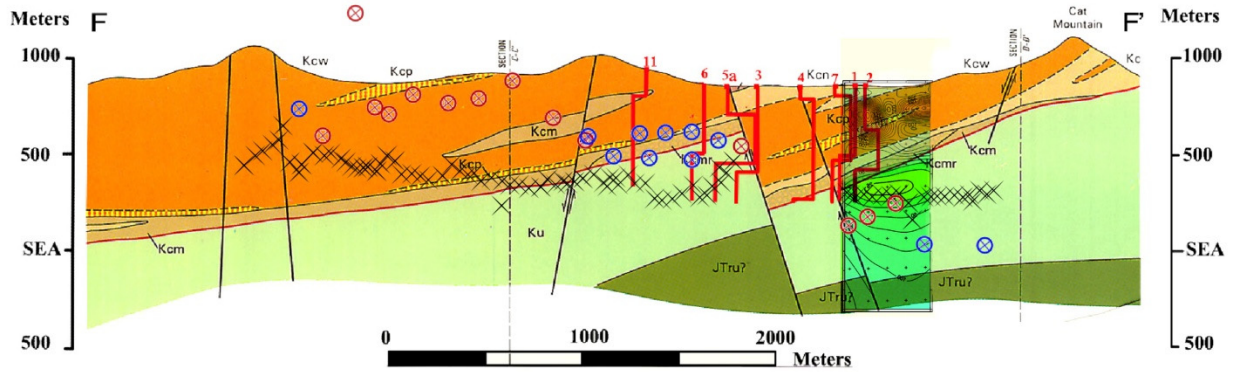


Figure 6.3. F-F' Summary. TEM (red lines): The TEM sites on this profile line distinguish between the high-resistivity volcanics (Kcw) that overlay the low-resistivity sedimentary rocks (Ku). Overall, the TEM data correlate well with the geological cross section. CSAMT (contour overlay): The CSAMT data correlate well with the interpreted geological cross section, including the depth to the sedimentary layers. Magnetics (black crosses): The magnetic data are too sparse across the main fault to derive any definitive conclusions. Gravity blue and red circles): Gravity measurements decrease suddenly across the main fault.

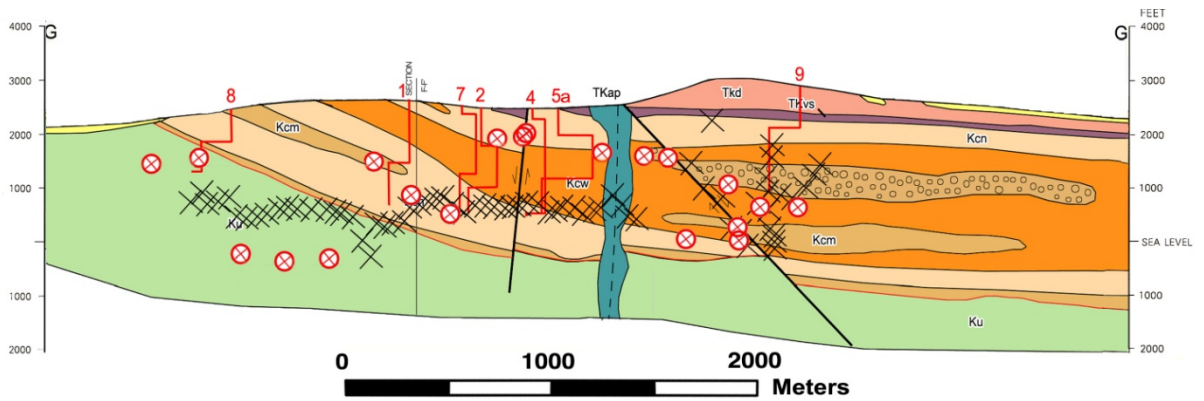


Figure 6.4. G-G' Summary. TEM (red lines): The welded volcanics (Kcw) have a high resistivity. The less welded volcanics (Kcm) have a lower resistivity. Site 9 should be ignored because of probable interference from the Tucson Water Reservoir. Magnetics (black crosses): Across the fault, the magnetic readings start to vary wildly, with no clear association with the fault. Gravity (red circles): The gravity values do not show a clear relationship to the fault.

6.2 Conclusions

The TEM and CSAMT survey results are generally in agreement with the geological interpretation of Lipman, 1993. The TEM and CSAMT surveys agree with the hypothesized geologic cross section in terms of the thickness of the welded (Kcw) and partly welded (Kcm) to non-welded (Kcn) volcanics, which overlay deeper sedimentary rocks (Ku). Interpreted faults and their proposed displacement were also detected with these methods and the results show a positive correlation with Lipman's interpretation. The TEM and CSAMT electrical resistivity data clearly show the presence of a deep conductive layer, below the resistive volcanic sequence, which is best illustrated on cross section F-F' (Figure 6.3).

The Magnetic data seem to have been largely affected by variations in magnetic susceptibility that occurs near the surface of the rhyolite within the Tucson Mountains. In some cases, there was some correlation of a magnetic field anomaly and a mapped fault; in other cases, there was no clear association.

Gravity measurements did correlate with the presence of a fault on one of the cross sections, but on other cross sections there was no visible correlation. Gravity modeling estimated a larger throw on the fault than the Lipman, 1993 interpretation and the TEM and CSAMT models. This larger depth may be due to the uncertainty in selection of the density values to use in the modeling.

Overall the geophysical surveys carried out in this study show a positive correlation with the geological interpretations made by Lipmann, 1993. When future surveys are undertaken to

further investigate the extent and depth of the porous conductive layer beneath the volcanics, we recommend that TEM and CSAMT surveys be emphasized. The gravity and magnetics surveys both showed a weaker correlation and there is more uncertainty in the modeling with these potential-field methods.

7. REFERENCES

Fiero, Brad, Geological Setting of Tucson, AZ, How the Tucson valley and surrounding mountains formed, <http://wc.pima.edu/Bfiero/tucsonecology/setting/geology.htm>

Gettings, M. E., 1996, Aeromagnetic, radiometric, and gravity data for Coronado National Forest, in Mineral resource potential and geology of Coronado National Forest, Southeastern Arizona and Southwestern New Mexico, edited by E. A. du Bray, U.S. Geological Survey Bulletin, 2083-D, 70–101.

Gettings, Mark, E., 2011, Personal Communication, Geology and Geophysics. USGS Western Mineral and Environmental Resources Science Center.

Houser, Brenda B., Lisa Peters, Richard P. Esser, and Mark E. Gettings, 2005, Stratigraphy and Tectonic History of the Tucson Basin, Pima County, Arizona, Based on the Exxon State (32)-1 Well By Brenda B. Houser, USGS SIR 2004-5076

Inman, J. R., 1975, Resistivity inversion with ridge regression, *Geophysics* v. 40 (no. 5) (1975), pp. 798–817.

Interpex, 2010, IX1D v3 Transient EM Software,
<http://www.interpex.com/ix1dv3/ix1dv3.htm>

Interpex, 2010, IX2D 2-D Gravity/Magnetics Software,
<http://www.interpex.com/IX2D/IX2D-GM.htm>

Lipman, Peter W., 1984, The roots of ash-flow calderas in North America: Windows into the tops of the granitic batholiths, *Journal of Geophysical Research*, v. 89, p. 8801-8841.

Lipman, P. W., and Sawyer, D. A, 1985, Mesozoic ash-flow caldera fragments in southeastern Arizona and their relationship to porphyry copper deposits, *Geology*, v. 13, no. 9, p. 652-656.

Lipman, Peter W., 1993, Geologic map of the Tucson Mountains Caldera, Southern Arizona, USGS Miscellaneous Investigations Series, Map I-2205.

Pima County Natural Resources, Parks and Recreation, www.pima.gov/nrpr

Sternberg, Ben K., Timothy C. Sutter, W. Dickson Cunningham, 1986, Report on Gravity Surveys for Desertron Sierrita Site.

Sternberg, B.K., Miletto, M.F., LaBrecque, D.J., Thomas, S.J., Poulton, M.M., 1991, revised Dec. 1992, The Avra Valley (Ajo Road) Geophysical Test Site: geophysical surveys, geologic data, and initial development of the test site, LASI-91-2, University of Arizona, Laboratory for Advanced Subsurface Imaging, Tucson, AZ.

Stokes, Philip J., Ben K. Sternberg, John Fleming, 2010, Geophysical exploration of the Tucson mountains, southern Arizona, for potential underground compressed air energy storage, 2010 GSA Denver Annual Meeting (31 October –3 November 2010).

Stokes, Philip J., Ben K. Sternberg, 2010, Appraisal of the Tucson Mountains for Solar Energy Storage: Preliminary Acquisition of Geophysical Data and Results, Laboratory for Advanced Subsurface Imaging (LASI) and Arizona Research Institute for Solar Energy (AzRISE).

USGS Publications Warehouse, <http://pubs.usgs.gov/of/2000/ofr-00-0155>